Multivariate modulation of Zr_6 UiO-66 for enhanced cooperative CO_2 adsorption through defect multi-functionalisation

Carmen Rosales-Martínez,[a] Sousa Javan Nikkhah,[b] Marcileia Zanatta,[c,d] Juan Carlos Martínez,[e] Matthias Vandichel,[b*] Isabel Abánades Lázaro[a*]

S.1. General Experimental Remarks 2
S.2. Materials and Synthesis 3
S.3. Characterisation of multivariate modulated MOFs 4
  S.3.1 Powder X-Ray Diffraction (PXRD) 4
  S.3.2 Proton Nuclear Magnetic Resonance (^{1}H NMR) 5
  S.3.3 Fourier transformed Infra-Red (FT-IR) 8
  S.3.4 Thermogravimetric analysis (TGA) 12
  S.3.5 Scanning Electron Microscopy (SEM) 13
  S.3.6 Z-potential 14
  S.3.7 Characterisation of MTVM MOFs stability in different solvents 18
    S.3.7.1 Solvent stability of UiO-66 18
    S.3.7.2 Solvent stability of UiO-66-NH_2 21
    S.3.7.3 Solvent stability of UiO-66-SO_3 25
    S.3.7.4 Solvent stability of UiO-66-NH_2/SO_3 29
  S.3.8 Solid-state UV-Vis 33
  S.3.9 Nitrogen Adsorption and Desorption Measurements 35
S.4. Time-resolved synchrotron small-angle X-ray scattering (SAXS) 38
S.5. Characterisation of samples synthesised at different reaction times 50
S.6. CO_2 Adsorption and Desorption Measurements 61
S.7. CO_2 Adsorption of MOFs containing different quantities of modulators 62
  S.7.1 CO_2 Adsorption of MOFs variable modulator UiO-66-NH_2 62
  S.7.2 CO_2 Adsorption of MOFs variable modulator UiO-66-SO_3 67
  S.7.3 CO_2 Adsorption of MOFs variable modulator UiO-66-NH_2/SO_3 72
S.8. CO_2 Adsorption Simulations 77
S.9. References 89

S.1. General Experimental Remarks

Powder X-Ray Diffraction (PXRD): PXRD profiles were collected in Kapton capillary at room temperature using a D8 discovery Bruker diffractometer from 2 to 40 2Ө degrees using copper radiation (Cu Kα), λ = 1.5418 Å, with a 0.015 step size (University of Valencia)

Thermogravimetric Analysis (TGA): were carried out with a Mettler Toledo TGA/SDTA 851 apparatus between 25 and 800 °C under ambient conditions (10 $°C·min^{-1}$scan rate and an air flow of 9 $mL·min^{-1}$). (University of Valencia)

Nuclear Magnetic Resonance Spectroscopy (NMR): NMR spectra were recorded on either a Bruker AVIII 300 MHz spectrometer and referenced to residual solvent peaks. (University of Valencia)

Gas Uptake: N_2 and CO_2 adsorption and desorption isotherms were performed in a Tristar II Plus Micromeritics sorptometer, at 77 K and 273 K/293K, respectively. Activation was set at 120ºC, under vacuum, for 24 hours on the already activated samples. (University of Valencia)

Scanning Electron Microscopy (SEM) and single point energy-dispersive X-Ray analysis (EDX): particle morphologies, dimensions and point energy-dispersive X-Ray analysis were studied with a Hitachi S-4800 scanning electron microscope at an accelerating voltage of 20 kV. (University of Valencia)

Energy-dispersive X-Ray analysis (EDX) mapping: the mapping of different elements was studied using a SCIOS 2 field emission scanning electron microscope with focused ion beam at an acceleratin-g voltage of 20 kV. (University of Valencia)

Fourier Transform Infrared Spectroscopy: IR spectra of solids were collected using a Shimadzu Fourier Transform Infrared Spectrometer, FTIR-8400S, fitted with a Diamond ATR unit. (Universityof Valencia)

Dynamic Light Scattering and Z-potential: Colloidal analysis and Z-potential were performed by Dynamic Light Scattering (DLS) with a Zetasizer Ultra potential analyser equipped with Non-Invasive Backscatter optics (NIBS) and a 50 mW laser at 633 nm. (University of Valencia).

Band gap measurements: UV-Vis diffuse reflectance spectroscopy (DRS) was performed on a Jasco V-670 spectrophotometer using an integrated Labsphere in the range 200-900 nm. (University of Valencia)

Small Angle X-Ray Scattering: SAXS patterns were measured at NCD-SWEET beamline (ALBA Synchrotron) using a Pilatus detector 1M 3s with a sample-detector distance of 2.172 meters and a wavelength of 1Å. Data treatment was performed with Igor 9, irena Package and DMF-containing capillary were used for background subtraction.

S.2. Materials and Synthesis

All reagents were obtained from commercial sources and were used without further purification.

Synthesis: In 8 mL vials, $ZrCl_4$ (0.45 mmol, 1 equivalent, 104.9mg), terephthalic acid (0.45 mmol, 1 equivalent, 74.8 mg), and the modulators (0.45 mmol, 1 equivalent) were dissolved in 5 mL of DMF with 0.35 mL of glacial acetic acid. The reaction mixtures were sonicated for 5 minutes and placed in an oven at 120ºC. After 24 hours, the reaction mixtures were cooled down to room temperature.

Table S1: Synthetic conditions.

Sample	zirconyl chloride (mmol)	BDC (mmol)	Benz-NH_2 (mmol)	Benz-SO_3 (mmol)
UiO-66	0.45	0.45	0.00	0.00
UiO-66-NH_2	0.45	0.45	0.45	0.00
UiO-66-SO_3	0.45	0.45	0.00	0.45
UiO-66-NH_2/SO_3	0.45	0.45	0.45	0.45

Scheme S1: Schematic representation of the synthetic route to obtain the different MOFs.

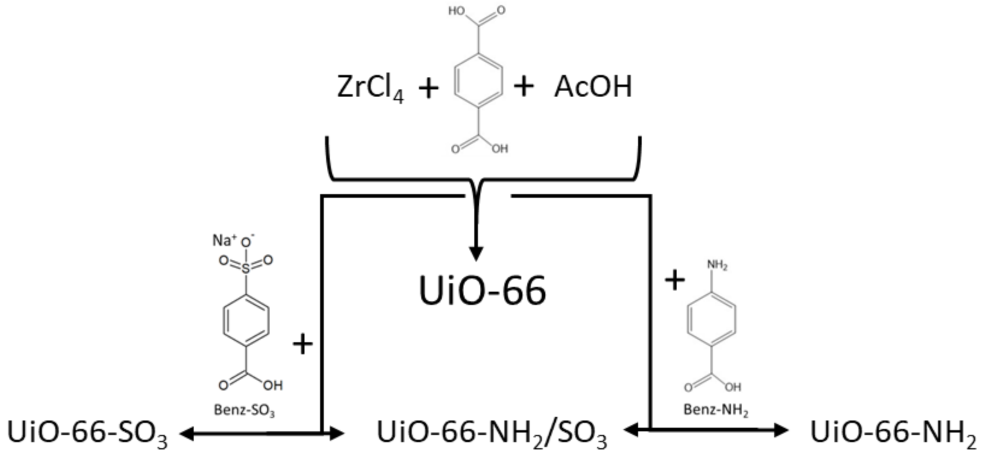

BDC stands for benzene dicarboxylic acid, also known as terephthalic acid; Benz-NH_2 stands for p-amino benzoic acid; Benz-SO_3 stands for p-sulfobenzoic acid sodium salt.

Activation protocols: The resultant powder was collected by centrifugation (5000 rpm, 5 min) and washed with DMF (X3) and MeOH (x3) through dispersion-centrifugation cycles. The samples were further activated by stirring the samples in MeOH at room temperature for approximately 24 hours, after what two further MeOH dispersion-centrifugation cycles were performed. The samples were further dried under vacuum at room temperature for 24 hours before characterisation.

MOF digestion: Acid-digested ^{1}HNMR was performed by digesting the MOFs (ca. 5mg) in 0.6 mL of deuterated dmso with 5 drops of deuterated sulfuric acid. The digestions were heated at 70ºC for 24 hours upon stirring, the time at which all the material was dissolved, resulting in complete digestion.

S.3. Characterisation of multivariate modulated MOFs

S.3.1 Powder X-Ray Diffraction (PXRD)

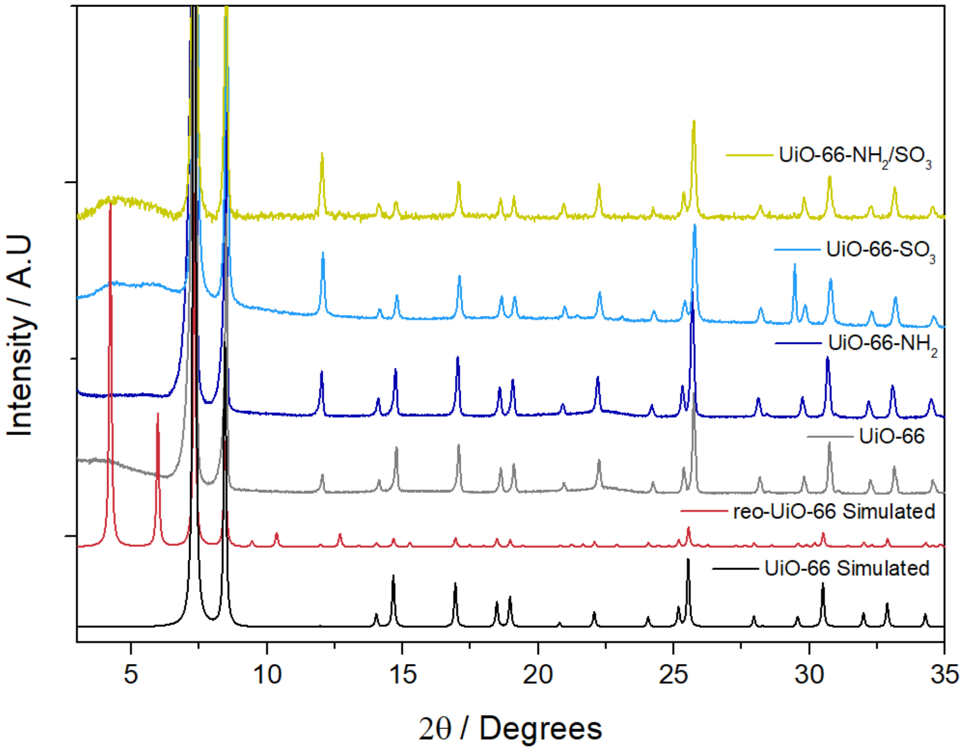

Figure S1: PXRD patterns compared to simulated UiO-66 and ***reo*** UiO-66, showing the appearance of ***reo*** phase features for UiO-66-SO_3 and UiO-66-NH_2/SO_3.

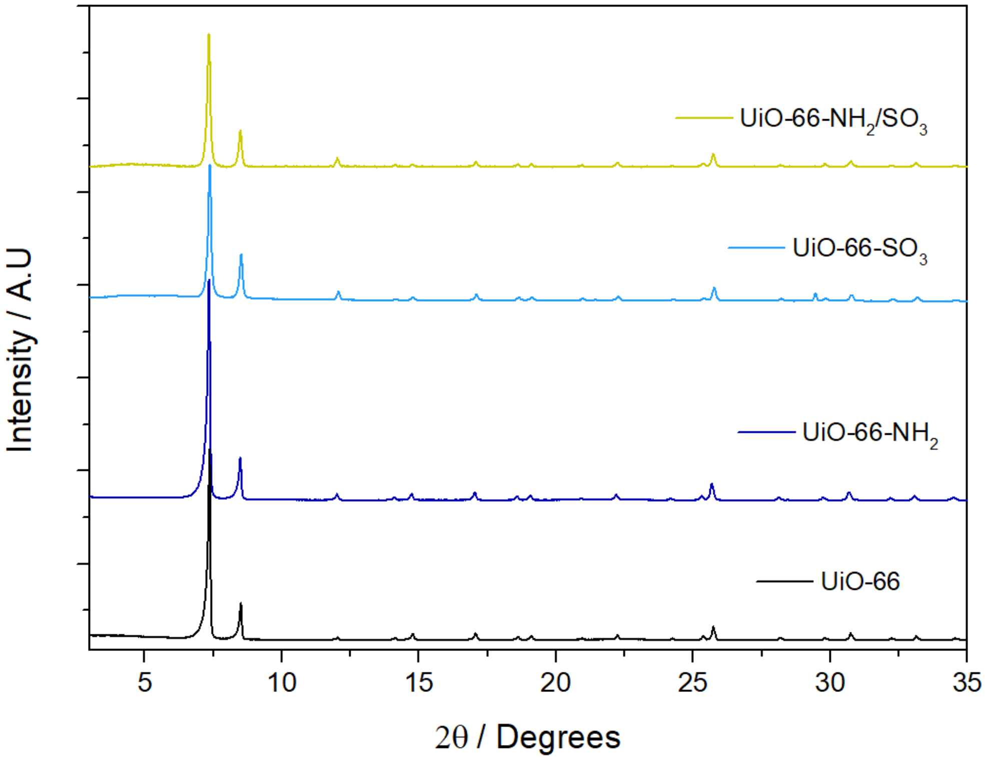

Figure S2: PXRD patterns of the MOFs.

S.3.2 Proton Nuclear Magnetic Resonance (^{1}H NMR)

Acid-digested ^{1}HNMR was performed by digesting the MOFs (ca. 5mg) in 0.6 mL of deuterated dmso with 5 drops of deuterated sulfuric acid. The digestions were heated at 70ºC for 24 hours upon stirring, the time at which all the material was dissolved, resulting in complete digestion.

Benz-X modulators were present in the ^{1}H NMR profiles alongside formic acid coming from the decomposition of DMF during synthesis, and acetic acid. Incorporation of modulators and defect-compensating species, is expressed as the **molar ratio** (R_{mod},) between modulator and bdc, $\mathrm{Rmod} = \frac{\mathrm{Mod}}{\mathrm{bdc}}$ and as the **molar percent** of modulator (mol%) compared to bdc, mol%= $\frac{\mathrm{Mod}}{\mathrm{Mod+bdc}} * 100$, while the **total modulator percent** (total mod%) is calculated taking into account all modulators and bdc, $\text{total mod\%} = \frac{\mathrm{Mod1+mod2}}{\mathrm{Mod1+mod2+bdc}} * 100$

The terephthalic acid linker appears as a singlet at *ca.* 8.1 ppm (4H). The singlet that corresponds to 1 H at *ca.* 7.9 ppm is attributed to DMF, while the singlet at *ca*. 8.2 ppm is attributed to formic acid (1H) coming from the decomposition of DMF during synthesis.[1] The modulator signals that have been used to perform the integrations that result in the estimation of the modulator content compared to the linker are represented in Figures S3-S5 (7.42 ppm for Benz-NH_2 and 7.63 for Benz-SO_3), and each of them integrates two protons. It is important to comment that due to the low integration of modulator signals in comparison to the linker, we consider the values provided as an estimation.

Please note that a minor shifting of these signals can be observed due to the use of deuterated sulfuric acid to digest the MOFs for ^{1}H NMR analysis. For Benz-NH_2 containing samples, the intensity of the Benz-NH_2 proton at ca. 7.42 ppm (2H) is subtracted from the intensity of the signal of the linker (ca. 8.1 ppm) for adequate modulators' determination.

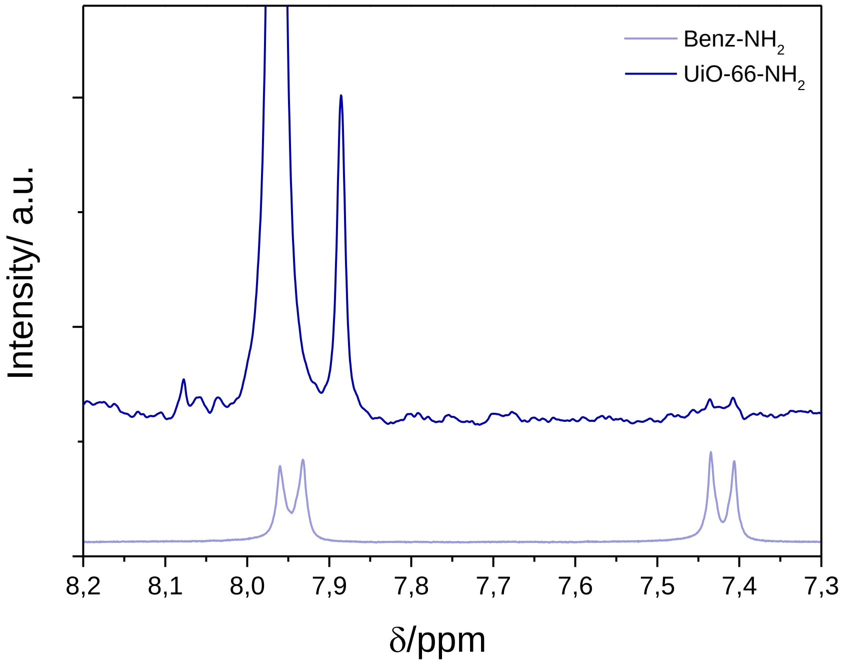

Figure S3: ^{1}H NMR profiles acid-digested UiO-66-NH_2, compared to the free modulator.

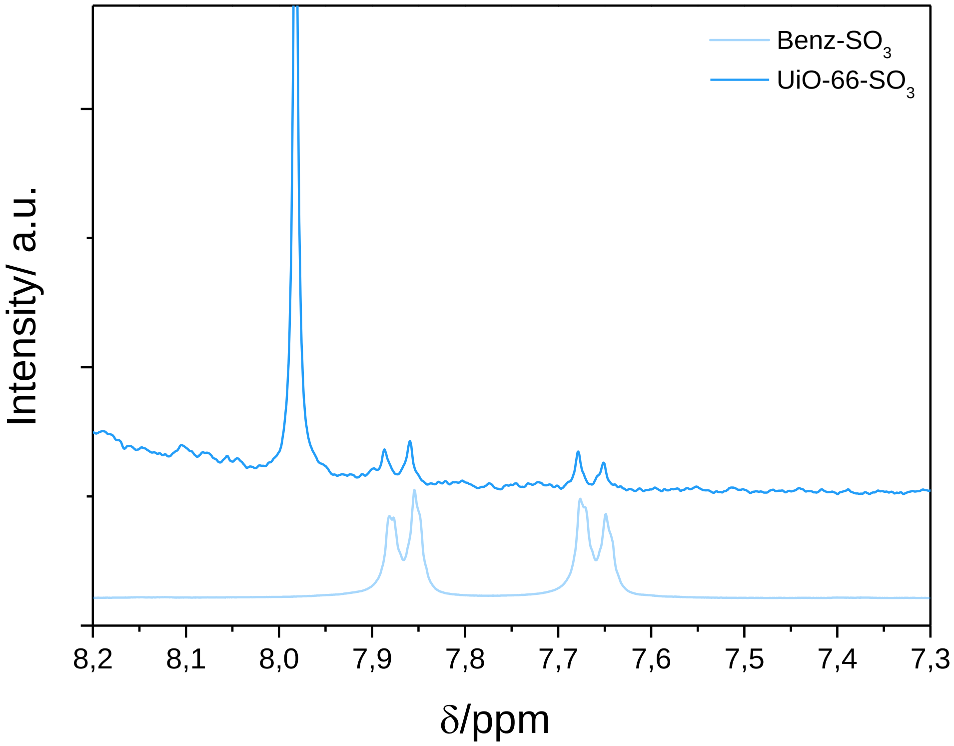

Figure S4: ^{1}H NMR profiles acid-digested UiO-66-SO_3, compared to the free modulator.

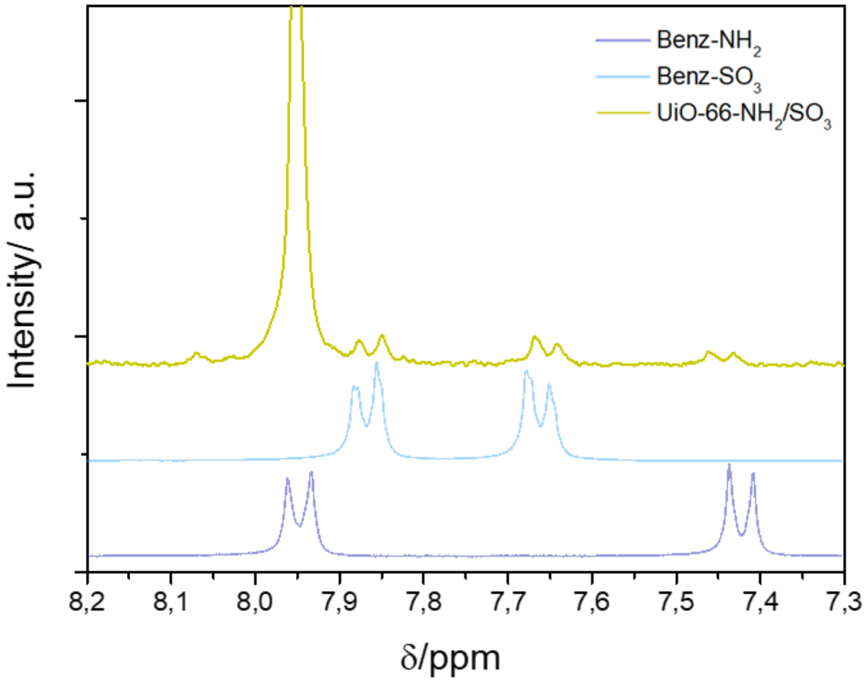

Figure S5: Amplification of ^{1}H NMR profiles acid-digested bimodulated UiO-66-NH_2/SO_3, compared to the free modulators.

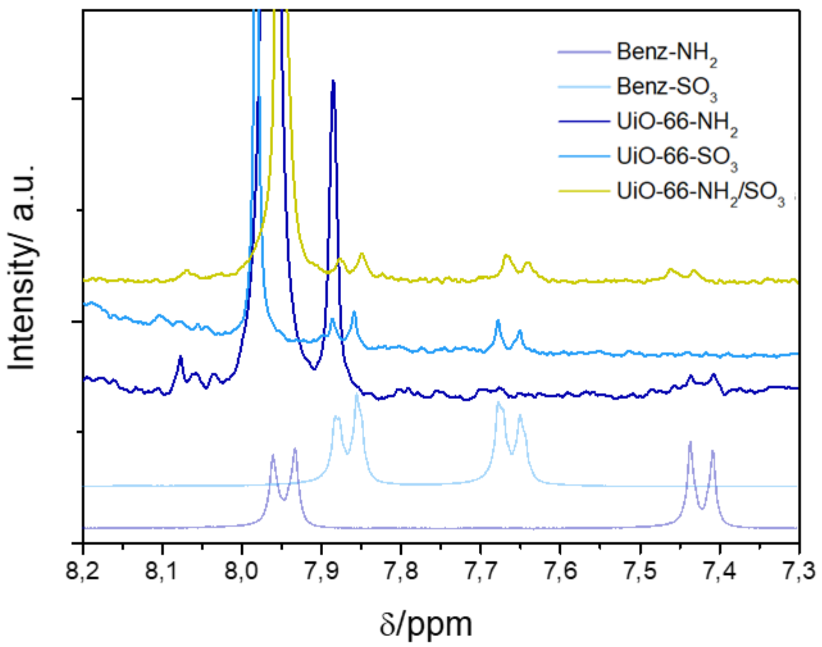

Figure S6: Amplification of ^{1}H NMR profiles acid-digested samples, compared to the free modulators.

Table S2: Tabulated data extracted from acid-digested ^{1}H NMR of activated MTVM UiO-66 MOFs, expressed in molar ratio compared to the linker.

Samples	**NH$_2$/BDC**	**SO$_3$/BDC**	**DMF/BDC**	**AcOH/BDC**	**FA/BDC**
UiO-66-NH$_2$	0.061	n/a	0.204	0.009	0.006
UiO-66-SO$_3$	n/a	0.200	n/a	0.013	0.003
UiO-66-NH$_2$/SO$_3$	0.133	0.317	n/a	0.024	0.001
UiO-66	n/a	n/a	n/a	0.007	0.002

Table S3: Tabulated data extracted from acid-digested ^{1}H NMR of activated MTVM UiO-66 MOFs, expressed in molar percent compared to the linker.

Samples	**%NH$_2$**	**%SO$_3$**	**%AcOH**	**%DMF**	**%FA**
UiO-66-NH$_2$	4.667	n/a	0.890	16.966	0.609
UiO-66-SO$_3$	n/a	16.667	1.316	n/a	0.279
UiO-66-NH$_2$/SO$_3$	11.765	24.089	2.364	n/a	0.133
UiO-66	n/a	n/a	0.725	n/a	0.171

S.3.3 Fourier transformed Infra-Red (FT-IR)

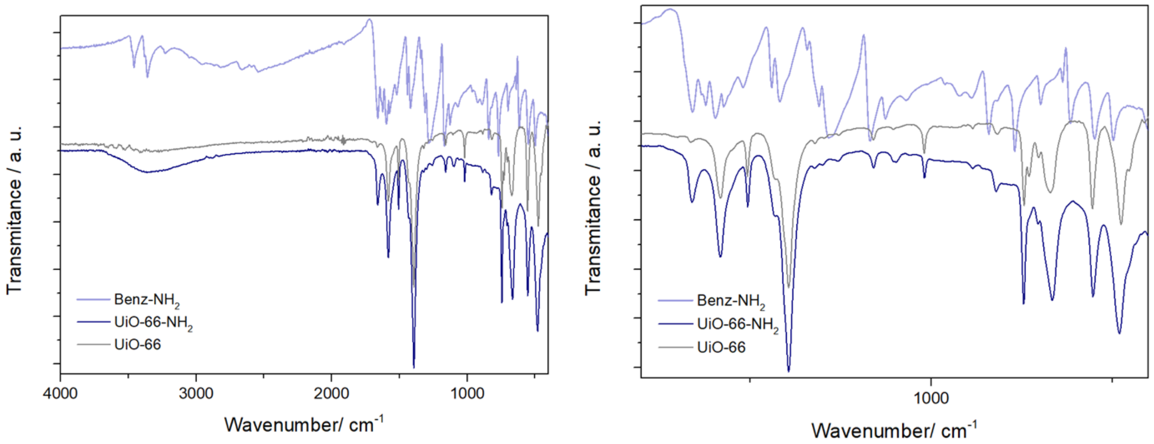

Figure S7: FT-IR profiles of UiO-66-NH$_2$ compared to pristine UiO-66 and Benz-NH$_2$ modulator. Given the low quantity of Benz-NH$_2$ incorporated, its FT-IR signals (NH$_2$ $_{st}$, at *ca.* 3600-3000cm^{-1}; NH$_2$ δ at *ca.* 1600 cm^{-1}; C-N $_{st}$ at ca. 1200 cm^{-1}and NH$_2$ δ at 900-700cm^{-1}) are masked by the MOF's signals.

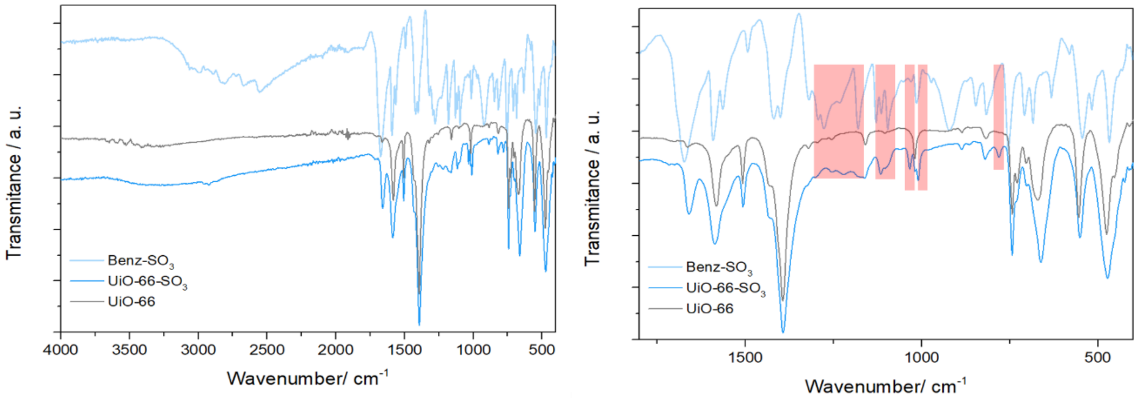

Figure S8: FT-IR profiles of UiO-66-SO$_3$ compared to pristine UiO-66 and Benz- SO$_3$ modulator. In agreement with previous work on Benz-SO$_3$ modulation, UiO-66-SO$_3$ displayed new bands attributed to asymmetric and symmetric stretching frequencies of sulfonate,[2] at 1115 ($\nu_{as}SO_3$), 1032 ($\nu_{as}SO_3$) and 1010 ($\nu_{s}SO_3$) cm^{-1}. These bands are shifted in comparison with the free modulator due to the partial attachment of sulfonate groups to Zr clusters. A new band at 780 cm^{-1} (C-S stretching) is observed in the FT-IR spectra of SO$_3$-containing-MOF.

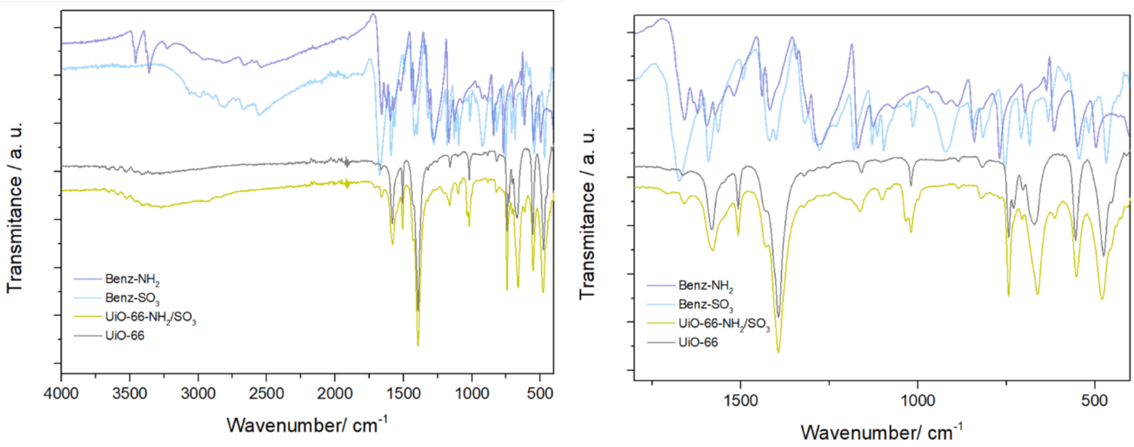

Figure S9: FT-IR profiles of UiO-66-NH$_2$/SO$_3$ compared to pristine UiO-66, Benz-NH$_2$ and Benz-SO$_3$ modulators.

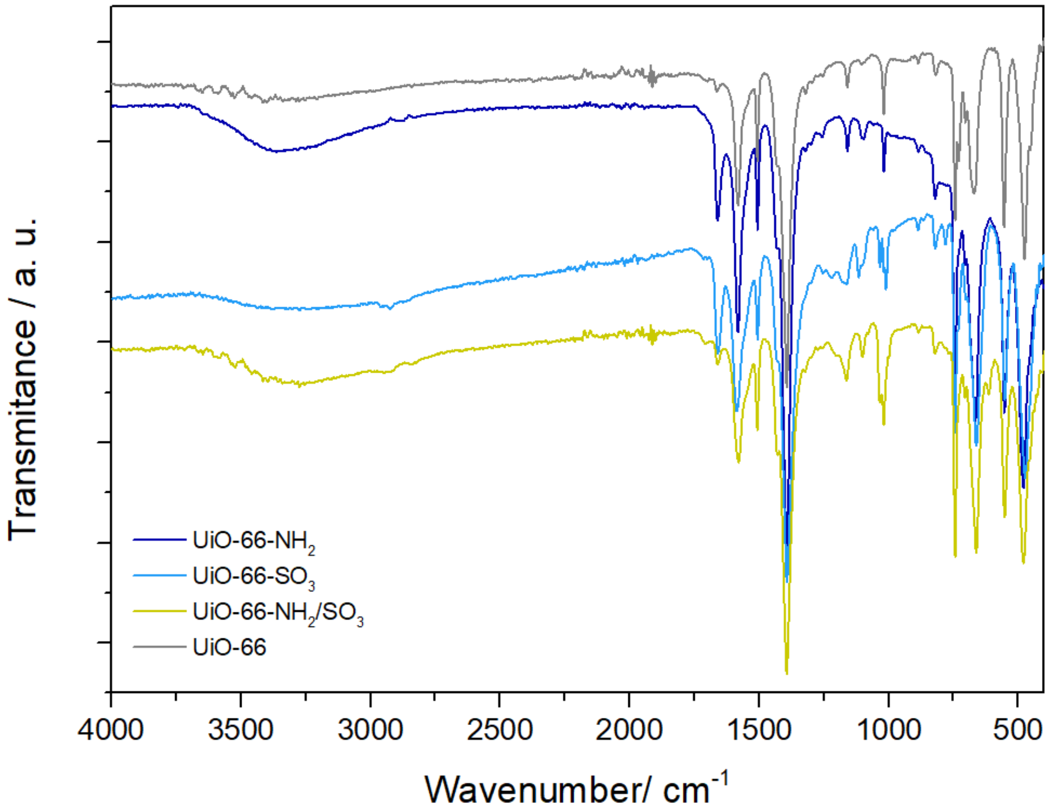

Figure S10: Comparison of FT-IR profiles.

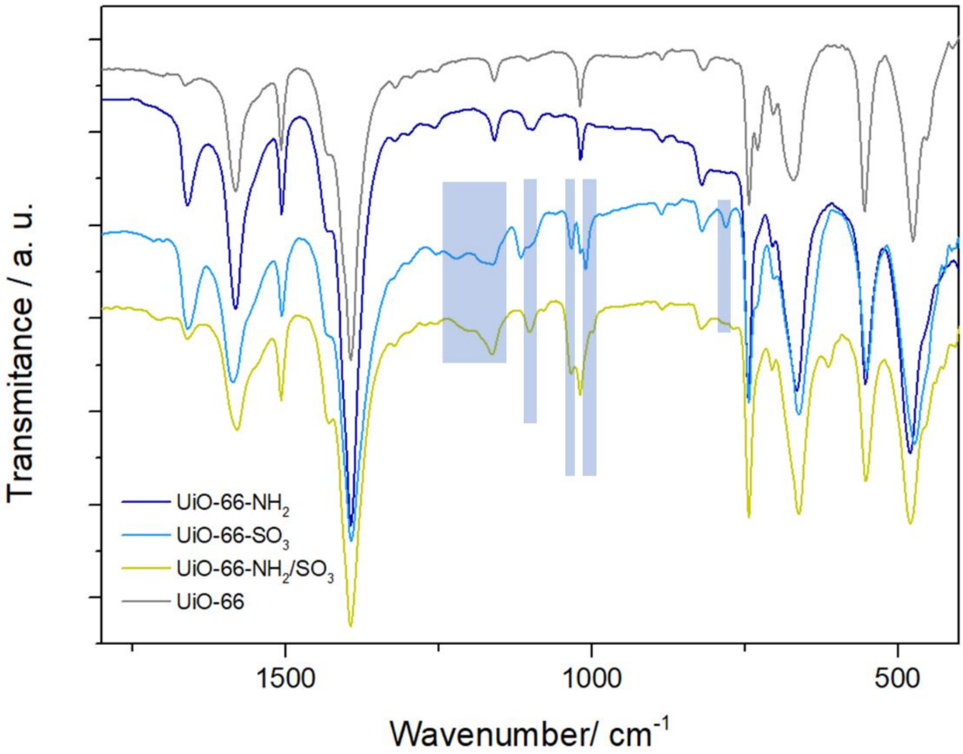

Figure S11: Comparison of amplified FT-IR profiles.

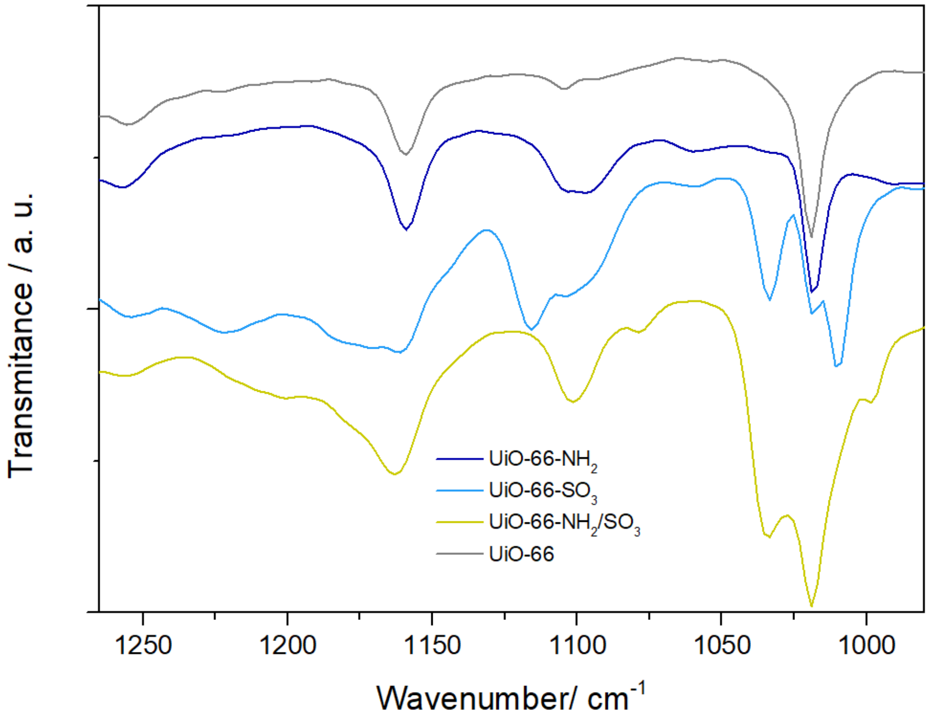

Figure S12: Comparison of amplified FT-IR profiles of single-modulated and bi-modulated samples, showing shifting of the signals related to the sulfonate in the di-modulated sample - originally at ca. 1115 ($\nu_{as}SO_3$), 1032 ($\nu_{as}SO_3$) and 1010 ($\nu_{s}SO_3$) cm^{-1} in UiO-66-SO$_3$ - suggesting a possible interaction between Benz-NH$_2$ and Benz-SO$_3$ modulators. Benz-NH$_2$ signals (C-N $_{st}$ at ca. 1179 cm^{-1} and the NH$_2$ δ at 861 cm^{-1} and ca. 798 cm^{-1}) are masked by the framework's signals.

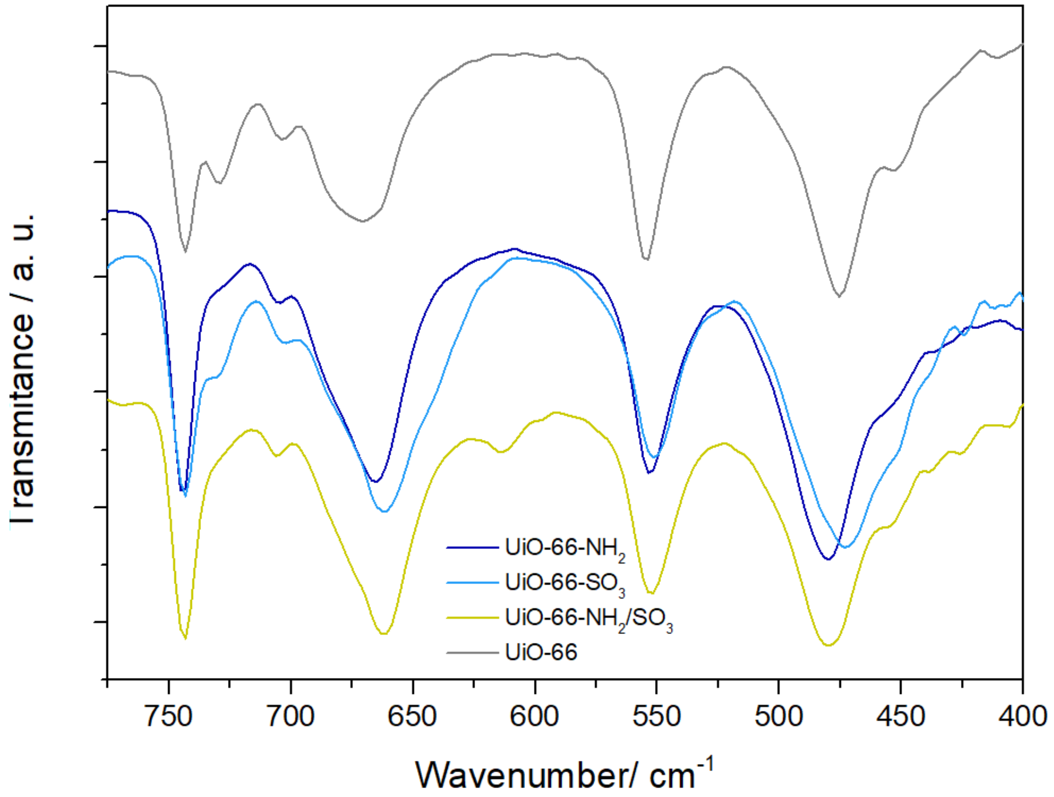

Figure S13: Comparison of amplified FT-IR profiles of single-modulated and bi-modulated samples, showing shifting of the signals related to Zr_6 clusters[3] due to modulators' attachment.

S.3.4 Thermogravimetric analysis (TGA)

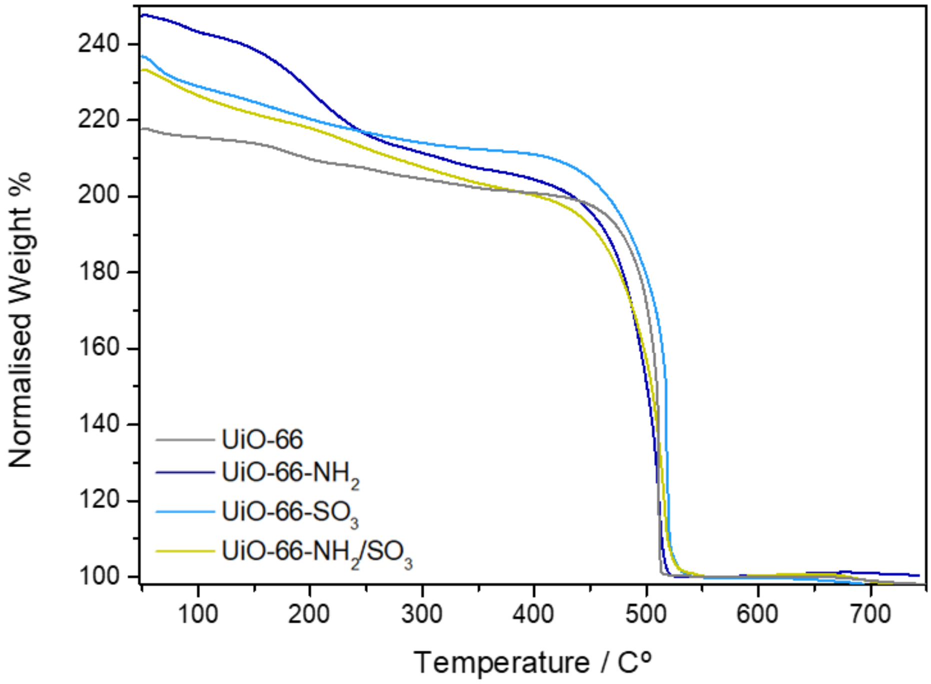

Figure S14: TGA profiles(air) of the activated samples compared to pristine UiO-66, with the end of the decomposition profiles (residue) normalised to 100%.

Table S4: Data extracted from TGA analysis[4] for the model framework $[Zr_6(O)_4(OH)_4(BDC)_X(Mod1)_y(Mod2)_z(FA)_A(AcOH)_B(OH)_C(DMF)_D(H2O)_E]$. Data provided per Zr

Sample	L	NH$_2$	SO$_3$Na	AcOH	DMF	FA	OH	H$_2$O
UiO-66	0.857	0.000	0.000	0.003	0.000	0.005	0.279	0.279
UiO-66-NH$_2$	0.824	0.050	0.000	0.007	0.168	0.002	0.291	0.123
UiO-66-SO3	0.751	0.000	0.150	0.010	0.000	0.001	0.337	0.337
UiO-66-NH$_2$/SO$_3$	0.596	0.079	0.189	0.009	0.000	0.001	0.529	0.529

Table S5: Data extracted from TGA analysis for the model framework $[Zr_6(O)_4(OH)_4(BDC)_X(Mod1)_y(Mod2)_z(FA)_A(AcOH)_B(OH)_C(DMF)_D(H_2O)_E]$.

Sample	ML%	Mod/mL	Total/ml
UiO-66	14.33	0.000	0.61
UiO-66-NH$_2$	17.57	0.286	1.64
UiO-66-SO$_3$	24.89	0.604	0.64
UiO-66-NH$_2$/SO$_3$	40.36	0.665	0.85

S.3.5 Scanning Electron Microscopy (SEM)

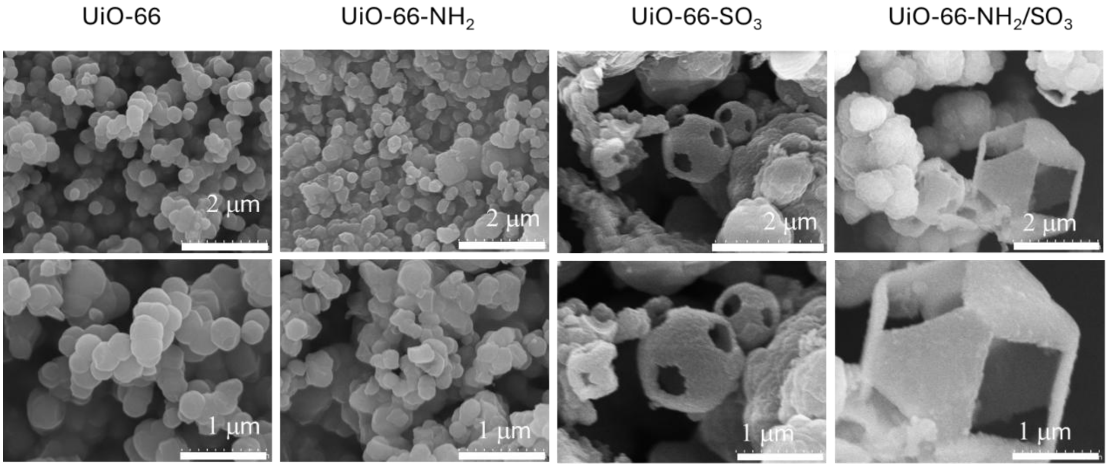

Figure S15: SEM images of modulated MOFs and pristine UiO-66.

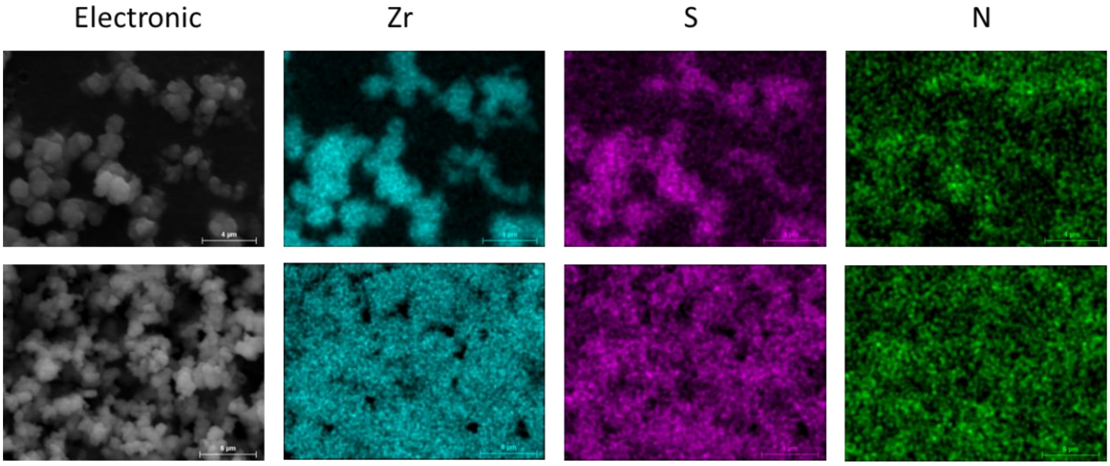

Figure S16: EDX mapping images of the UiO-66-NH$_2$/SO$_3$, showing general homogenous distribution of N and S within the sample.

S.3.6 Z-potential

The positive Z-potential of pristine UiO-66 is increased upon Benz-NH_2 incorporation, whereas Benz-SO_3 provides a negative Z-potential to UiO-66-SO_3, indicating the presence of unbonded SO_3 groups. UiO-66-NH_2/SO_3 does not exhibit two distinct Z-potential contributions (one negative and one positive) from separately functionalised samples, as observed in our control mixture of UiO-66-NH_2 and UiO-66-SO_3. Instead, it shows an overall positive Z-potential, where the combined influence of the framework and Benz-NH_2 outweighs the negative charge contributed by Benz-SO_3.

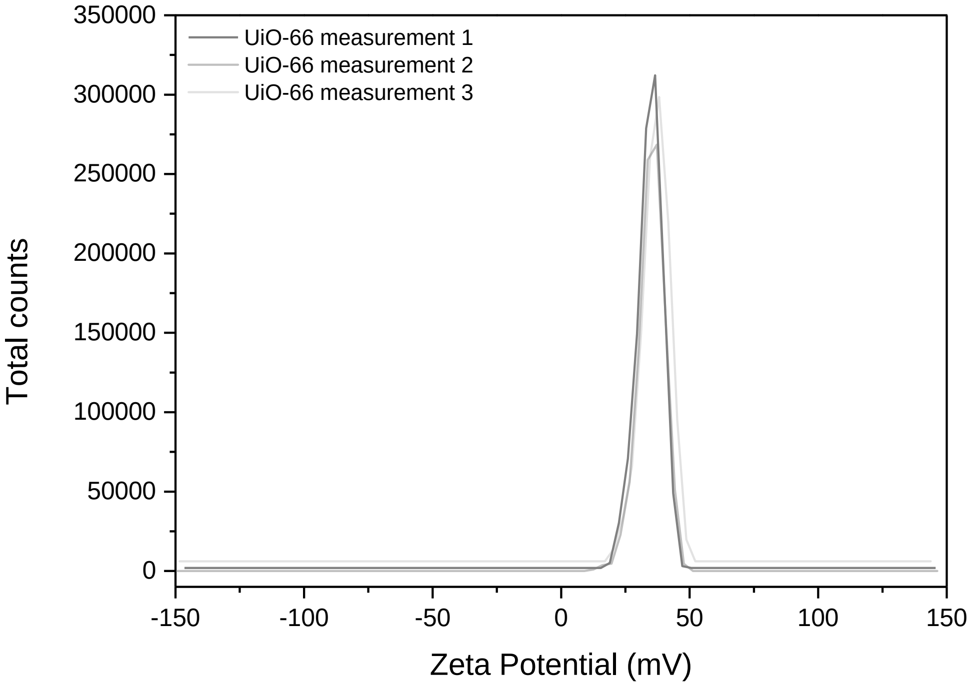

Figure S17: Z-potential of UiO-66 in water.

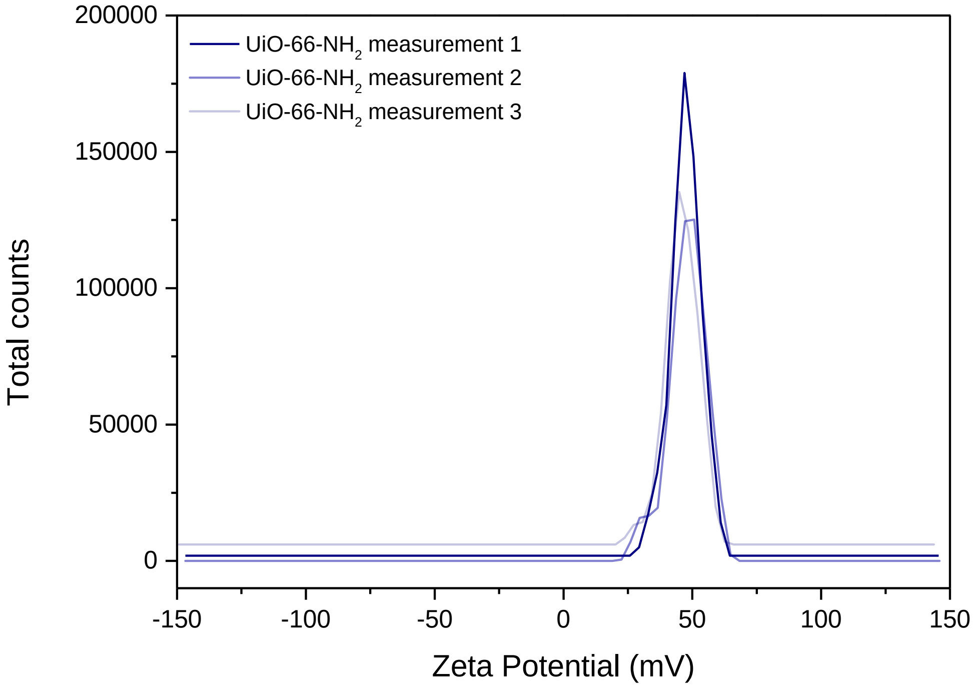

Figure S18: Z-potential of UiO-66-NH$_2$ in water.

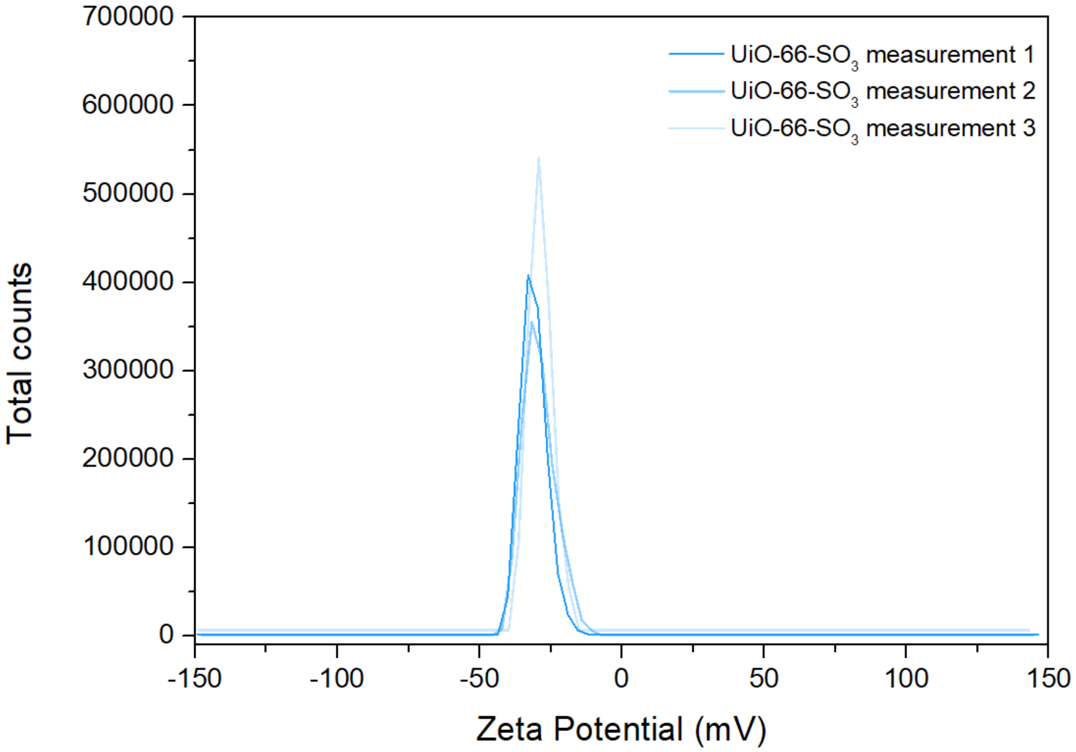

Figure S19: Z-potential of UiO-66-SO$_3$ in water.

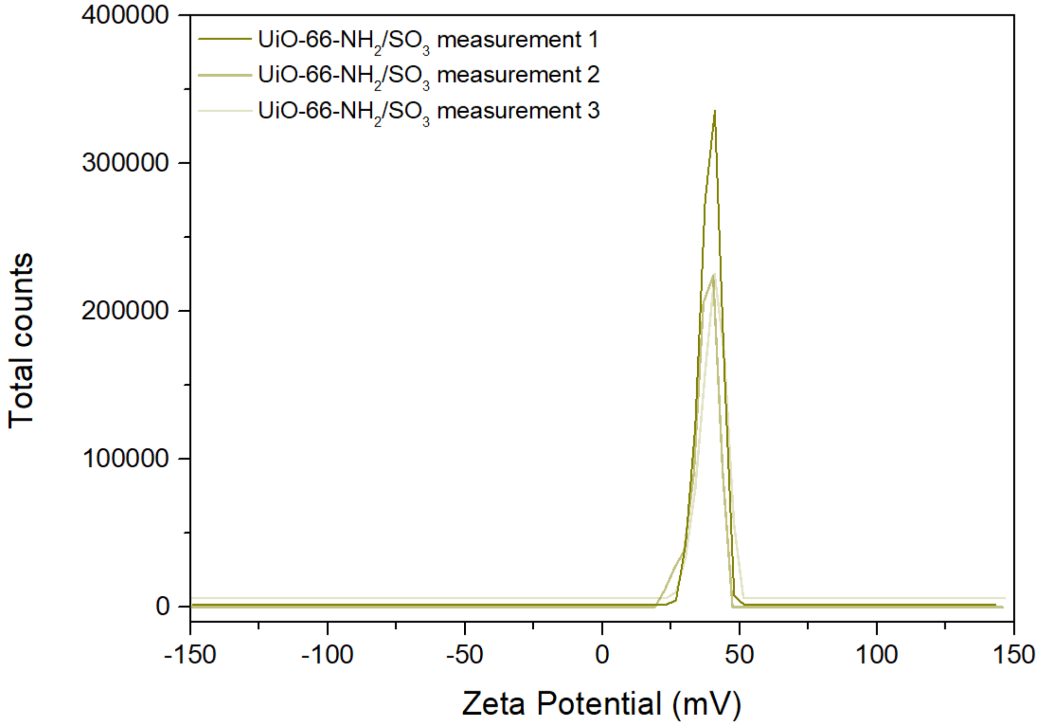

Figure S20: Z-potential of UiO-66-NH$_2$/SO$_3$ in water.

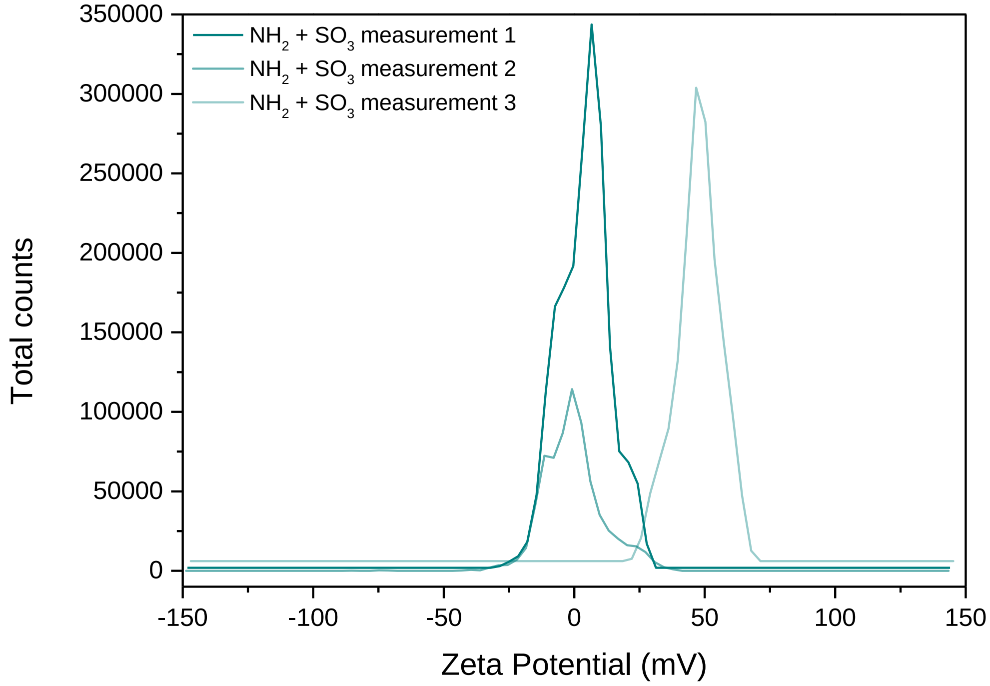

Figure S21: Z-potential of physical mixture of UiO-66-NH$_2$ and UiO-66-SO$_3$ in water.

Table S6: Average and standard deviation values of Z-potential extracted from three measurements.

	Mean / eV	**Standard Deviation / eV**
UiO-66	35.46	1.19
UiO-66-NH_2	47.10	1.07
UiO-66-SO_3	-29.68	1.24
UiO-66-NH_2/SO_3	38.88	1.41
UiO-66-NH_2 + UiO-66-SO_3	16.65	27.00

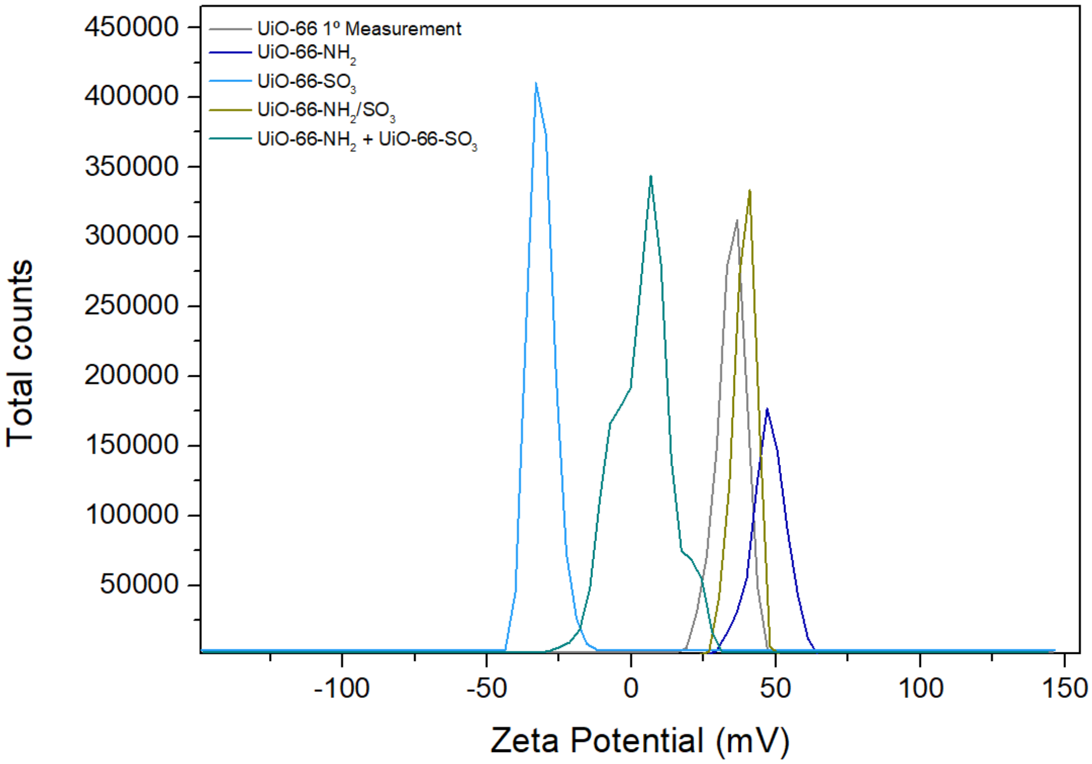

Figure S22: Comparison of the first measurement of Z-potential of UiO-66 samples.

S.3.7 Characterisation of MTVM MOFs stability in different solvents

Stability protocol: 10 mg of a new batch of activated MOF (UiO-66, UiO-66-NH_2, UiO-66-SO_3H, and UiO-66-NH_2/SO_3) were dispersed in 10 mL of solvent upon sonication (2 minutes) and the samples were stirred for 24 hours. After that, the materials were centrifuged (7000 rpm, 7 min) and dried at 50ºC. Note that the MOFs were activated using the same procedure in Methanol (See section SX) prior to solvent stability studies.

S.3.7.1 Solvent stability of UiO-66

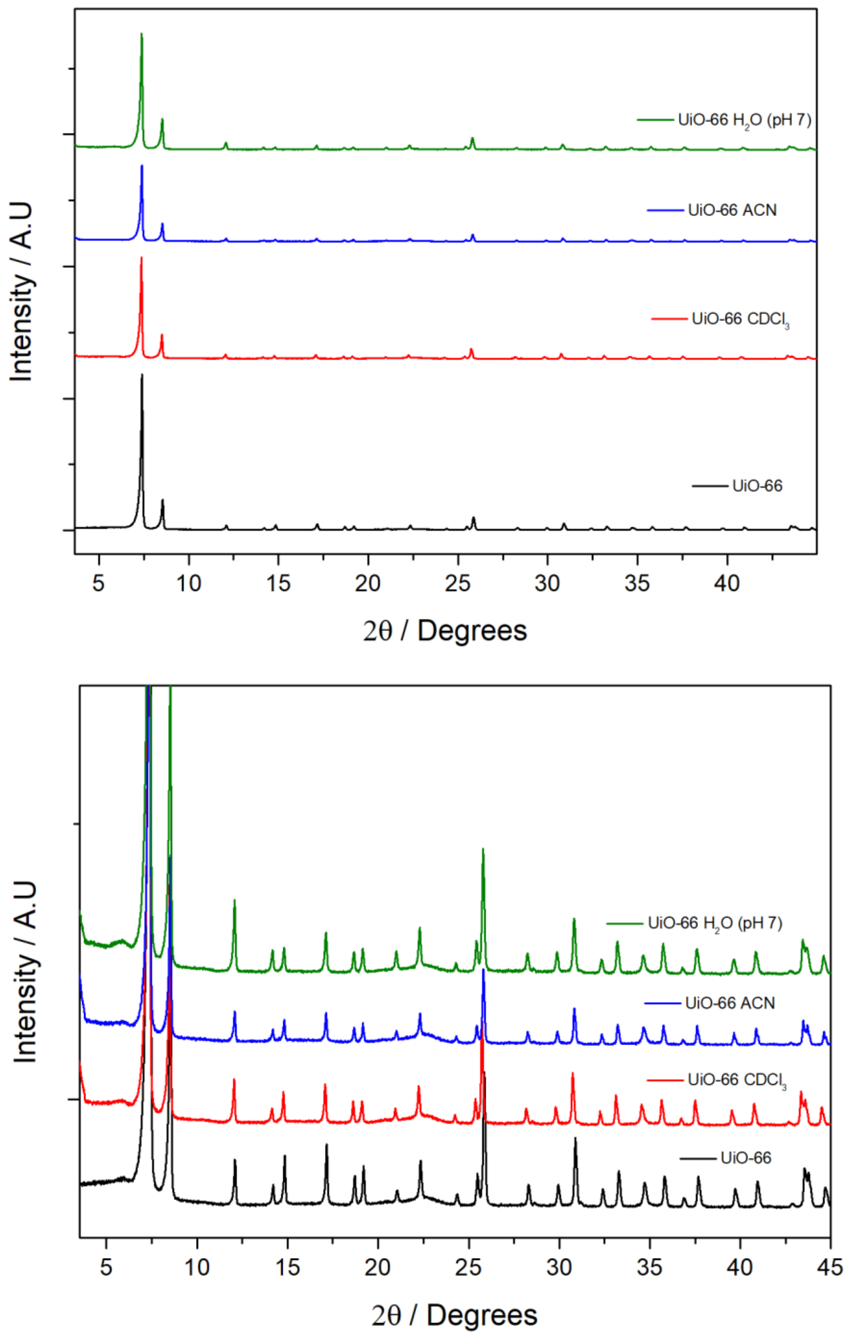

Figure S23: PXRD patterns of UiO-66 before and after stirring in different solvents for 24h.

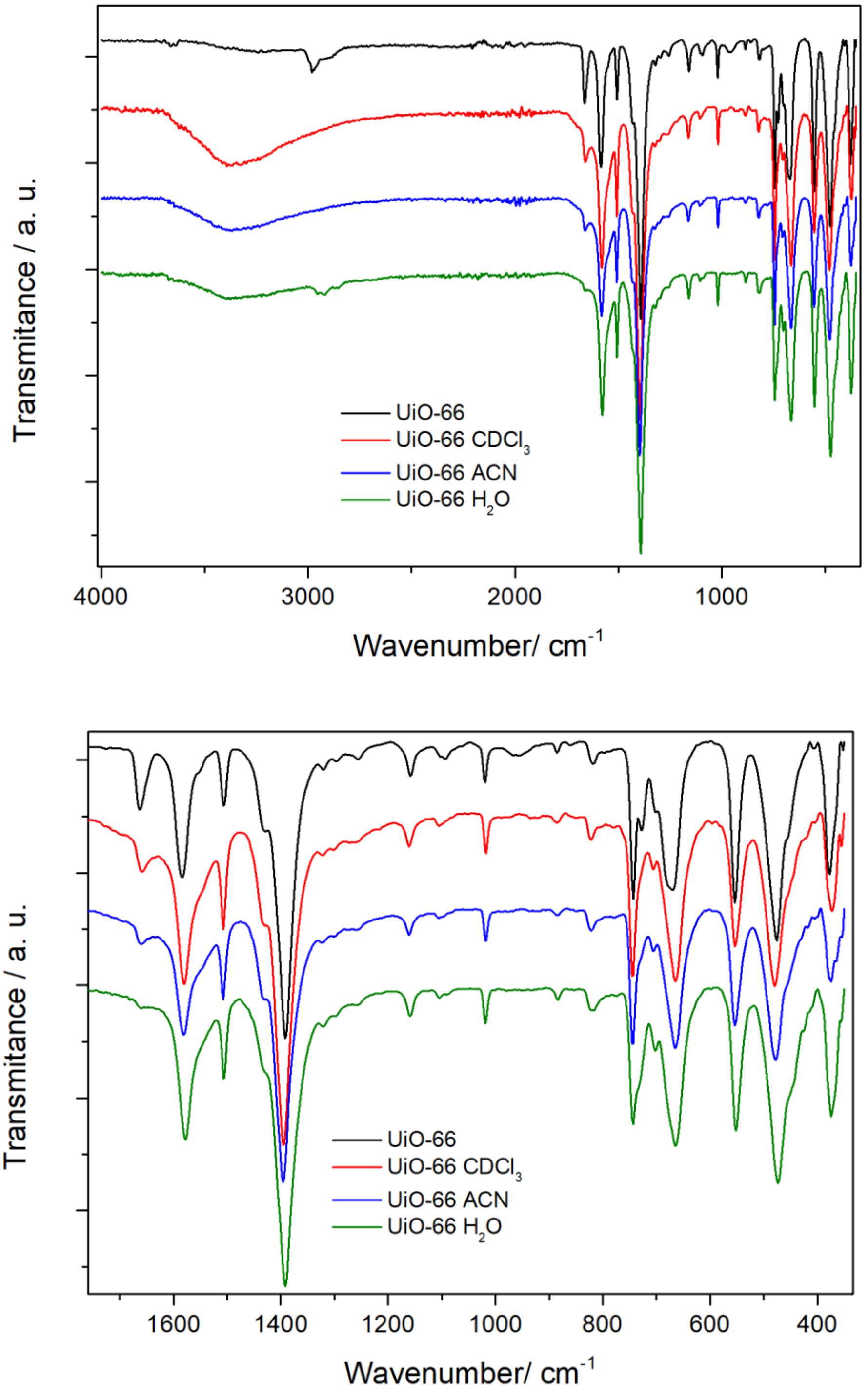

Figure S24: FT-IR profiles of UiO-66 before and after stirring in different solvents for 24h.

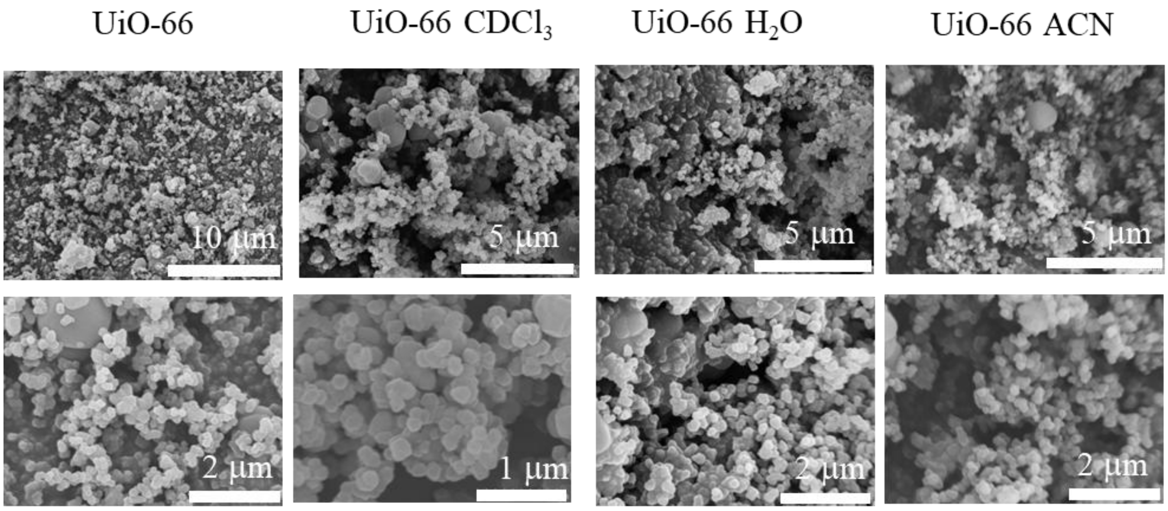

Figure S25: SEM images of UiO-66 before and after stirring in different solvents for 24h.

S.3.7.2 Solvent stability of UiO-66-NH_2

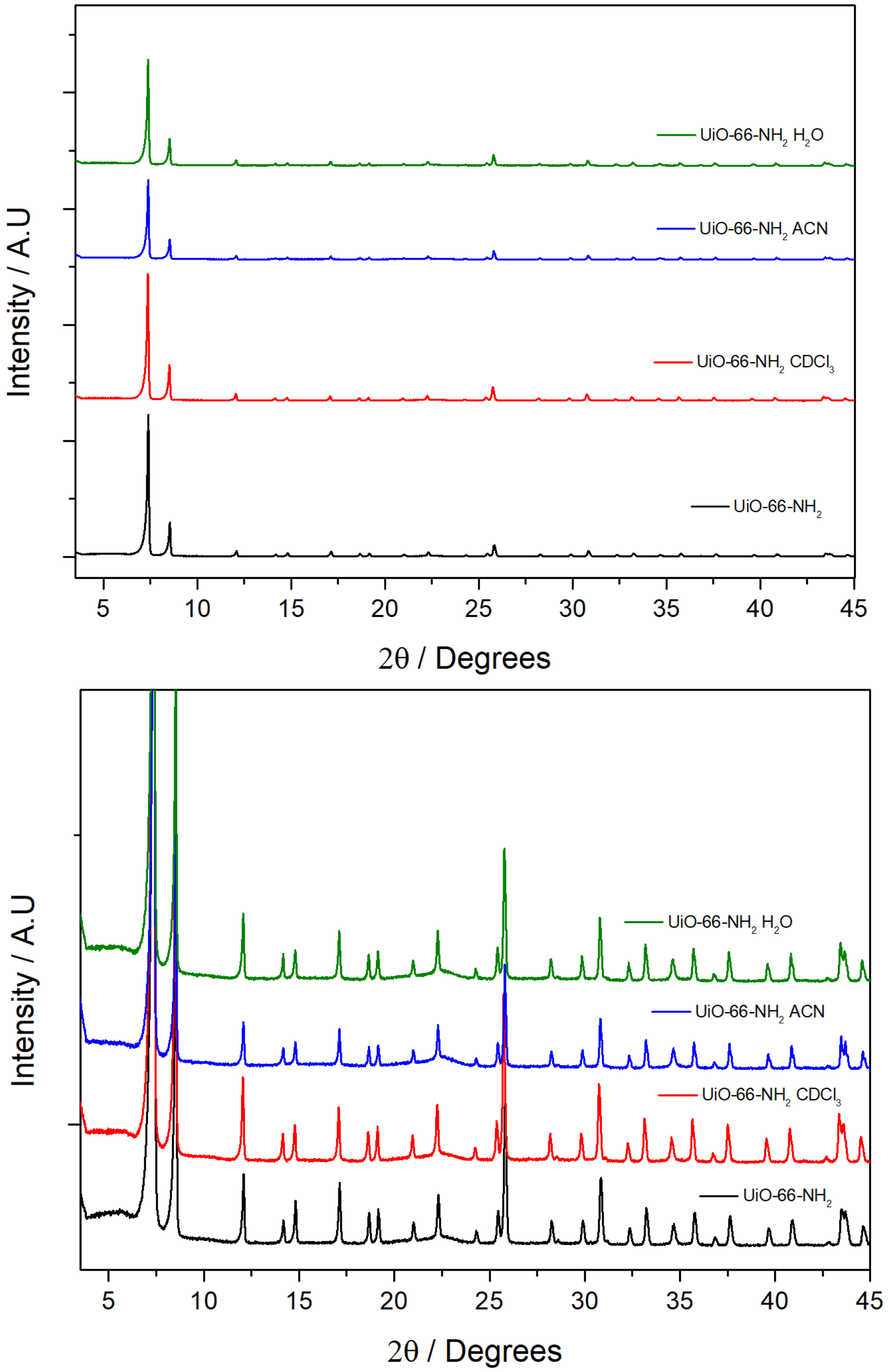

Figure S26: PXRD patterns of UiO-66-NH_2 before and after stirring in different solvents for 24h.

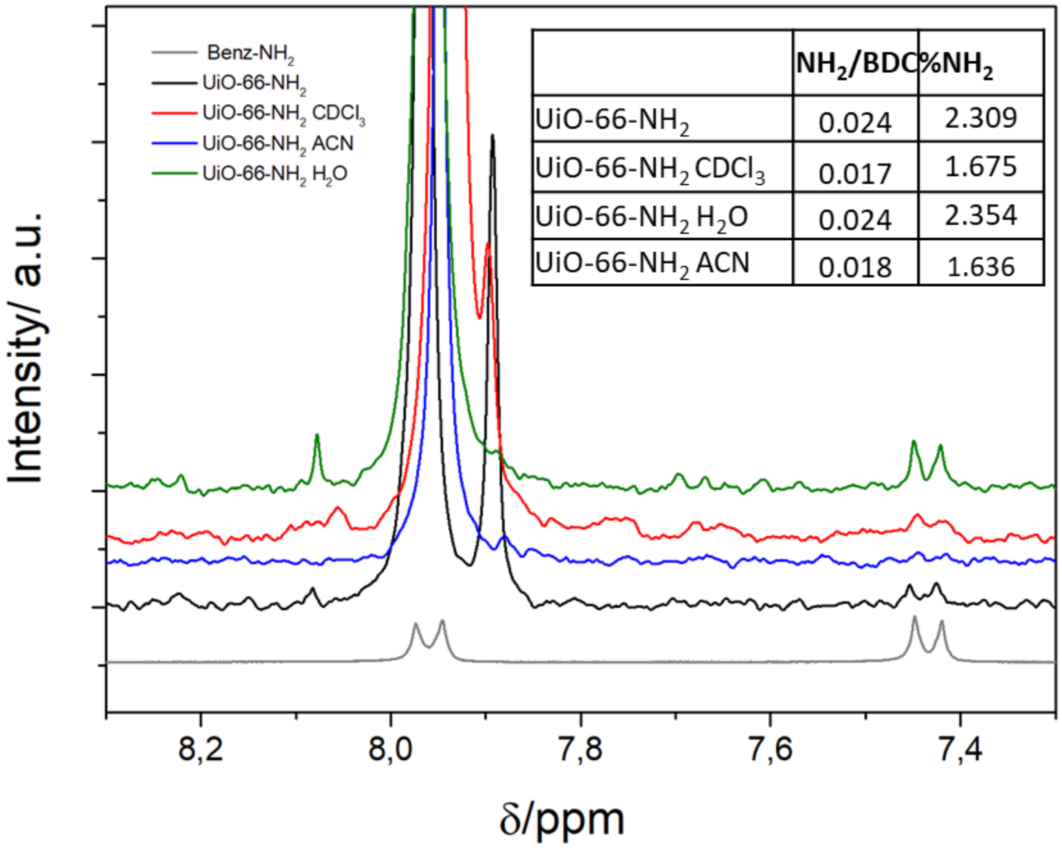

	NH_2/BDC	%NH_2
UiO-66-NH_2	0.024	2.309
UiO-66-NH_2 $CDCl_3$	0.017	1.675
UiO-66-NH_2 H_2O	0.024	2.354
UiO-66-NH_2 ACN	0.018	1.636

Figure S27: ^{1}H NMR profiles acid-digested UiO-66-NH_2, compared to the free modulator, showing the presence of Benz-NH_2 after solvent treatment. It is important to note that due to the low integration of modulator signals in comparison to the linker, we consider the values provided as an estimation, which proves the retention of modulators' after the solvent treatment.

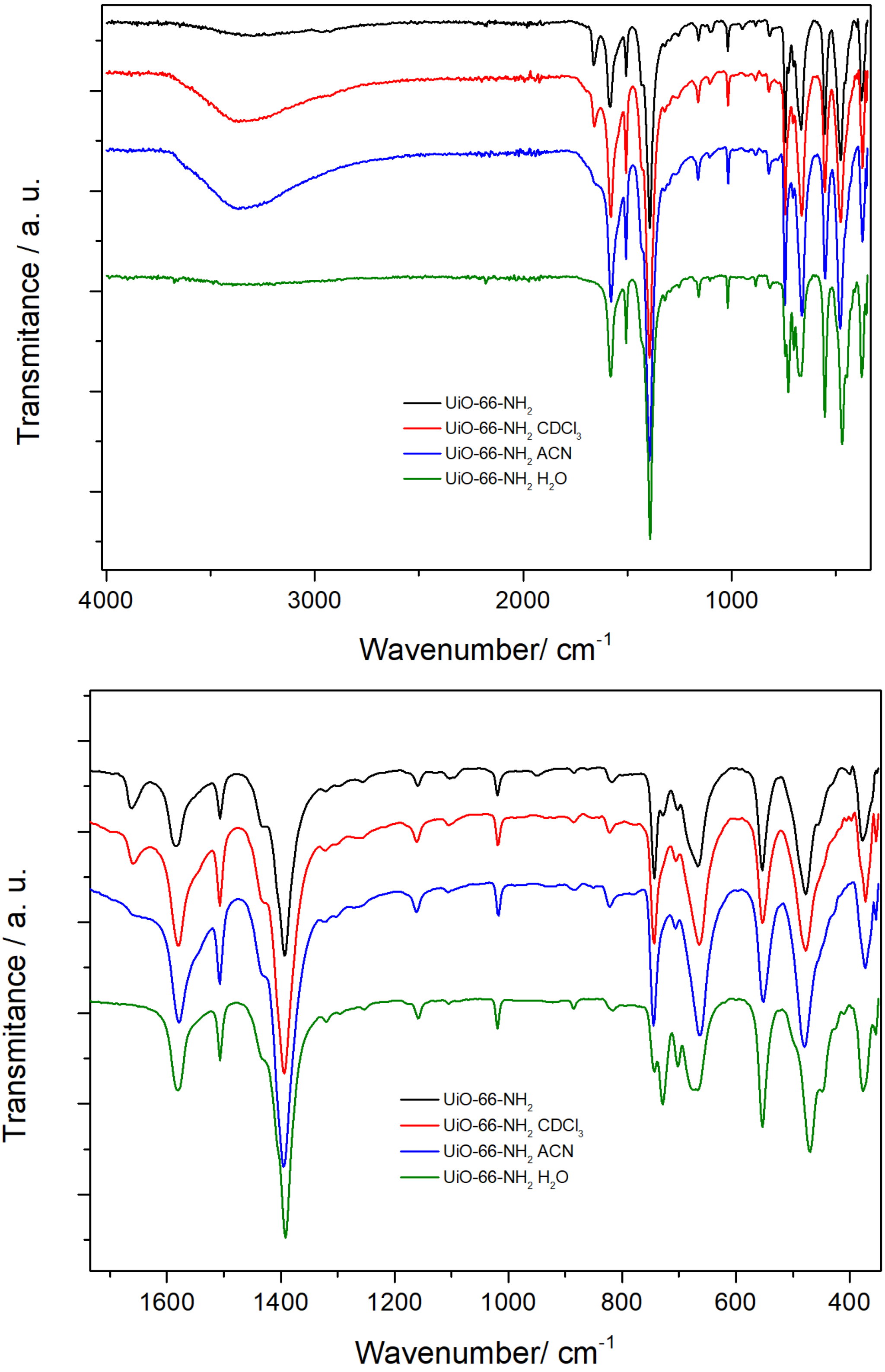

Figure S28: FT-IR profiles of UiO-66-NH$_2$ after 24h on five different solvents.

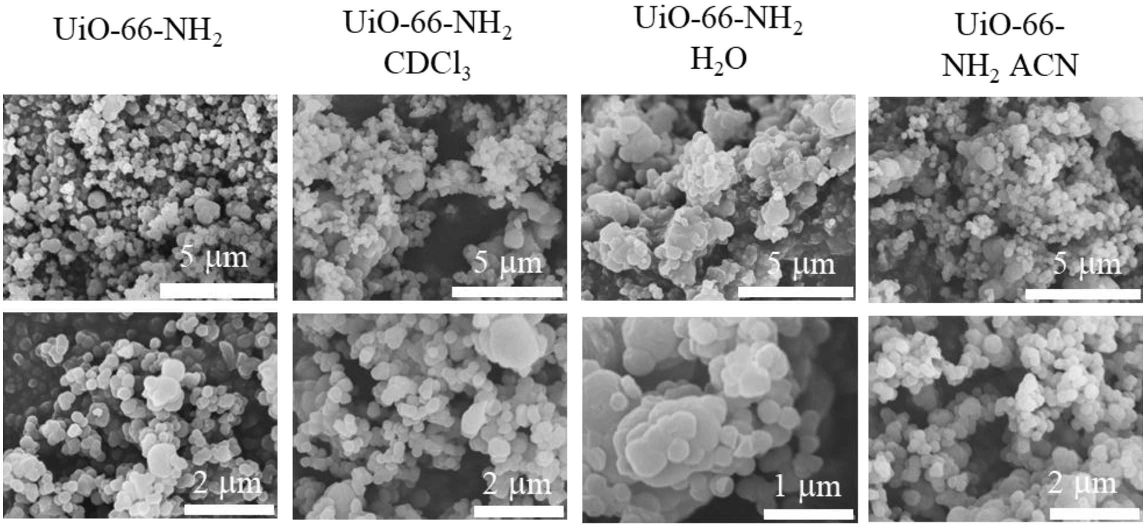

Figure S29: SEM images of UiO-66-NH$_2$ before and after stirring in different solvents for 24h.

S.3.7.3 Solvent stability of UiO-66-SO_3

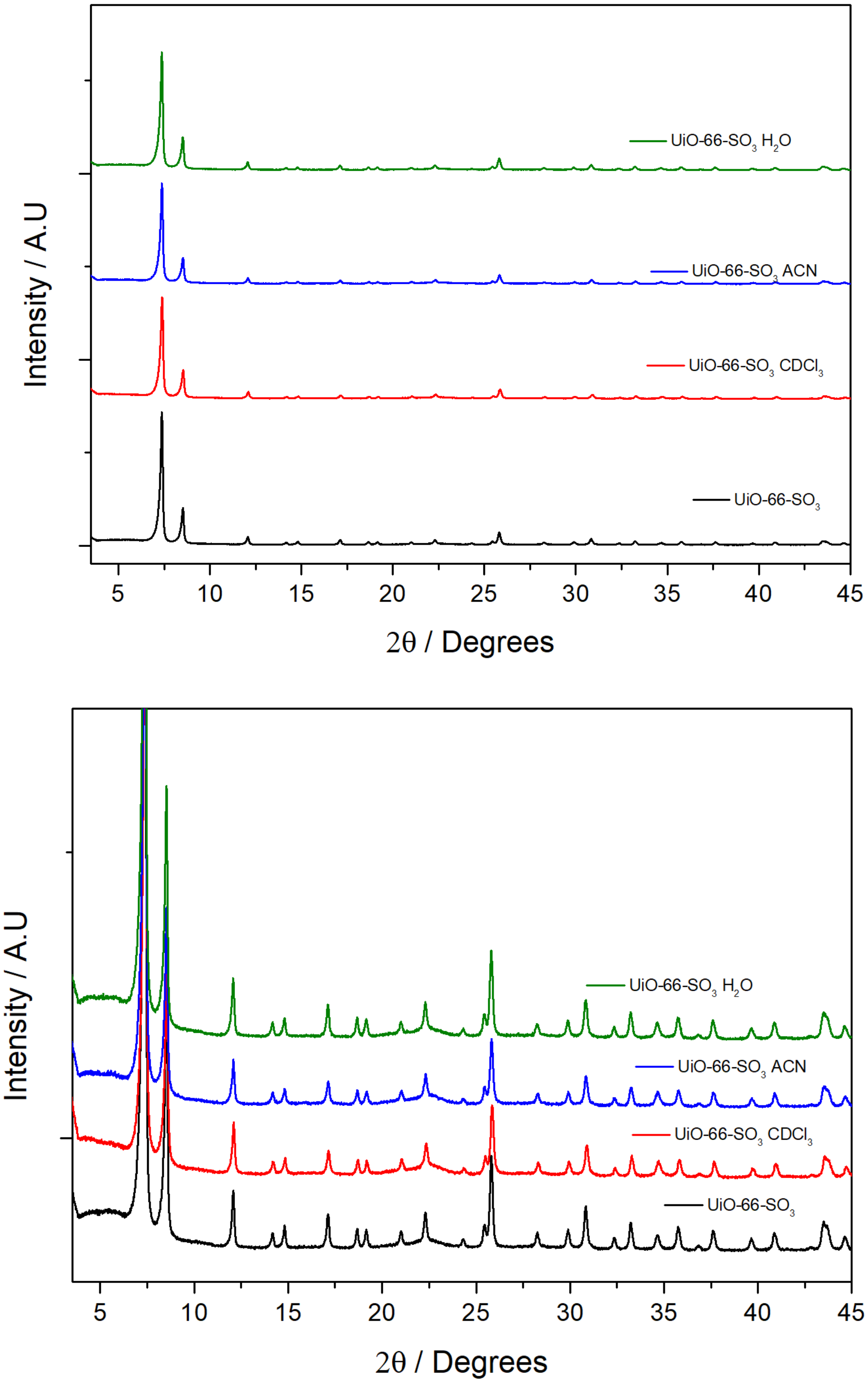

Figure S30: PXRD patterns of UiO-66-SO_3 before and after stirring in different solvents for 24h.

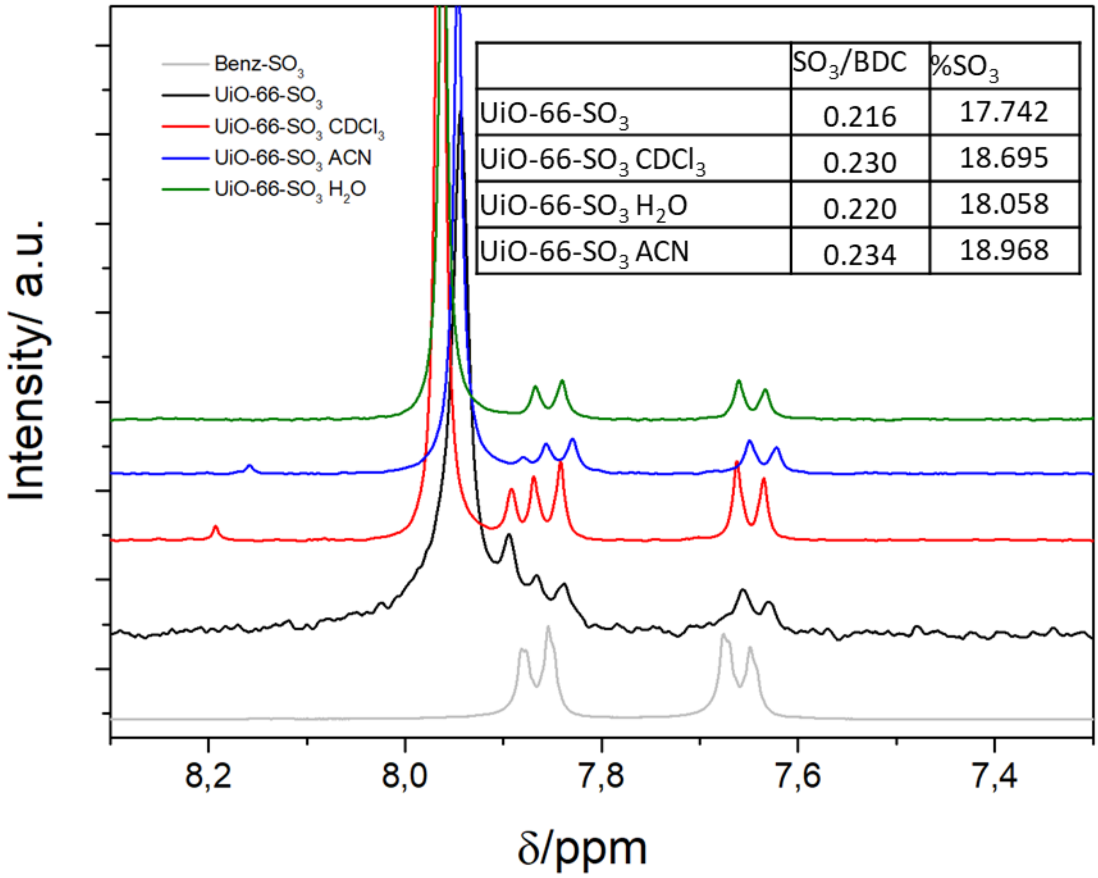

	SO_3/BDC	%SO_3
UiO-66-SO_3	0.216	17.742
UiO-66-SO_3 $CDCl_3$	0.230	18.695
UiO-66-SO_3 H_2O	0.220	18.058
UiO-66-SO_3 ACN	0.234	18.968

Figure S31: ^{1}H NMR profiles acid-digested UiO-66-SO_3, compared to the free modulator, showing the presence of modulator after solvent treatment. It is important to note that due to the low integration of modulator signals in comparison to the linker, we consider the values provided as an estimation, which proves the retention of modulators' after the solvent treatment. The attachment is confirmed by maintained FT-IR bands (Figure S32).

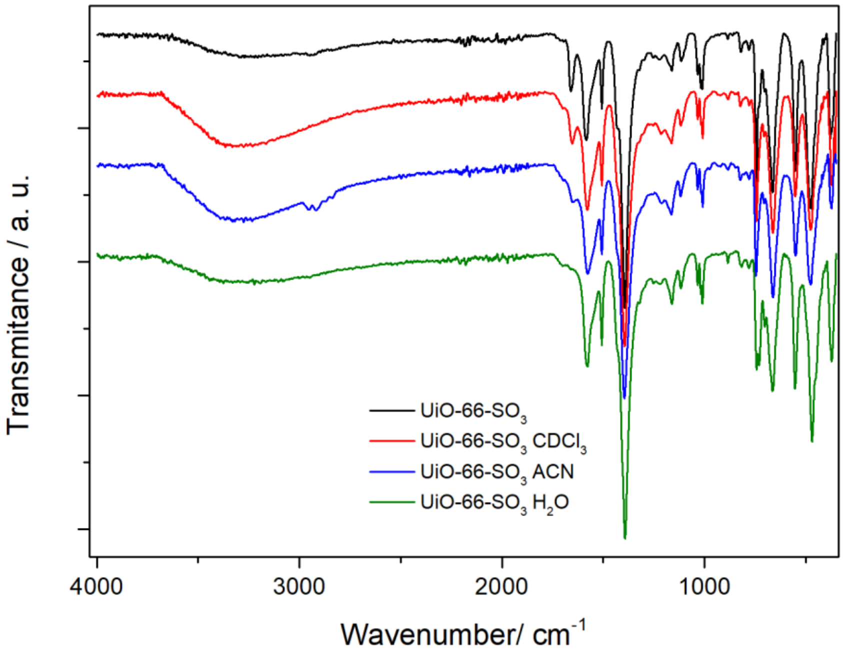

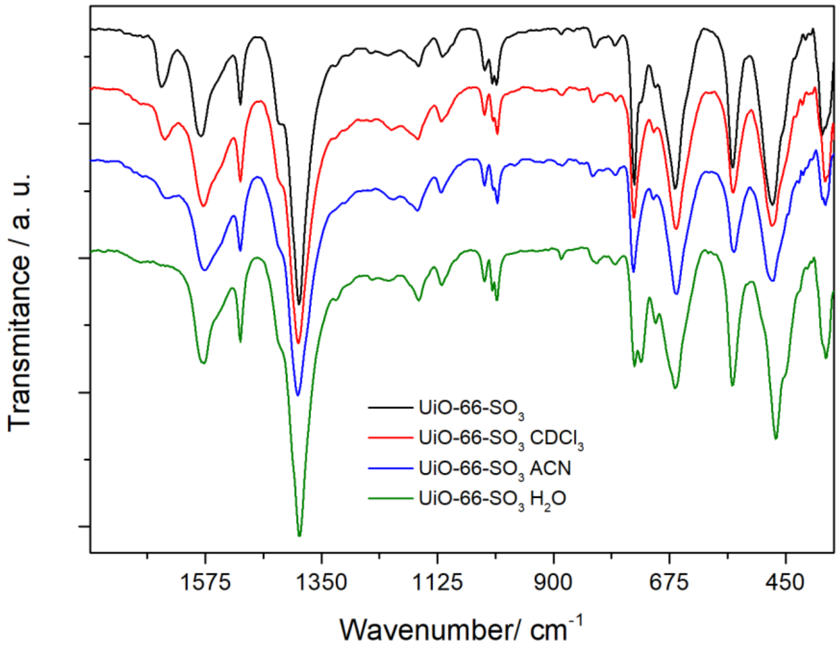

Figure S32: FT-IR profiles of UiO-66-SO_3 before and after stirring in different solvents for 24h.

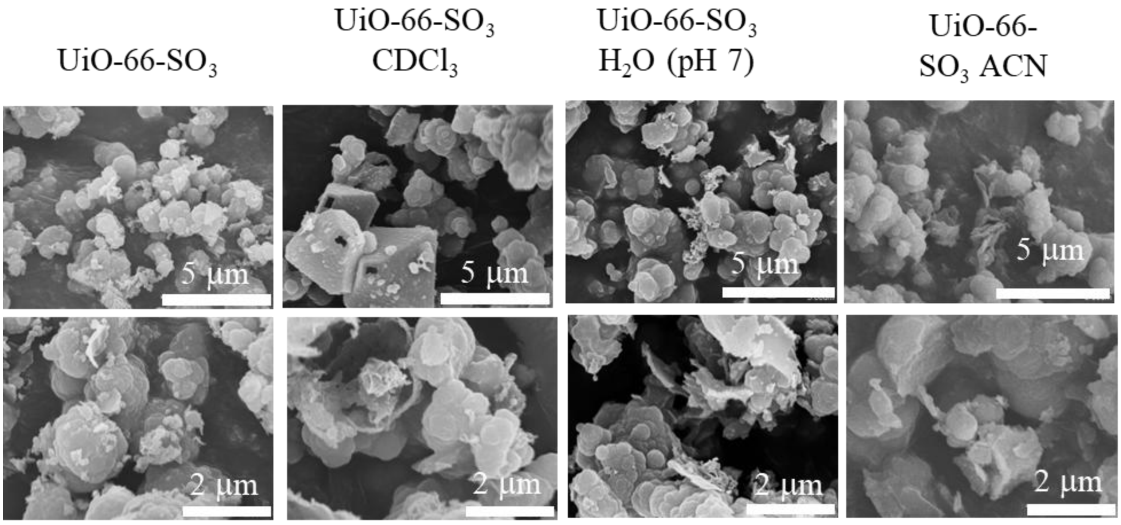

Figure S33: SEM images of UiO-66-SO_3 before and after stirring in different solvents for 24h.

S.3.7.4 Solvent stability of UiO-66-NH_2/SO_3

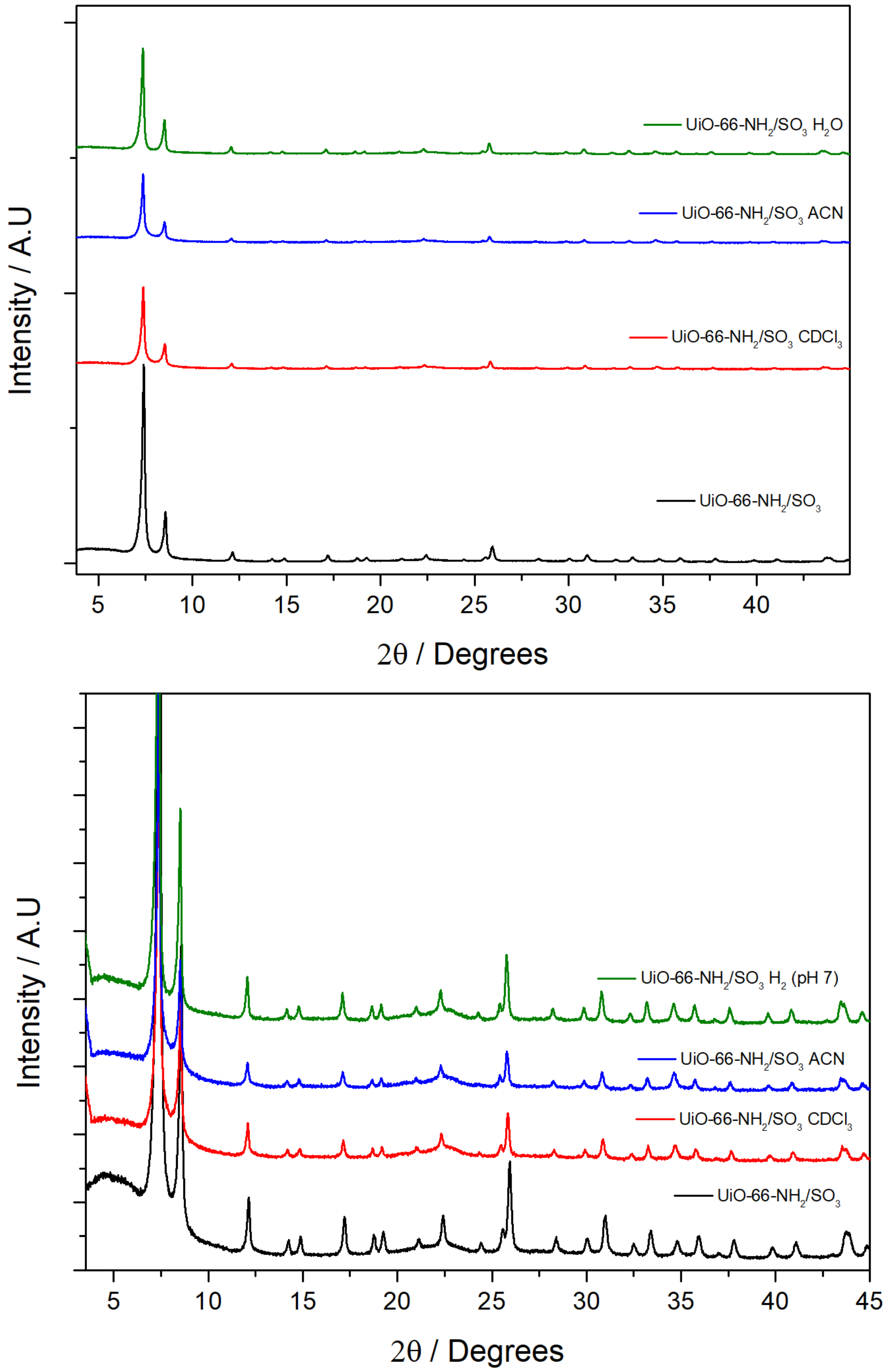

Figure S34: PXRD patterns of UiO-66-NH_2/SO_3 before and after stirring in different solvents for 24h.

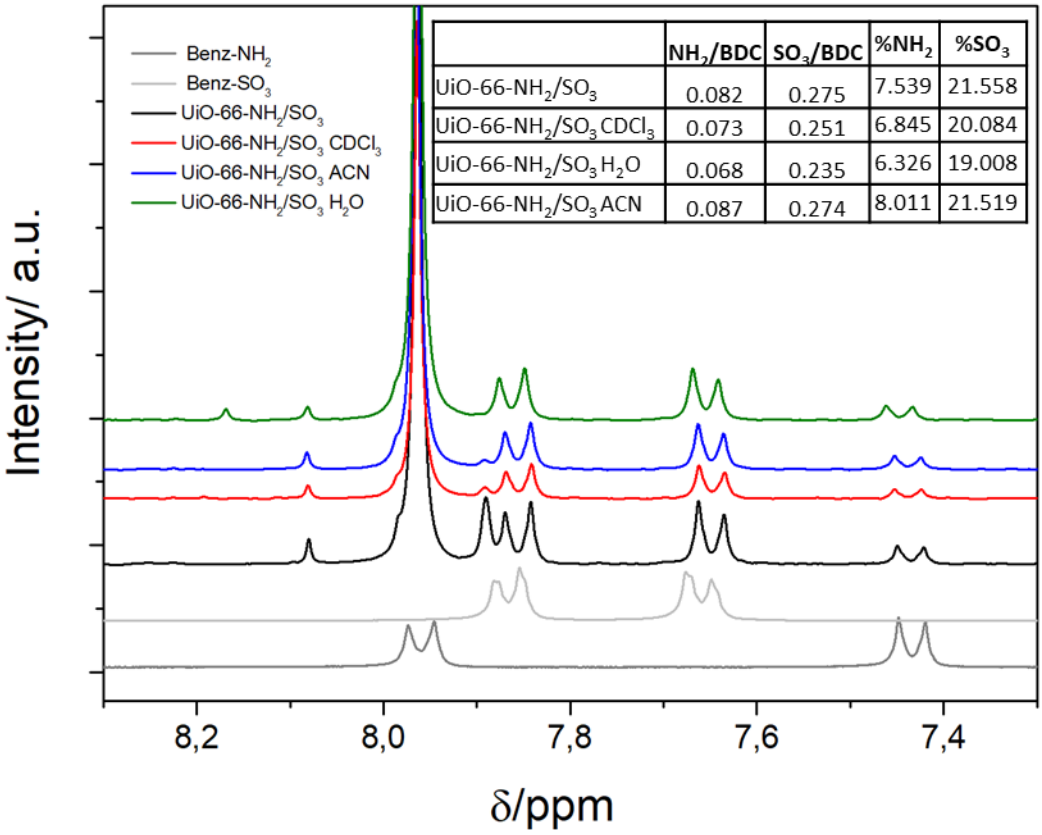

	NH_2/BDC	SO_3/BDC	%NH_2	%SO_3
UiO-66-NH_2/SO_3	0.082	0.275	7.539	21.558
UiO-66-NH_2/SO_3 $CDCl_3$	0.073	0.251	6.845	20.084
UiO-66-NH_2/SO_3 H_2O	0.068	0.235	6.326	19.008
UiO-66-NH_2/SO_3 ACN	0.087	0.274	8.011	21.519

Figure S35: ^{1}H NMR profiles acid-digested UiO-66-NH_2/SO_3, compared to the free modulator, showing insignificant decrease in modulator content upon solvent treatment.It is important to note that due to the low integration of modulator signals in comparison to the linker, we consider the values provided as an estimation, which proves the retention of modulators' after the solvent treatment. The attachment is confirmed by maintained FT-IR bands (Figure S36).

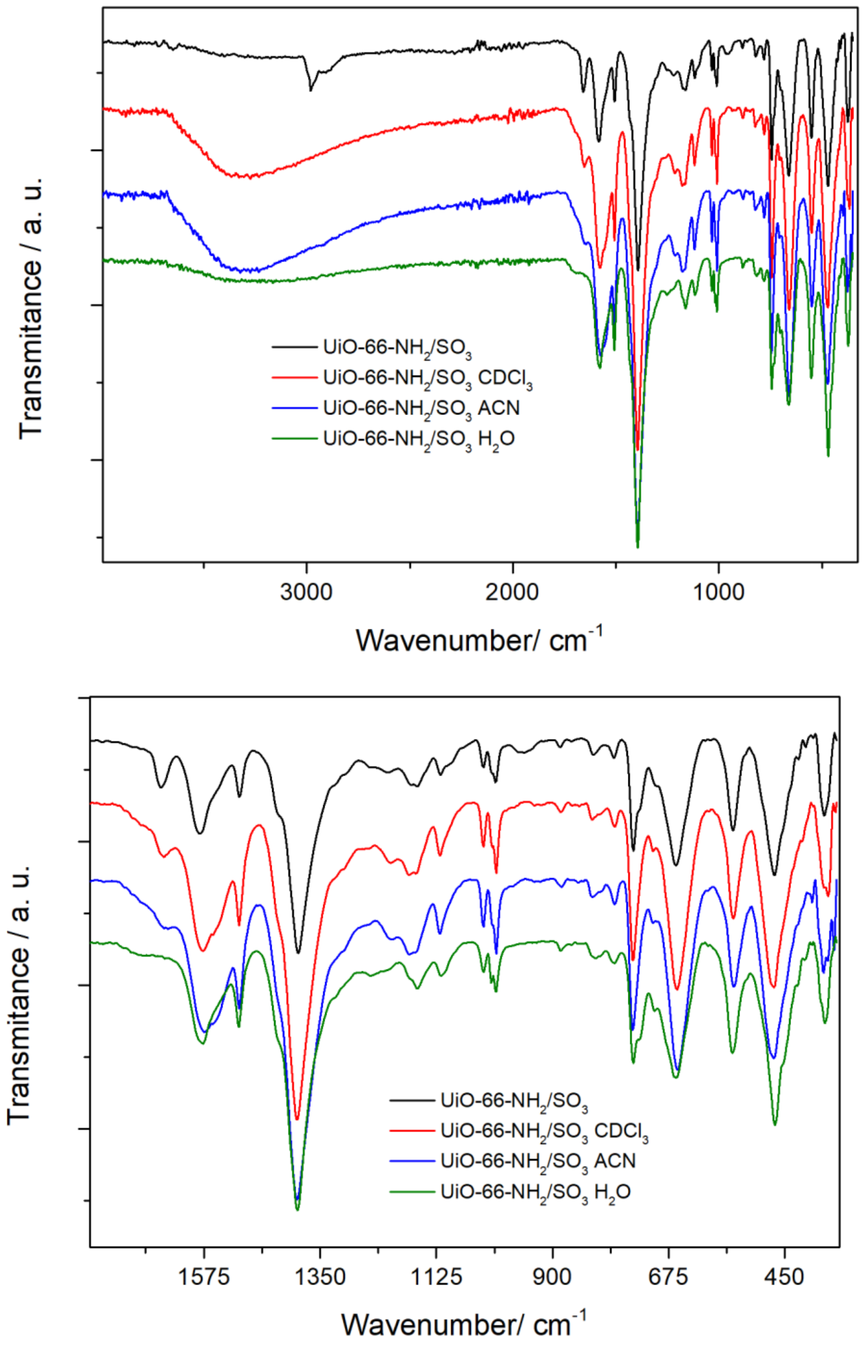

Figure S36: FT-IR profiles of UiO-66-NH_2/SO_3 before and after stirring in different solvents for 24h.

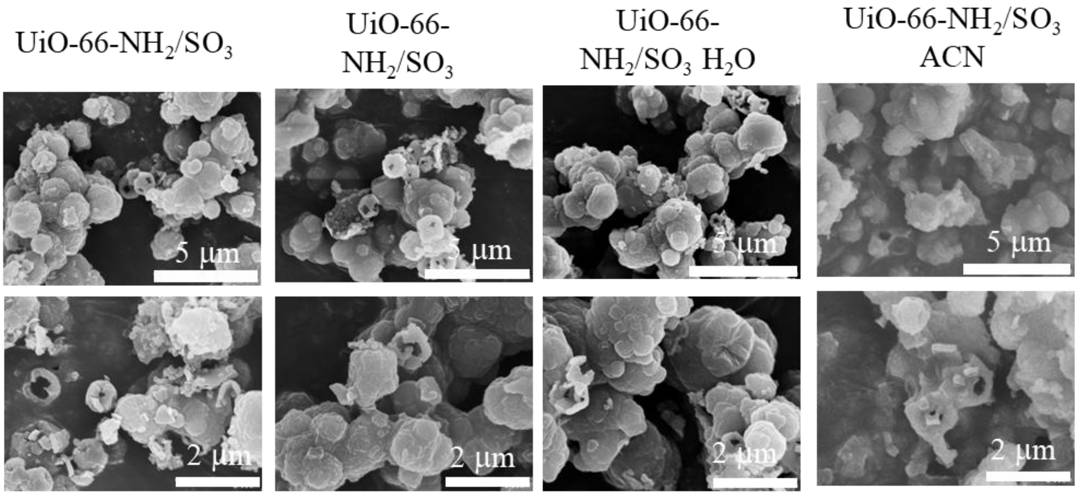

Figure S37: SEM images of UiO-66-NH$_2$/SO$_3$ before and after stirring in different solvents for 24h.

S.3.8 Solid-state UV-Vis

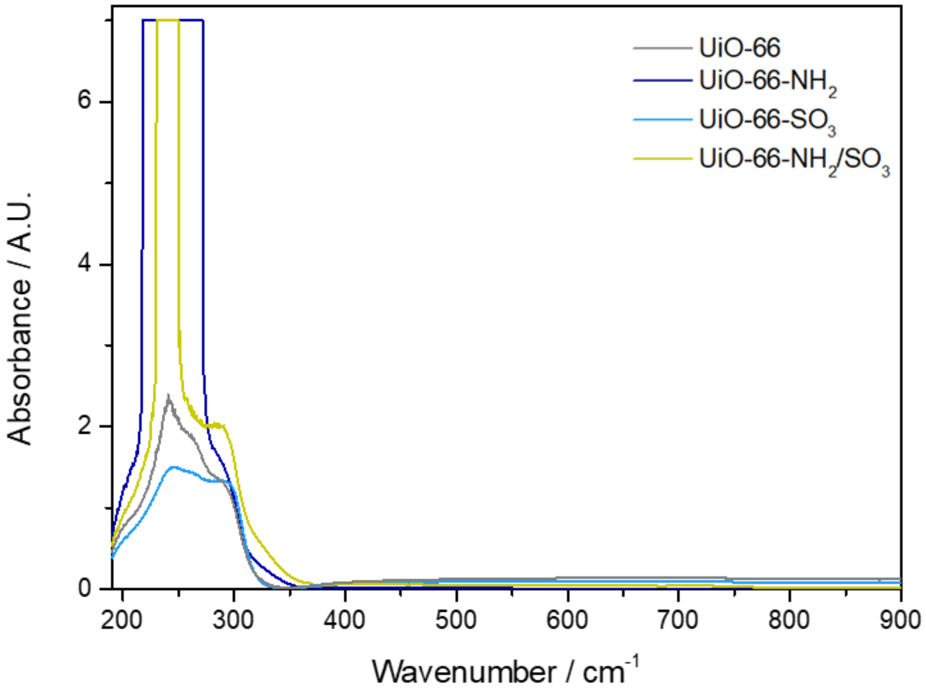

Figure S38: Solid-state UV-Vis spectra of the samples.

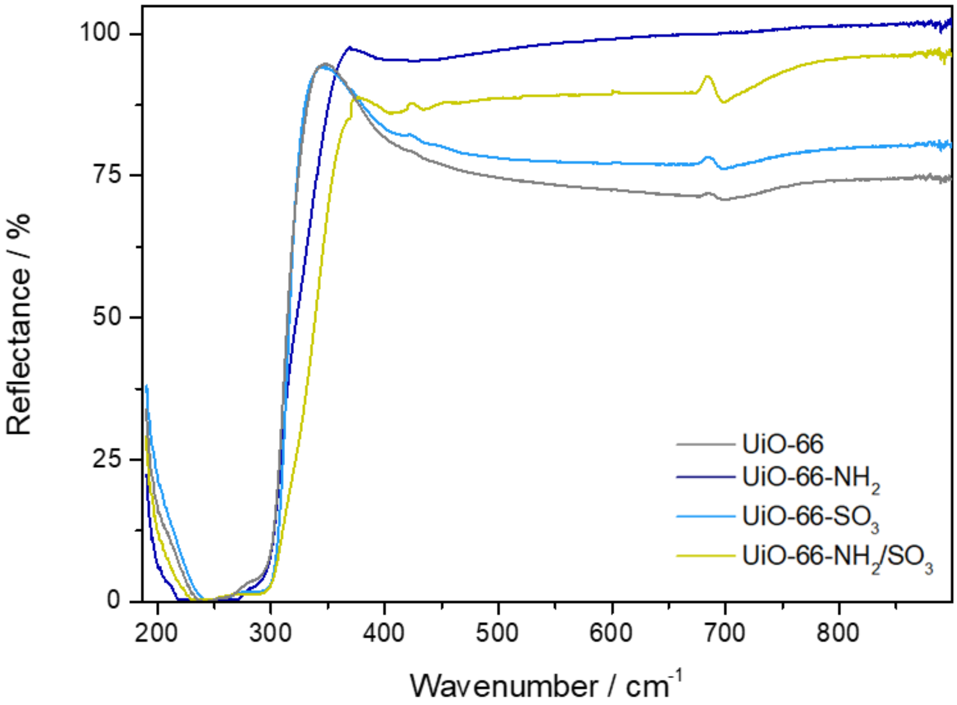

Figure S39: Diffuse reflectance UV-Vis spectra of the samples.

The Tauc plots were constructed by plotting $[(F(R)h\nu)]^{1/,2}$ where F(R) is the Kubelka–Munk function, versus the photon energy (eV). The band gap was extracted by linear fitting of the region near the absorption onset (See Figure S25) and extrapolating the line to intercept the energy axis.

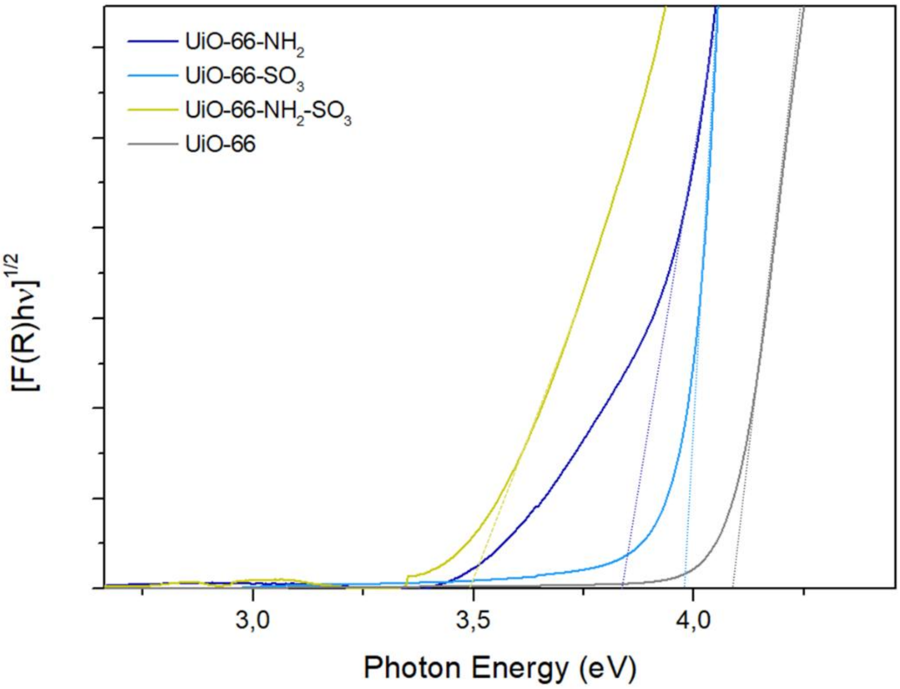

Figure S40: Amplifications of tauc plot of the samples.

Table S7: Estimated optical band gap extracted from fitting of the tauc plots.

Sample	**Band gap (eV)**
UiO-66	4.08
UiO-66-NH$_2$	3.80
UiO-66-SO$_3$	3.96
UiO-66-NH$_2$/SO$_3$	3.47

S.3.9 Nitrogen Adsorption and Desorption Measurements

Table S8: Tabulated data extracted from N_2 adsorption and desorption measurements of UiO-66 MOFs.

Sample	S_{BET}	S_{MICRO}	S_{EXT}	V_{TOTAL}	V_{MICRO}	V_{MESO}
	(m^2 /g)	(m^2 /g)	(m^2 /g)	(cm^3 /g)	(cm^3 /g)	(cm^3 /g)
UiO-66	1191	1028	163	0.532	0.395	0.137
UiO-66-NH_2	1184	1062	122	0.5	0.404	0.096
UiO-66-SO_3	1296	1159	137	0.546	0.468	0.079
UiO-66-NH_2/SO_3	1167	730	437	0.65	0.32	0.33

S_{BET} corresponds to Brunauer–Emmett–Teller surface area. S_{micro} to micropore surface area. S_{ext} to the external surface area. V_{micro} to micropore volume. V_{meso} to mesopore volume and V_{total} to total pore volume.

V_{micro} was calculated using the *t*-plot model with the Harkins and Jura thickness curve based on the BET surface areas. V_{total} was calculated from the cumulative pore size distributions at $P/P_0 = 0.9$, before the inter-particle space and $V_{meso} = V_{total} - V_{micro}$. The pore size distributions were calculated applying the model that provided the lowest fitting error, cylindrical pillared clay.

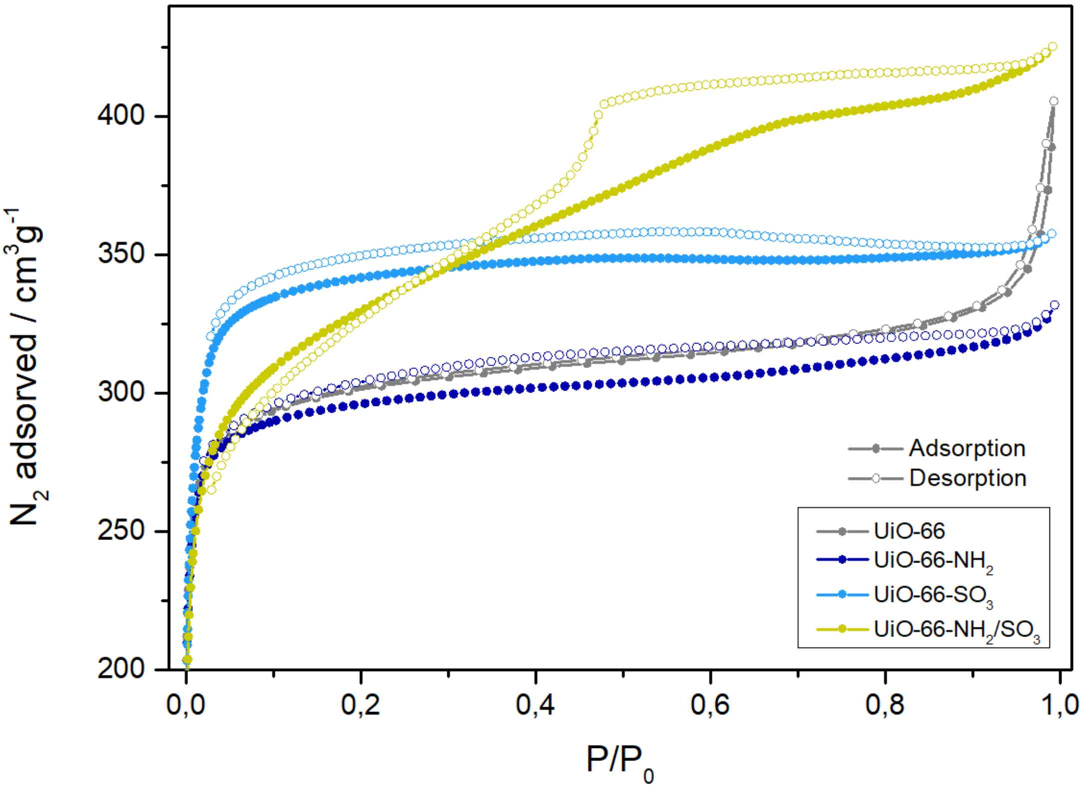

Figure S41: N_2 adsorption and desorption isotherms of the MOFs.

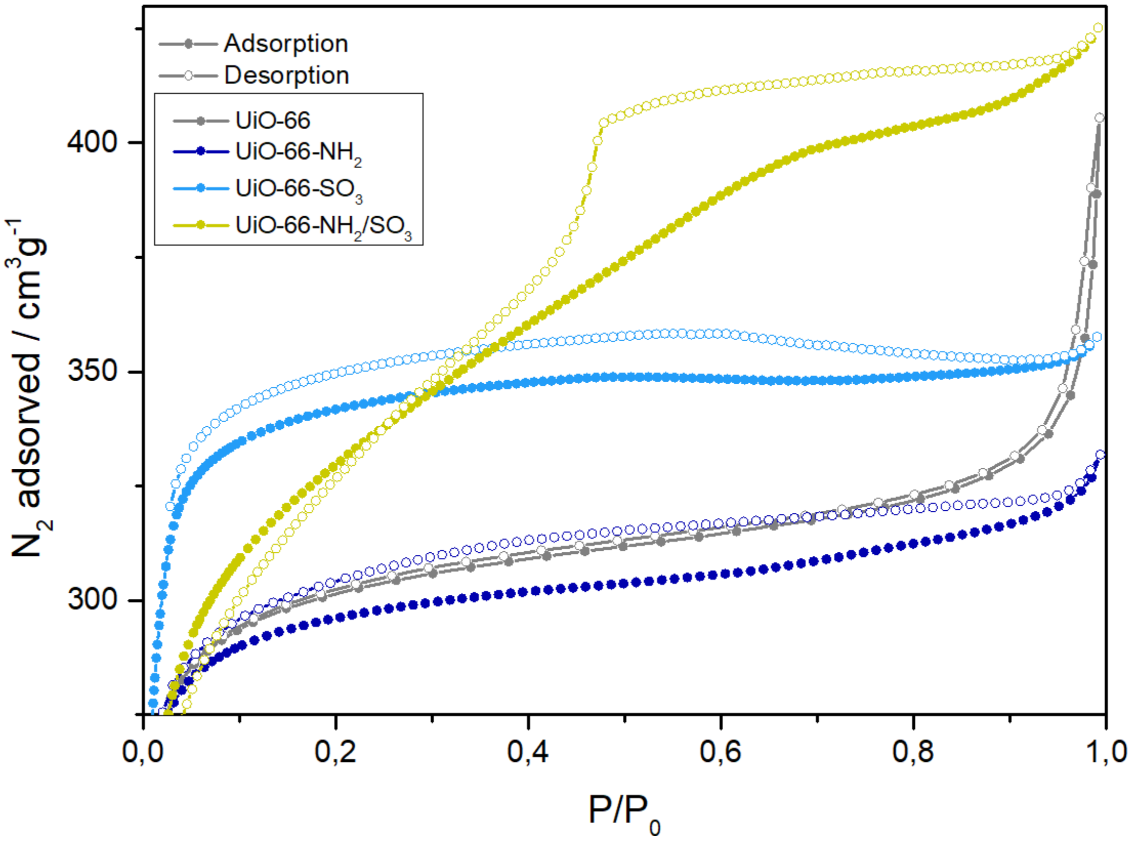

Figure S42: Amplification of the N_2 adsorption and desorption isotherms of the MOFs.

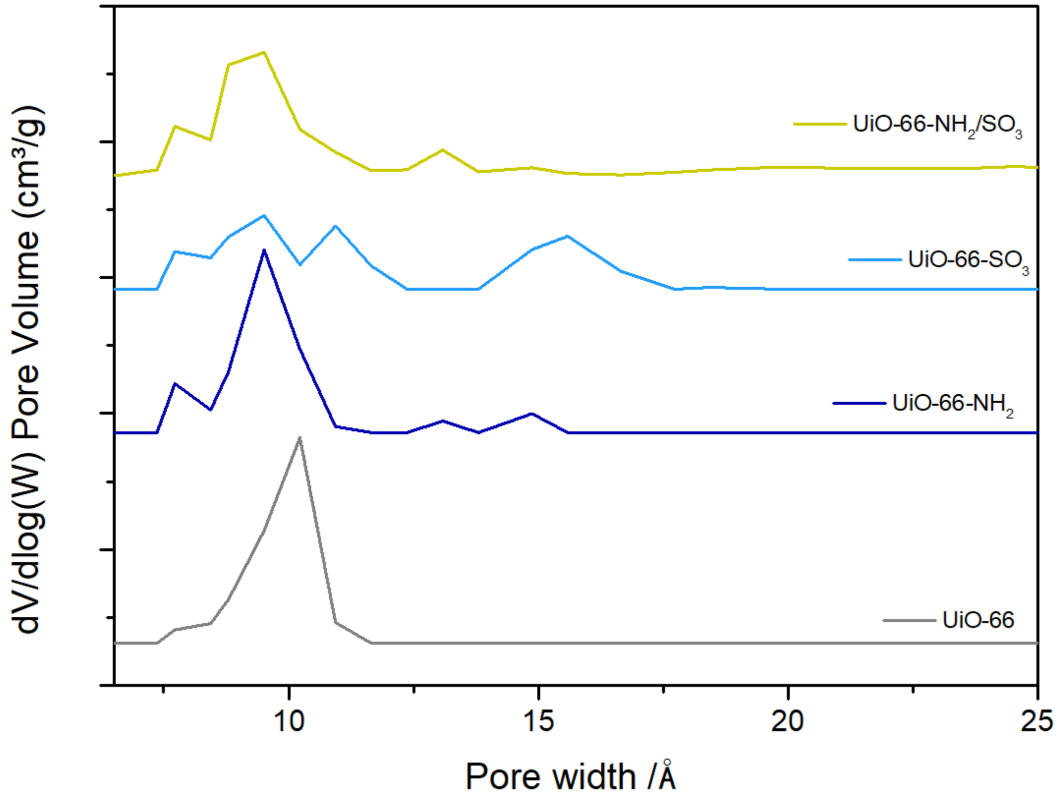

Figure S43: Amplifications of pore size distributions of the MOFs.

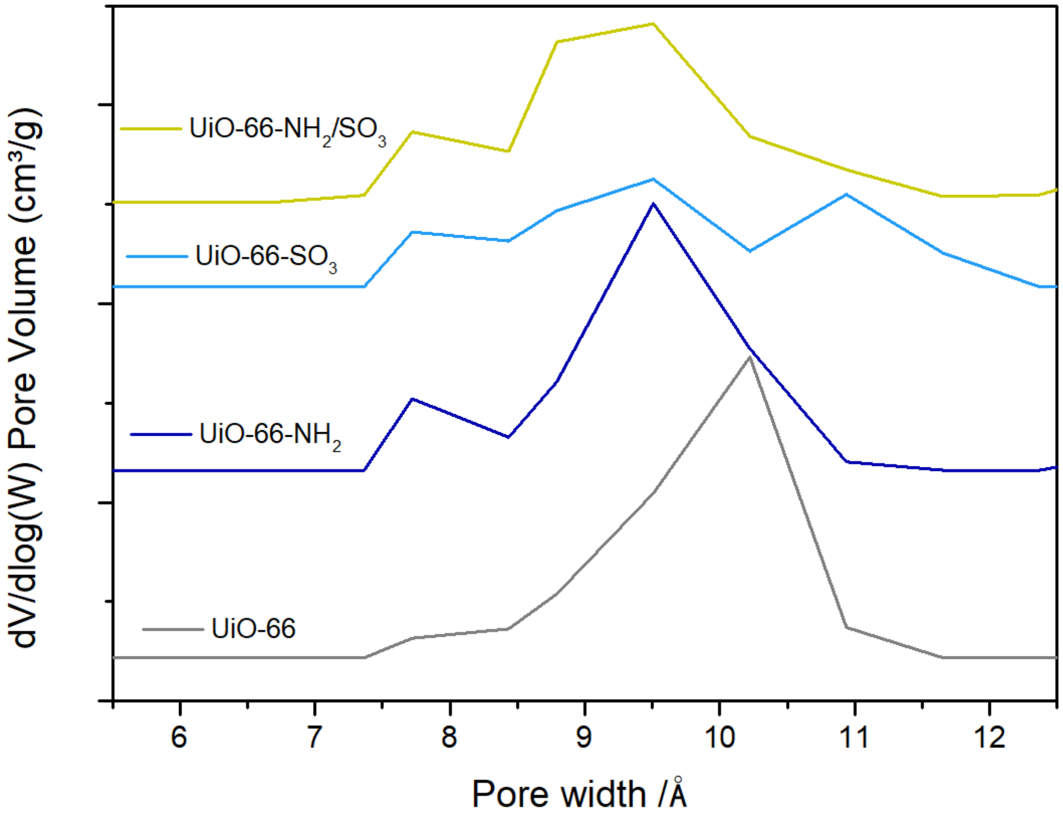

Figure S44: Amplifications of pore size distributions of the MOFs.

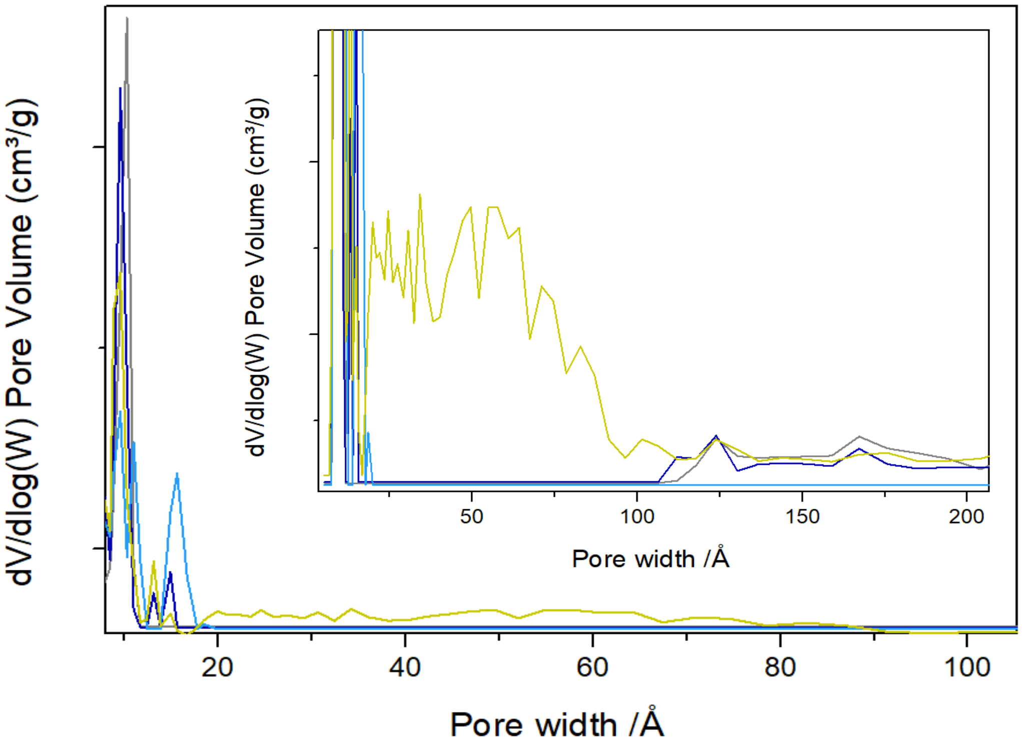

Figure S45: Comparison of pore size distributions of the MOFs.

S.4. Time-resolved synchrotron small-angle X-ray scattering (SAXS)

Time-resolved SAXS patterns were collected at ALBA Synchrotron beamline (NCD-SWEET).

Experiments were performed at a photon energy of 12.4 KeV covering a q-range from 0.08 to 6.8 nm^{-1}, where q is the scattering vector, q = 4π sin(θ)/λ, θ the Bragg angle and λ the photon wavelength, using a pixel single photon counting detector (Pilatus 1M 3s) at a sample-to-detector distance of 2.172 meters. The q-scale was calibrated by means of the standard Silver Behenate, AgBh.

We monitored the self-assembly of UiO-66 materials upon mixing prepared solutions with identical concentration to the ex-situ materials ($ZrCl_4$ dissolved in DMF and linker with modulator dissolved in AcOH/DMF with 0.07 volume ratio). The solutions were mixed and 0.1 mL of the mixture was placed in a 1.5 mm diameter capillary that was sealed 5 minutes prior to the start of the reaction, which was heated from 25 °C to 120ºC with a heating ramp of 4ºC/min.

Images were acquired with a time resolution of 30 s over a time course of 3 hours with an exposure time of 5 seconds. The resulting two-dimensional images were azimuthally integrated to obtain 1D intensity profile patterns that plot intensity versus scattering vector q. That intensity has been normalised from intensity fluctuations of the incoming X-ray beam and variations of the sample transmission. The scattering plot of a capillary filled with DMF was collected and subtracted as background from the data.

Igor 9 software, WaveMetrics, Inc. and Irena[5] packages were used for data analysis.

The Bragg reflection bands were fitted to a Gaussian profile to extract the intensity.
The integrated parameters were computed in the q range between 0.1 nm^{-1} and 2.7 nm^{-1}.[6]

The equation used for the calculation of the Porod Invariant (Q)was:

$$Q = \int_{qmin}^{qmax} I(q)\mathrm{q}^2 dq$$

The integrated intensity was calculated using the following formula:

$$I\ int = \int_{qmin}^{qmax} I(q) dq$$

To estimate the correlation length (ξ) we applied the empirical approximation by combining the Invariant and integrated intensity with the Ornstein-Zernike function.[7,8]

Ornstein-Zernike function $I\ (q) = \frac{\mathrm{I(0)}}{1+(\xi \mathrm{q})^2}$

$$Correlation\ legnth\ (\xi) = \frac{\pi *\ I\ int}{\mathrm{Q}}$$

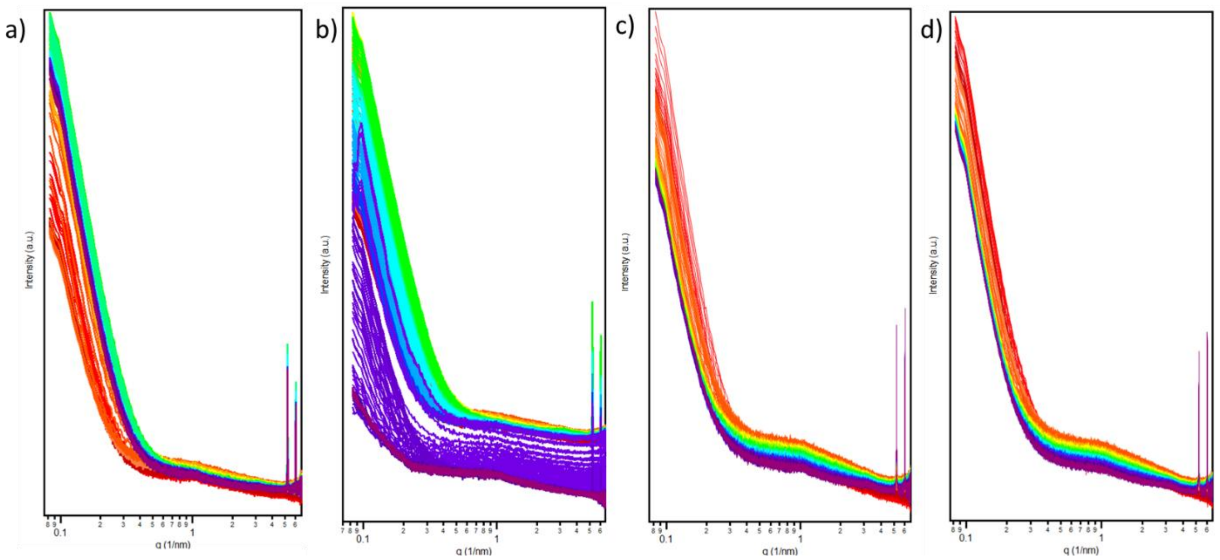

Figure S46: Time evolution of raw SAXS profiles of a) UiO-66, b) UiO-66-NH_2, c) UiO-66-SO_3 and d) UiO-66-NH_2/SO_3.

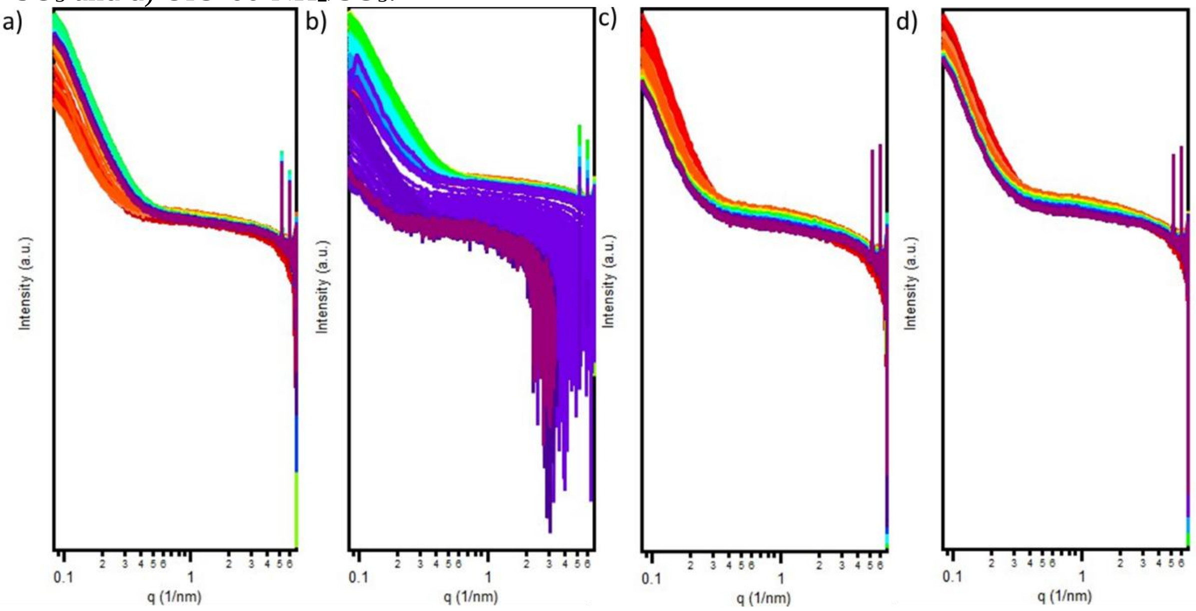

Figure S47: Time evolution of background subtracted SAXS profiles of a) UiO-66, b) UiO-66-NH_2, c) UiO-66-SO_3 and d) UiO-66-NH_2/SO_3.

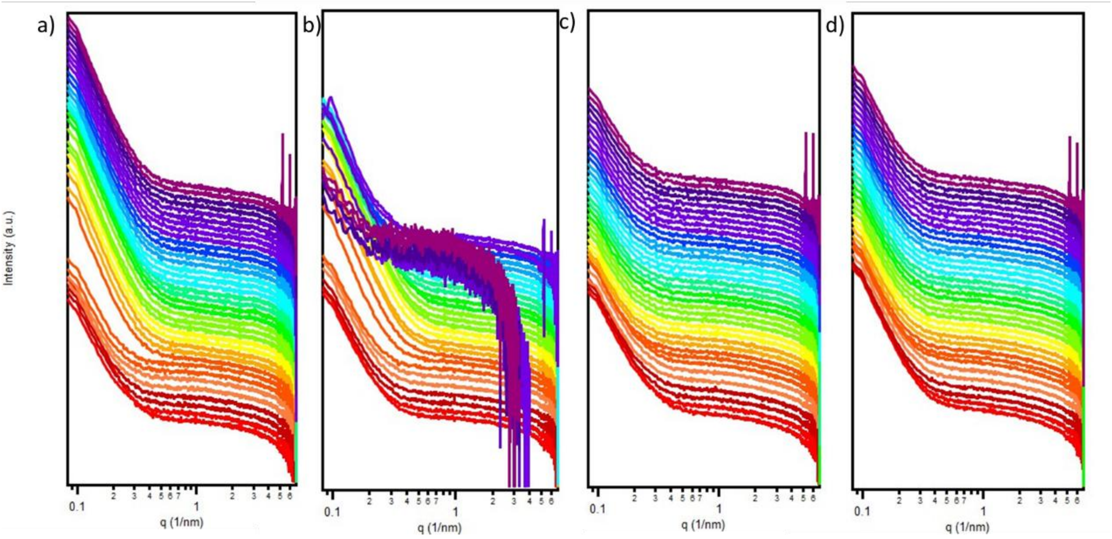

Figure S48: Stacked time evolution of background-subtracted SAXS profiles for every 5 minutes of reaction for a) UiO-66, b) UiO-66-NH_2, c) UiO-66-SO_3 and d) UiO-66-NH_2/SO_3. The same offset and intensity scale are applied to all graphs.

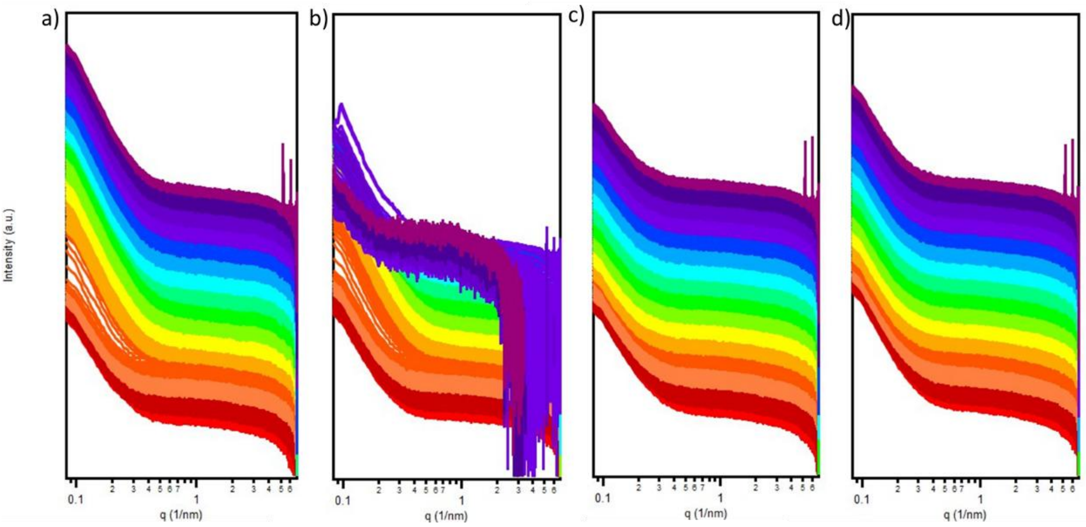

Figure S49: Stacked time evolution of background-subtracted SAXS profiles for every 0.5 minutes of reaction for a) UiO-66, b) UiO-66-NH_2, c) UiO-66-SO_3 and d) UiO-66-NH_2/SO_3. The same offset and intensity scale are applied to all graphs.

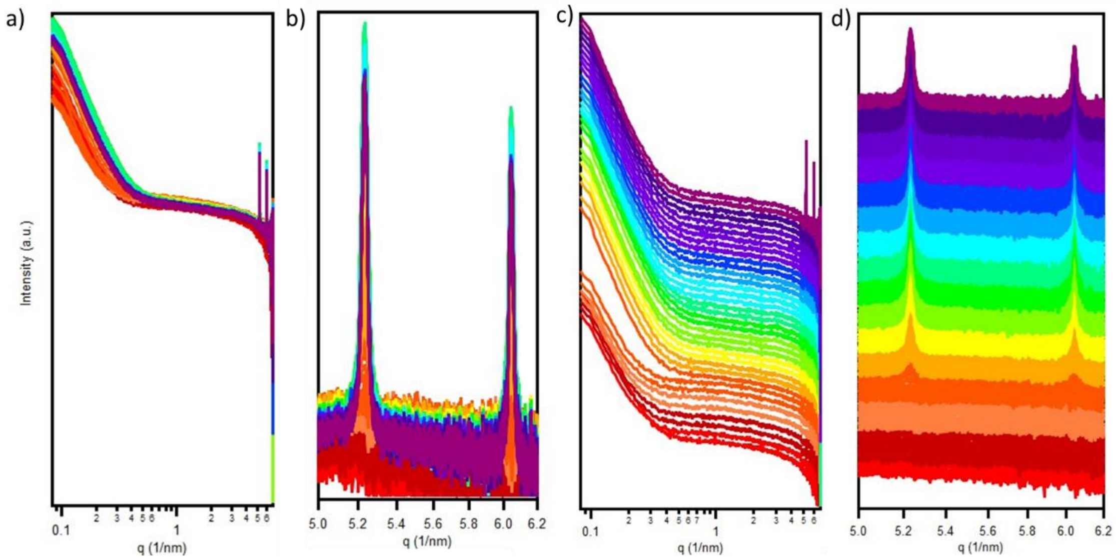

Figure S50: Time evolution of background-subtracted SAXS profiles of UiO-66.

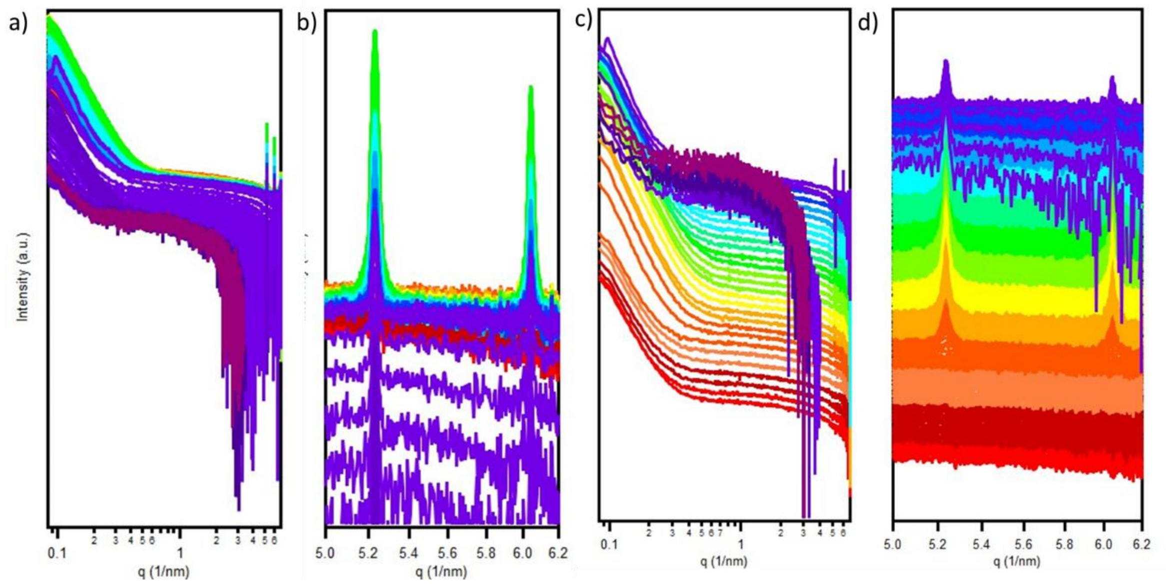

Figure S51: Time evolution of background-subtracted SAXS profiles of UiO-66-NH_2.

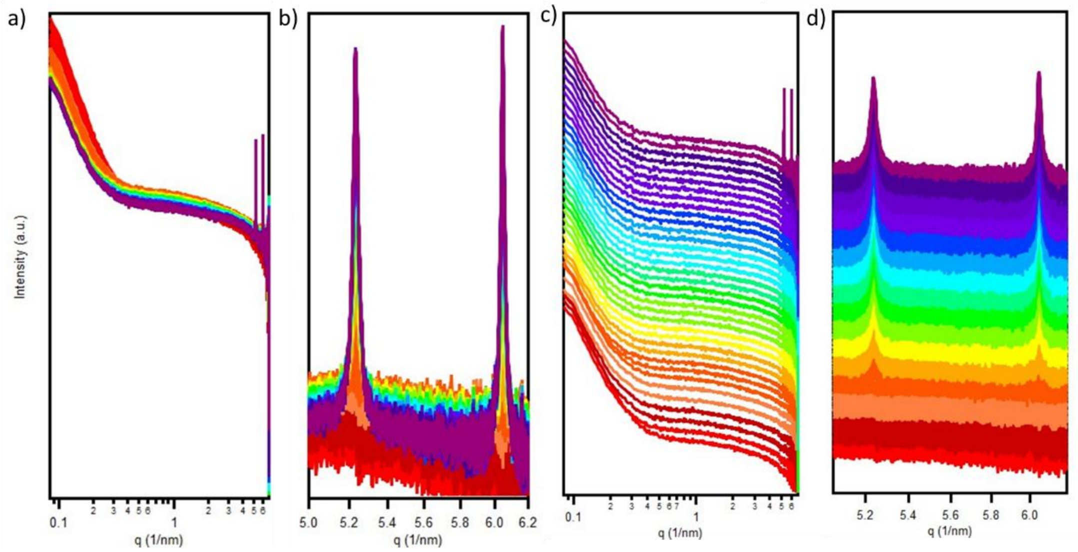

Figure S52: Time evolution of background-subtracted SAXS profiles of UiO-66-SO_3.

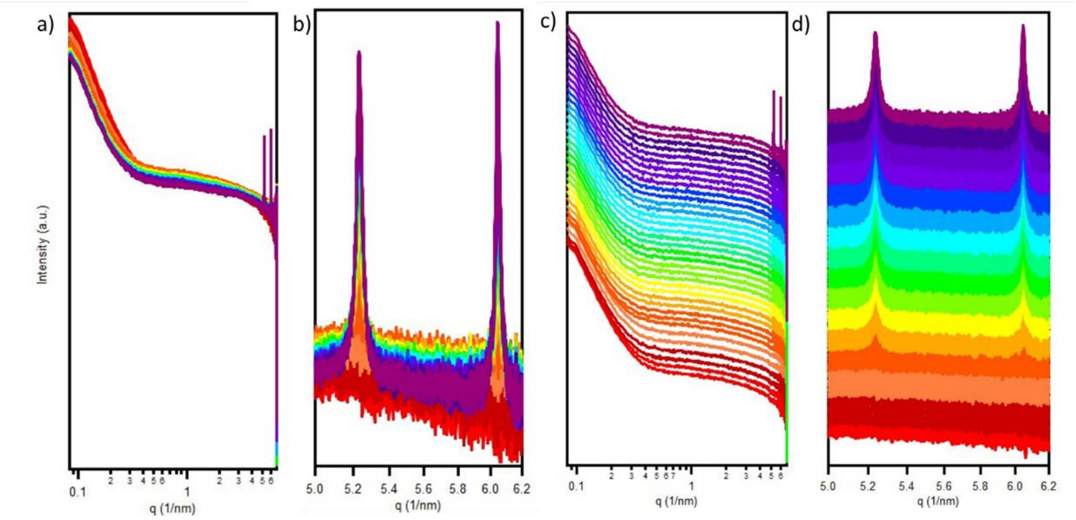

Figure S53: Time evolution of background-subtracted SAXS profiles of UiO-66-NH_2/SO_3.

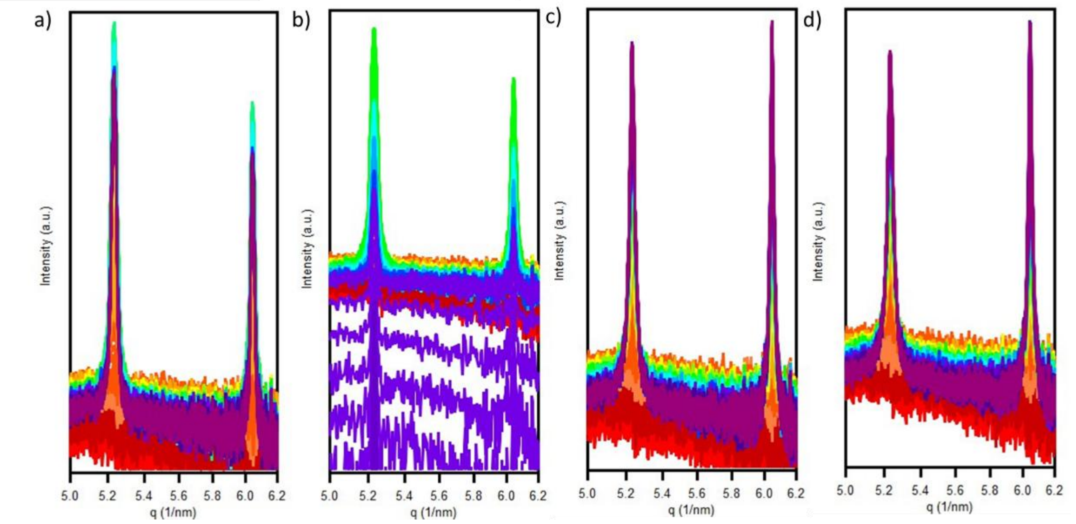

Figure S54: Time evolution Bragg reflection background-subtracted profiles of a) UiO-66, b) UiO-66-NH_2, c) UiO-66-SO_3 and d) UiO-66-NH_2/SO_3.

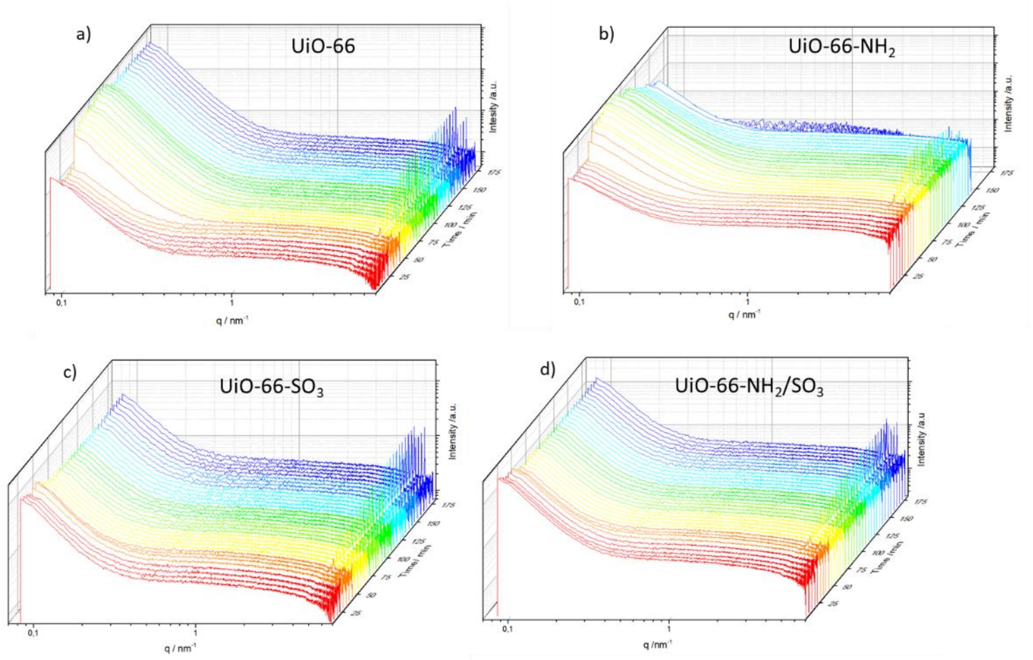

Figure S55: Time evolution of background-subtracted log-log SAXS profiles of a) UiO-66, b) UiO-66-NH$_2$, c) UiO-66-SO$_3$ and d) UiO-66-NH$_2$/SO$_3$. Scattering is provided every 5 minutes.

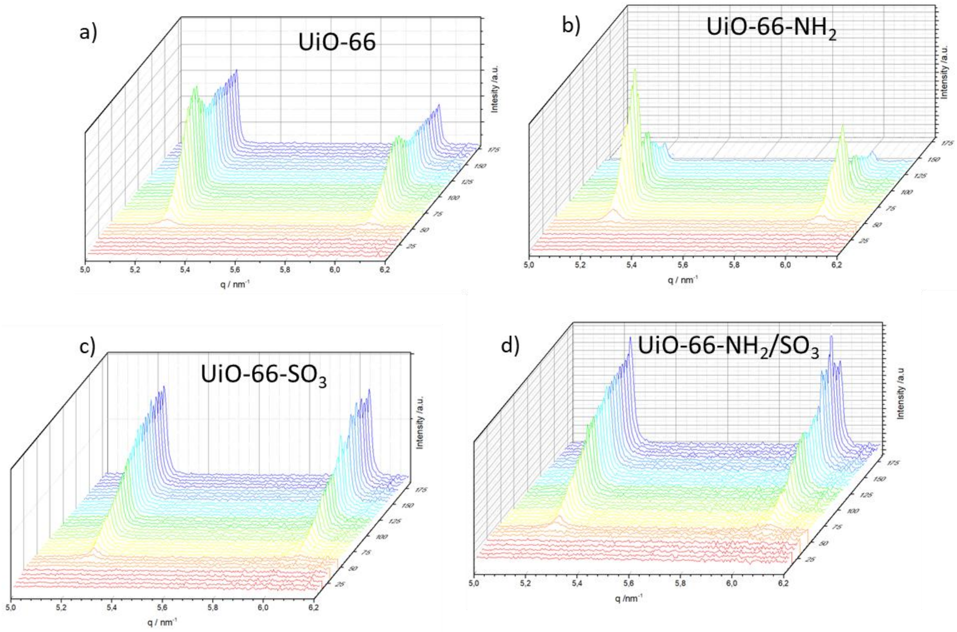

Figure S56: Time evolution Bragg reflection background-subtracted profiles of a) UiO-66, b) UiO-66-NH$_2$, c) UiO-66-SO$_3$ and d) UiO-66-NH$_2$/SO$_3$. Scattering is provided every 5 minutes.

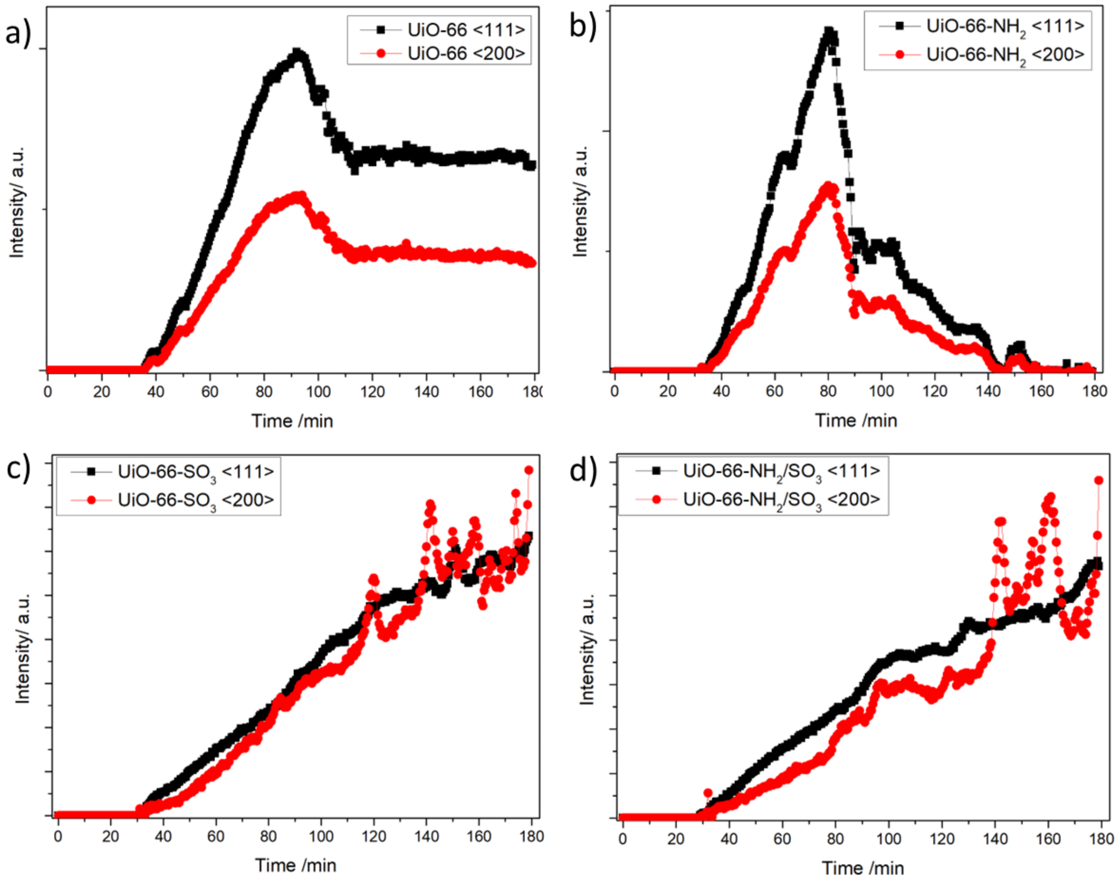

Figure S57: Relative intensity of the Bragg reflection bands.

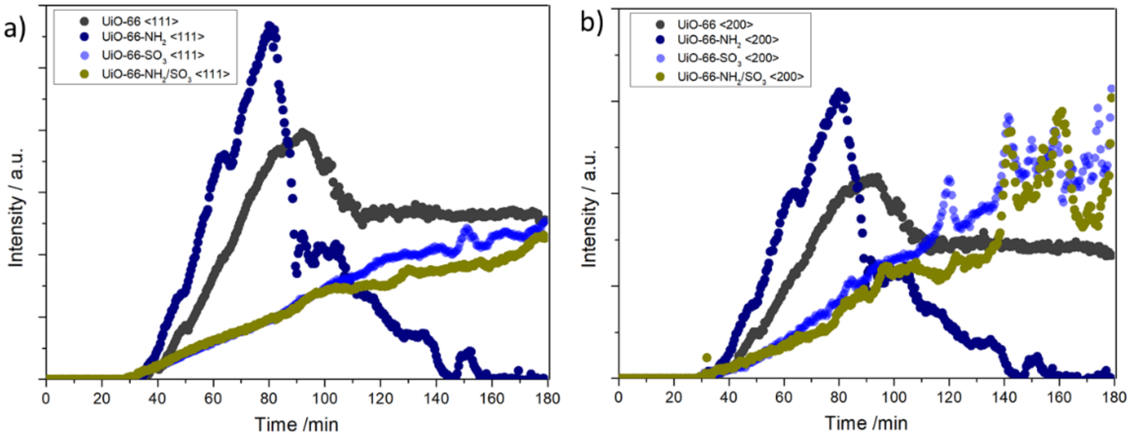

Figure S58: Comparison of the intensity of the Bragg reflection bands.

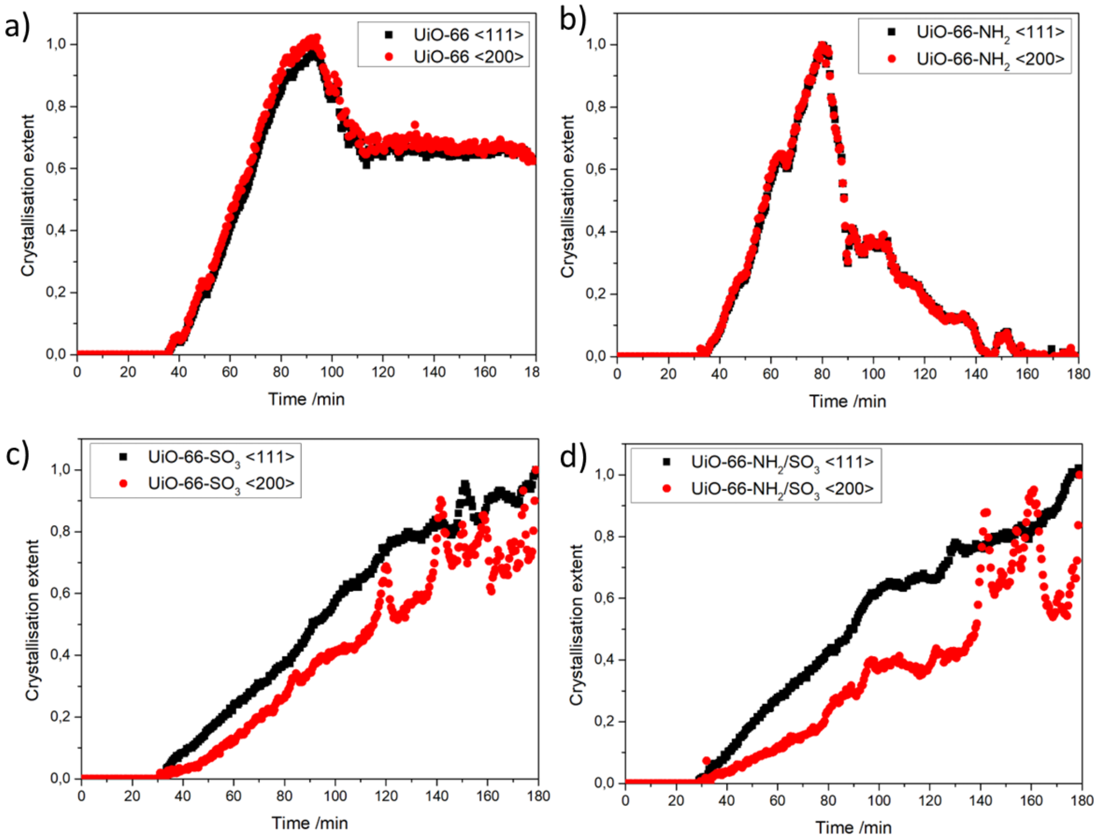

Figure S59: Crystallisation extent extracted from normalizing the intensity of the Bragg reflection bands to the highest intensity recorded for each Bragg reflection.

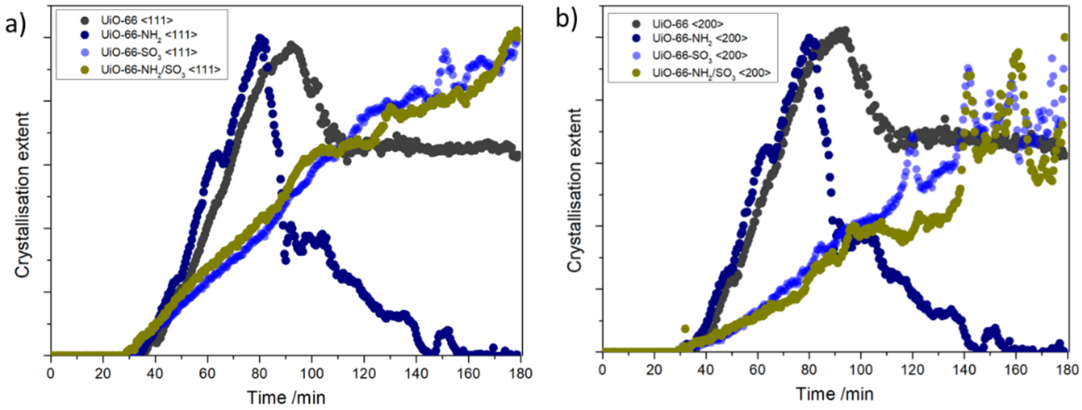

Figure S60: Comparison of the crystallisation extent based on the intensity of the Bragg reflection bands.

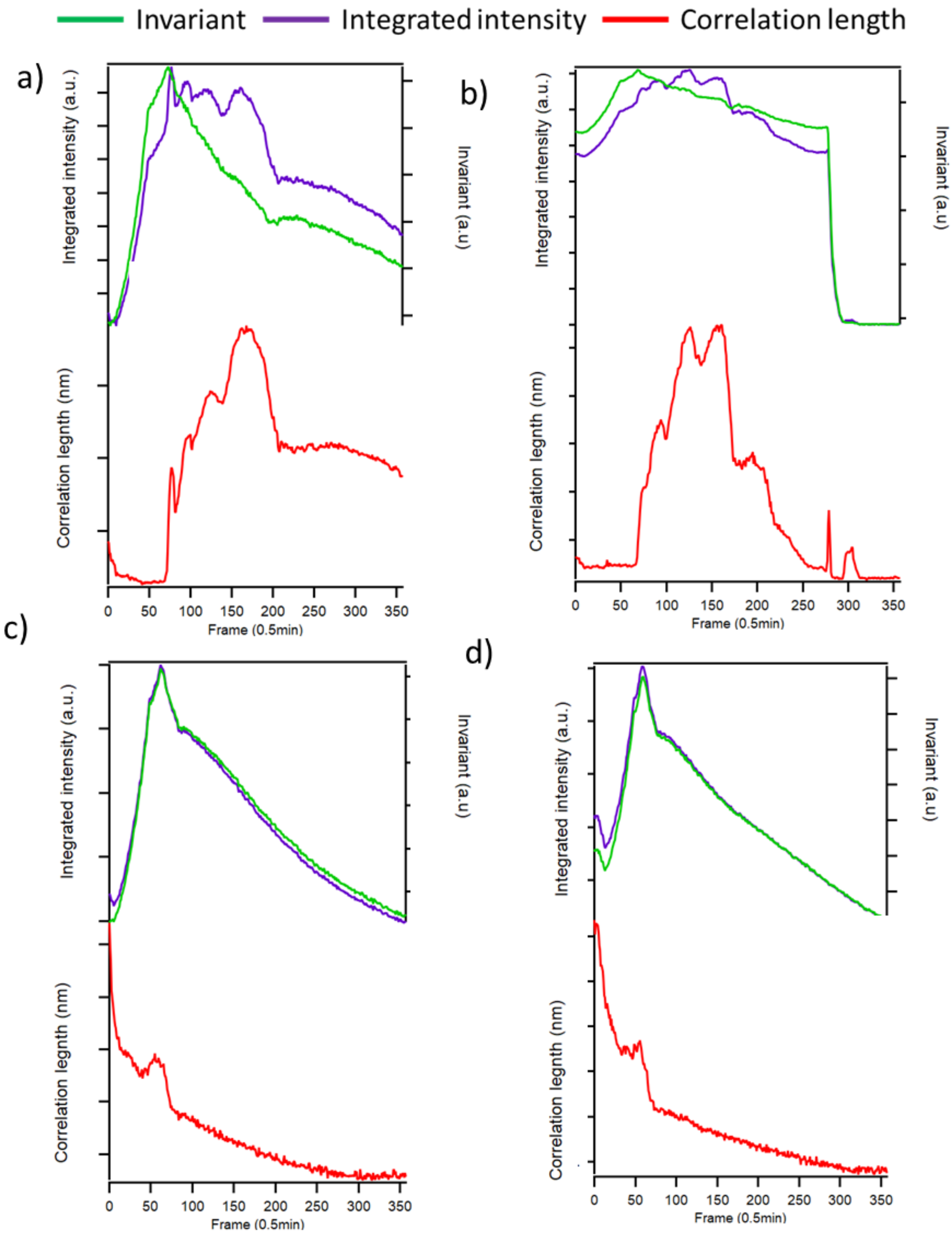

Figure S61: Time evolution of integrated parameters for a) UiO-66, b) UiO-66-NH_2, c) UiO-66-SO_3 and d) UiO-66-NH_2/SO_3.

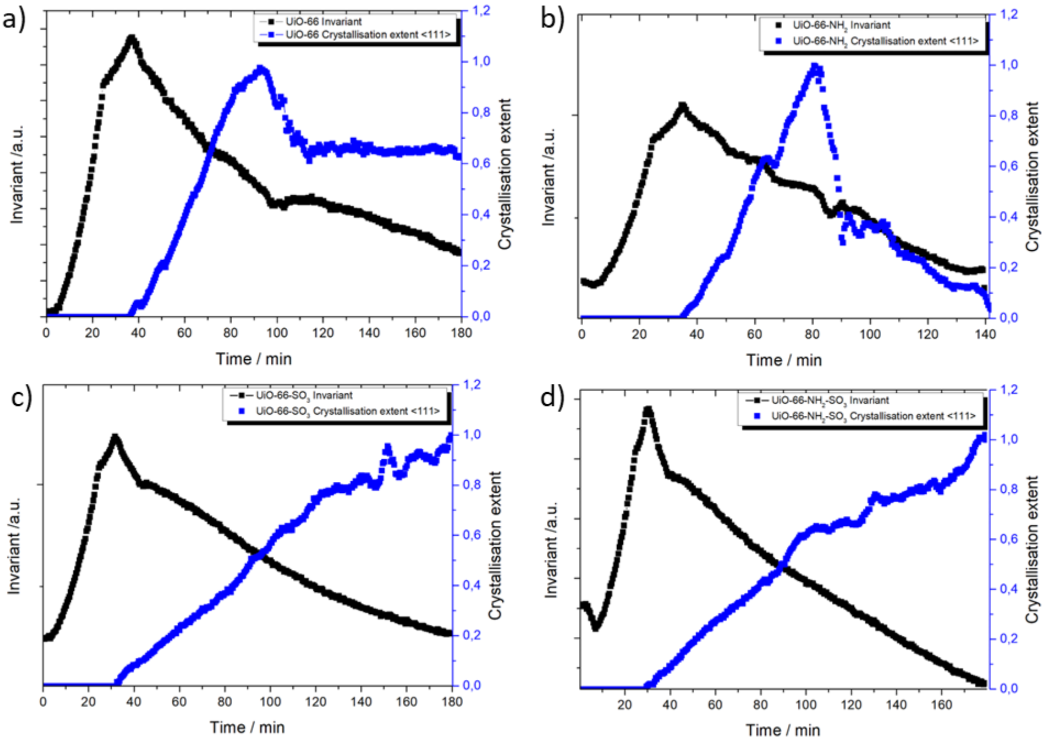

Figure S62: Time evolution of the invariant compared to the crystallisation extent.

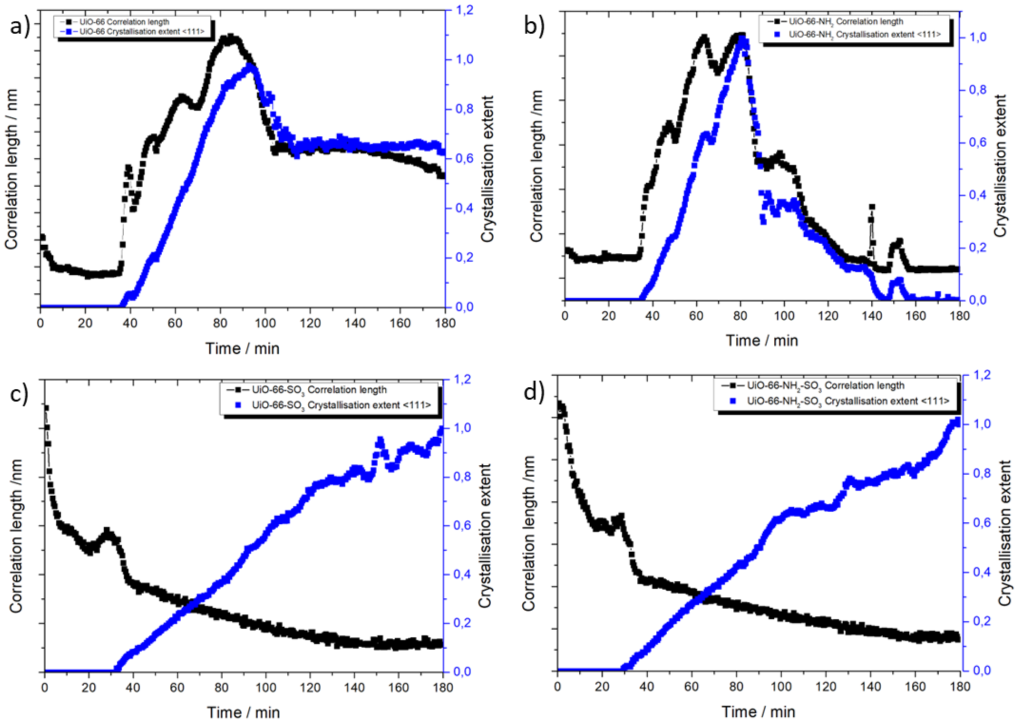

Figure S63: Time evolution of the correlation length compared to the crystallisation extent.

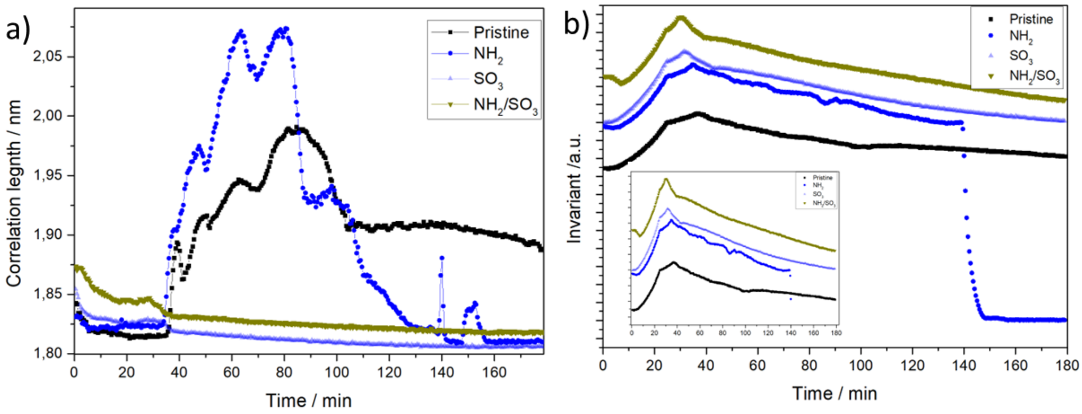

Figure S64: Comparison of the time evolution of the correlation length and invariant.

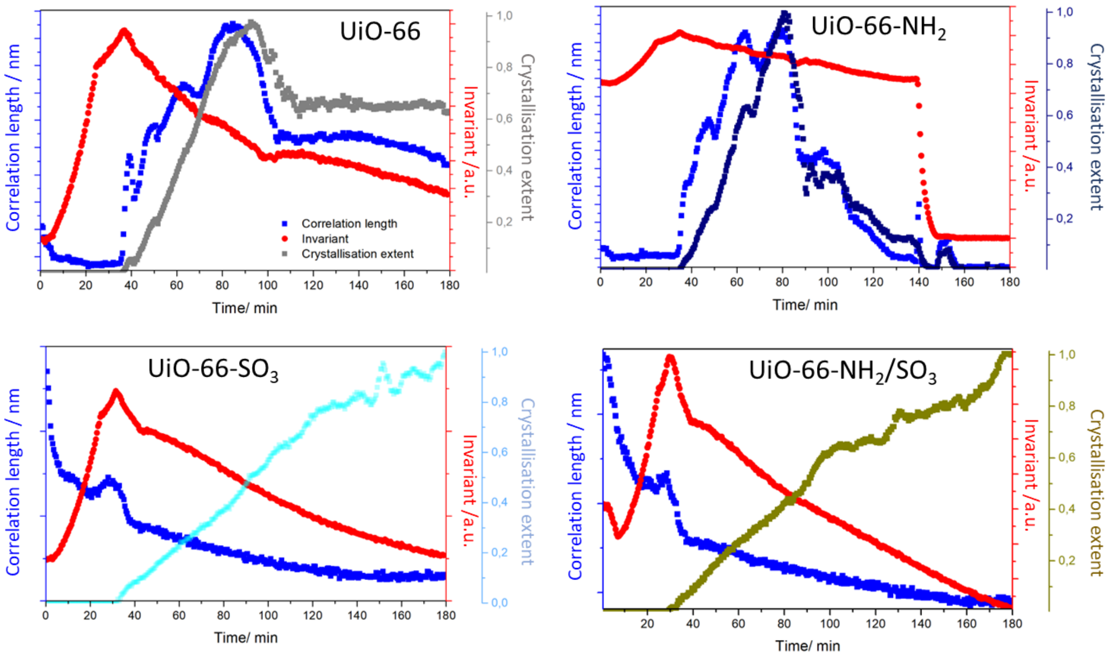

Figure S65: Comparison of the time evolutions of the correlation length, invariant and crystallisation extent.

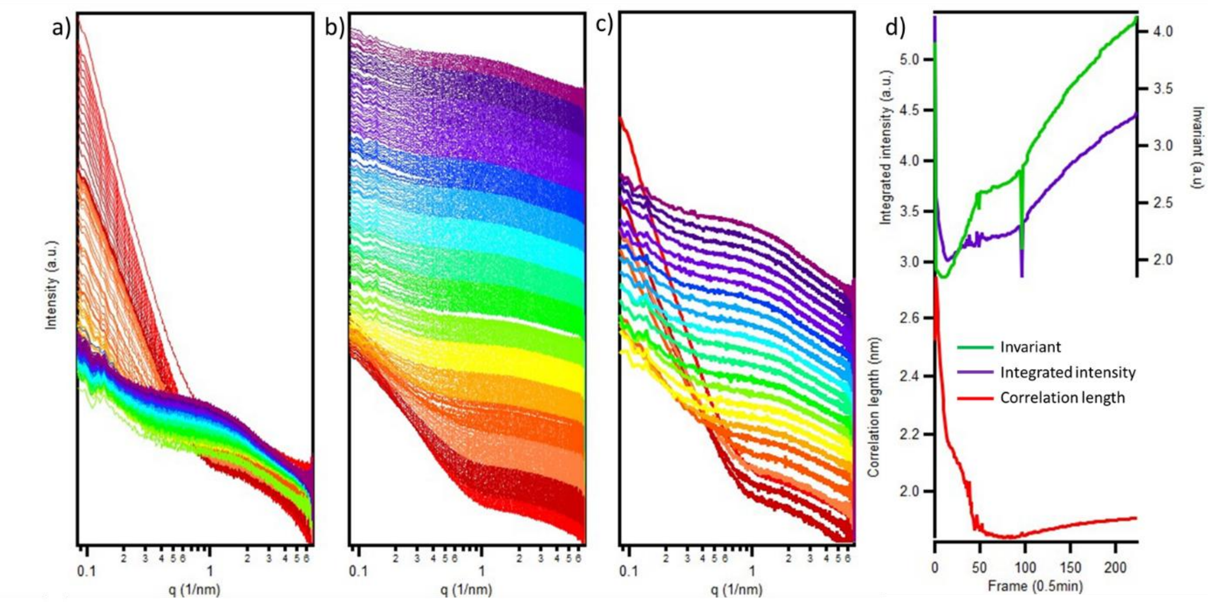

Figure S66: Background-subtracted time evolution SAXS profiles of the control synthesis of Benz-SO$_3$ with Zr in DMF without bdc linker, showing similar features to UiO-66 Benz-SO3 containing synthesis and indicating an initial aggregation of Benz-SO$_3$ with Zr.

S.5. Characterisation of samples synthesised at different reaction times

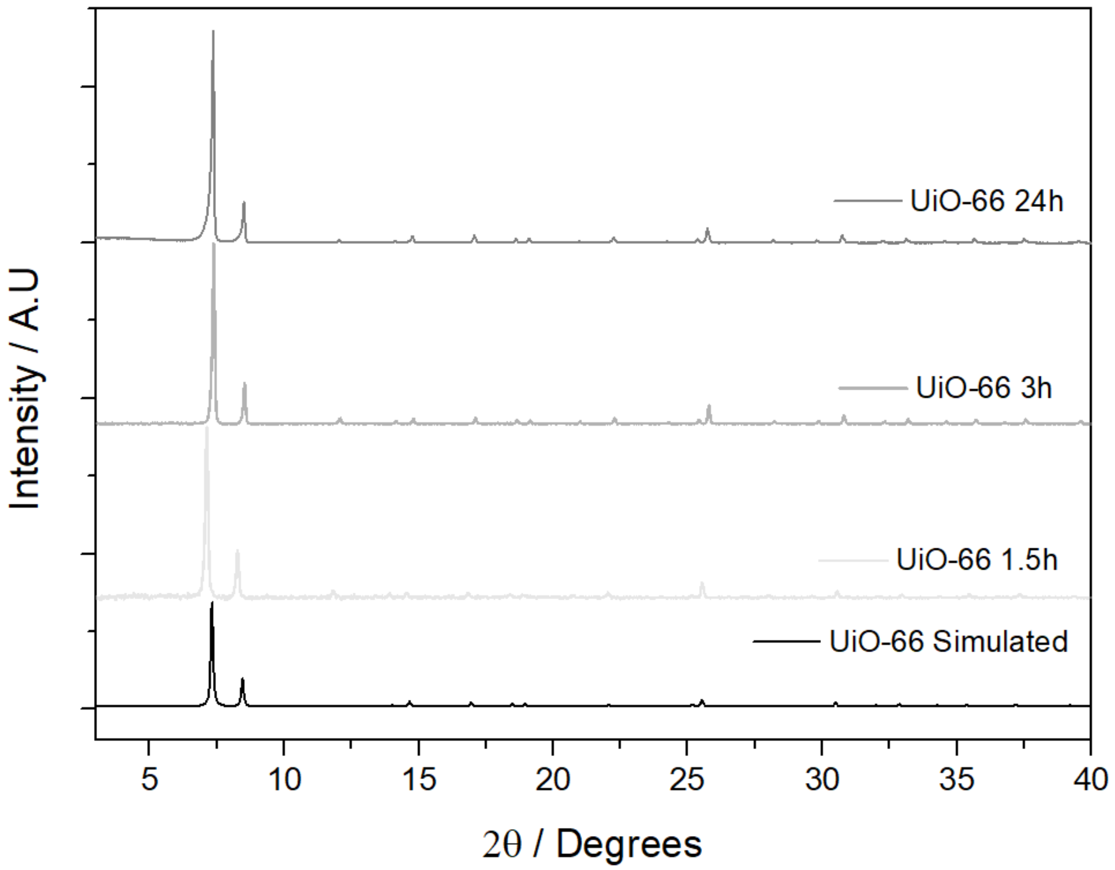

Figure S67: PXRD patterns of UiO-66 PXRD after 1.5 and 3h of reaction time, compared to simulated UiO-66.

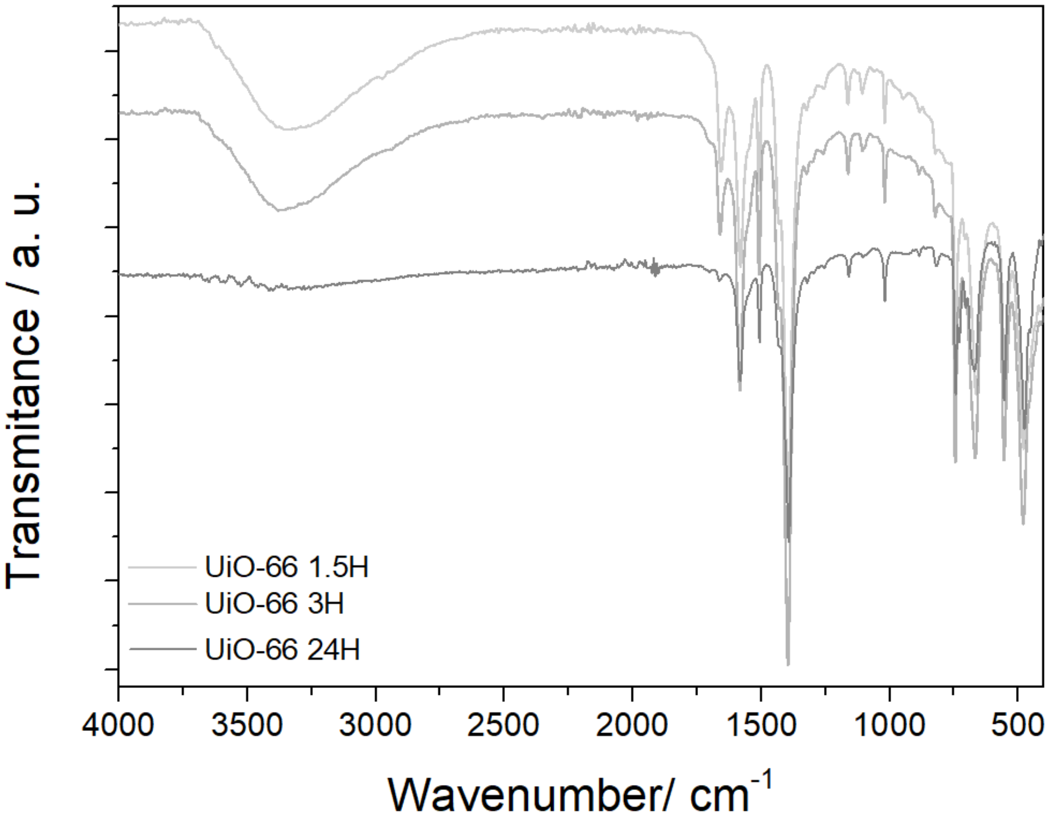

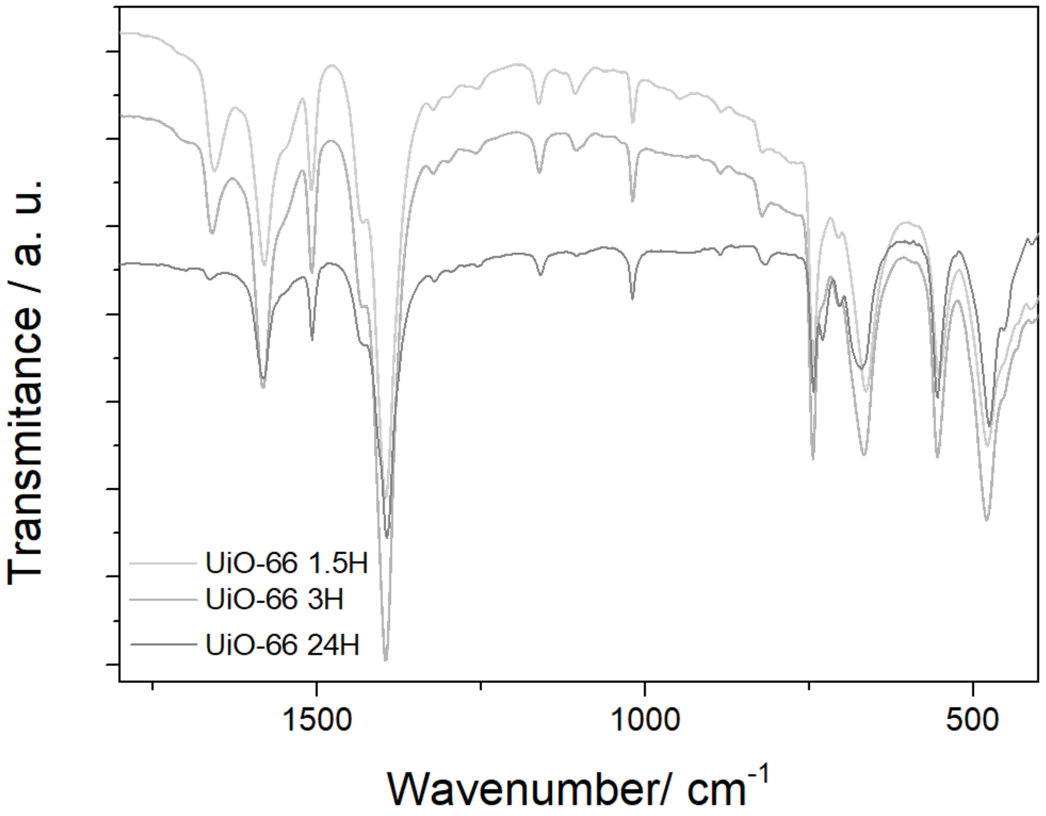

Figure S68: FT-IR profiles of UiO-66 synthesised with different reaction times.

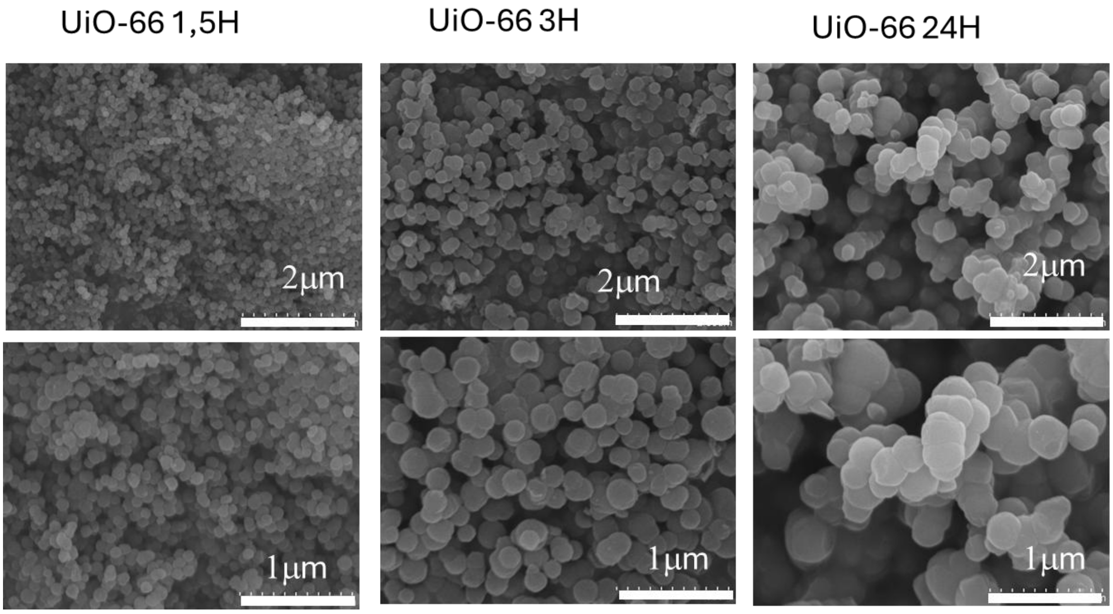

Figure S69: SEM images of UiO-66 after different reaction times.

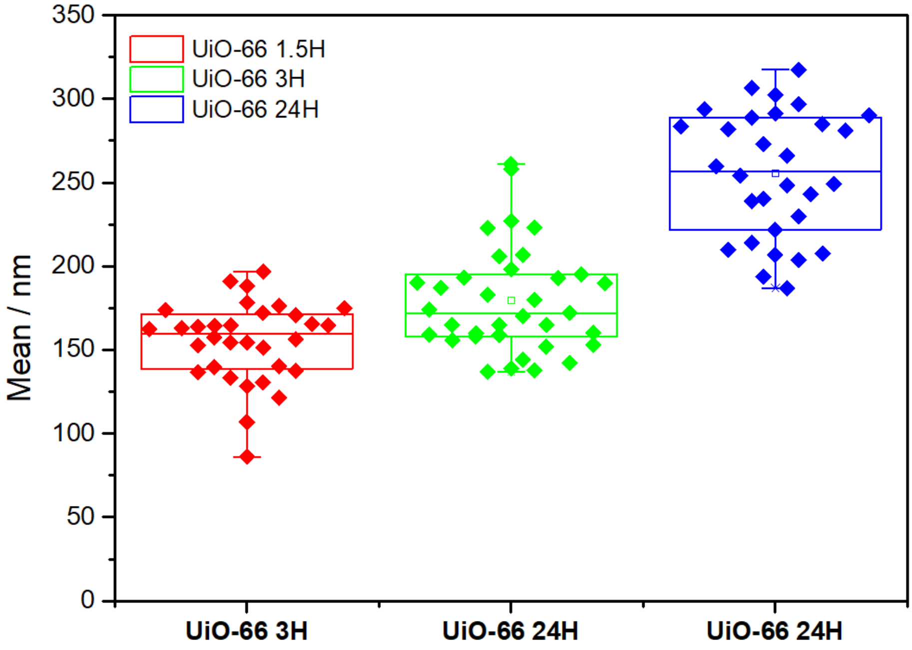

Figure S70: Particle size histogram of UiO-66 after different reaction times. Bin size 10 nm.

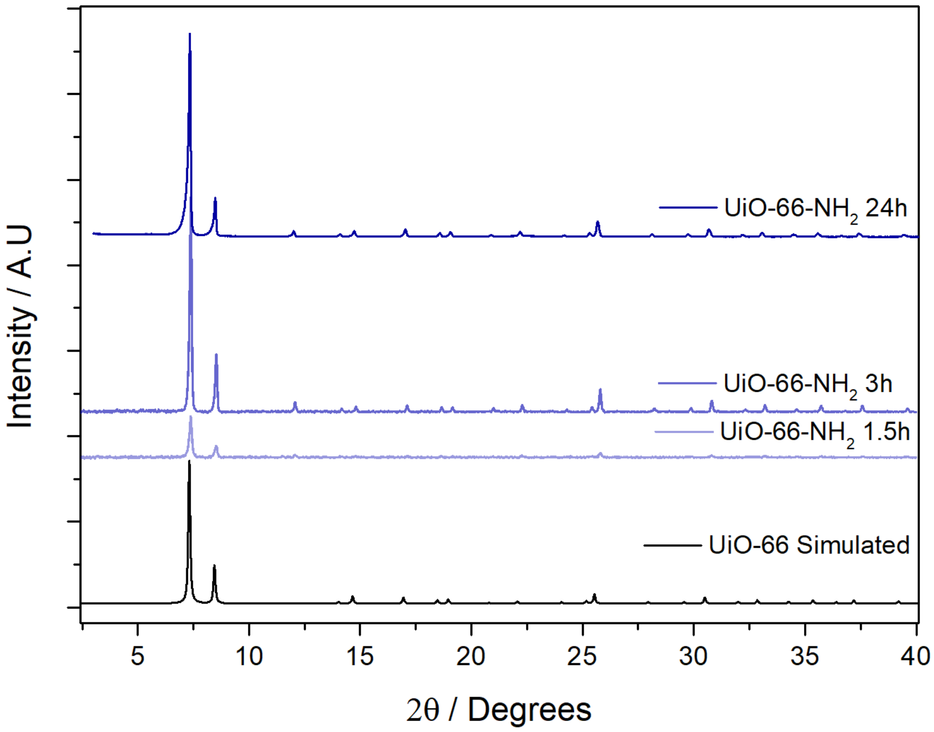

Figure S71: PXRD patterns of UiO-66-NH$_2$ PXRD after 1.5, 3 and 24 hours of reaction time, compared to simulated UiO-66.

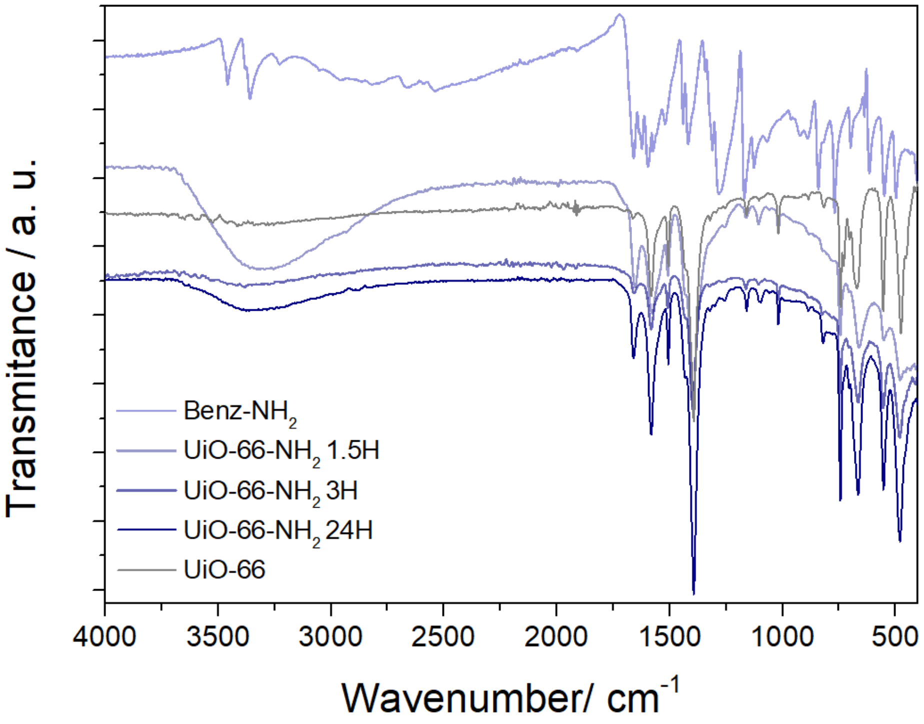

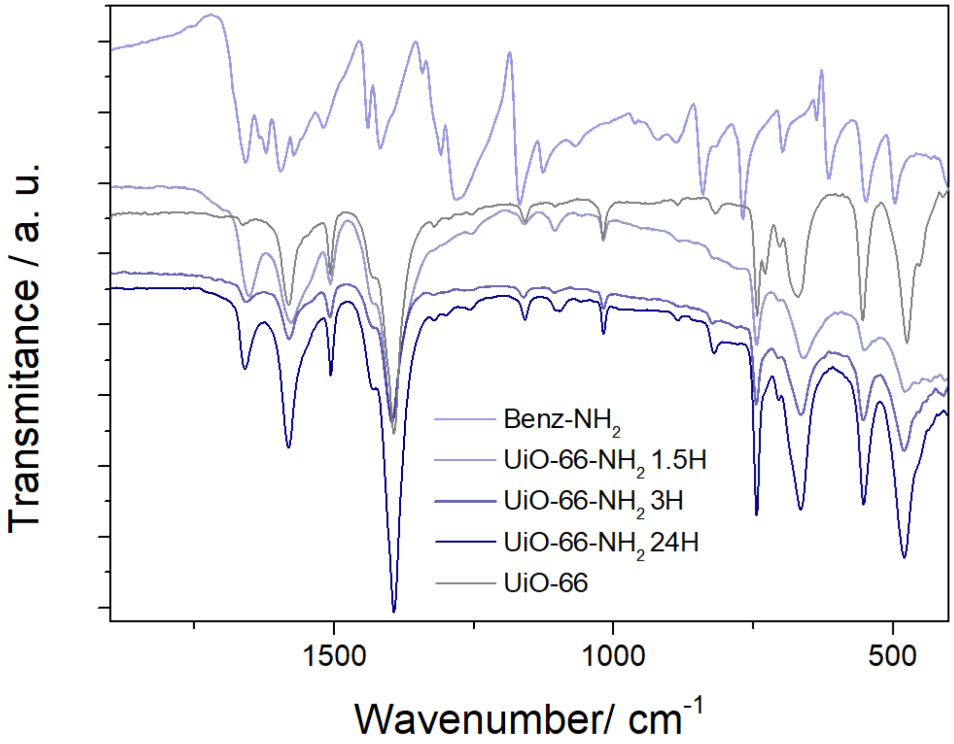

Figure S72: FT-IR profiles of UiO-66-NH_2 synthesised with different reaction times, compared to the free modulator and UiO-66. Given the low quantity of Benz-NH_2 incorporated, its signals, such as the C-N $_{st}$ (ca. 1179 cm^{-1}) and the NH_2 δ (861 cm^{-1} and ca. 798 cm^{-1}) are masked by the MOF's signals.

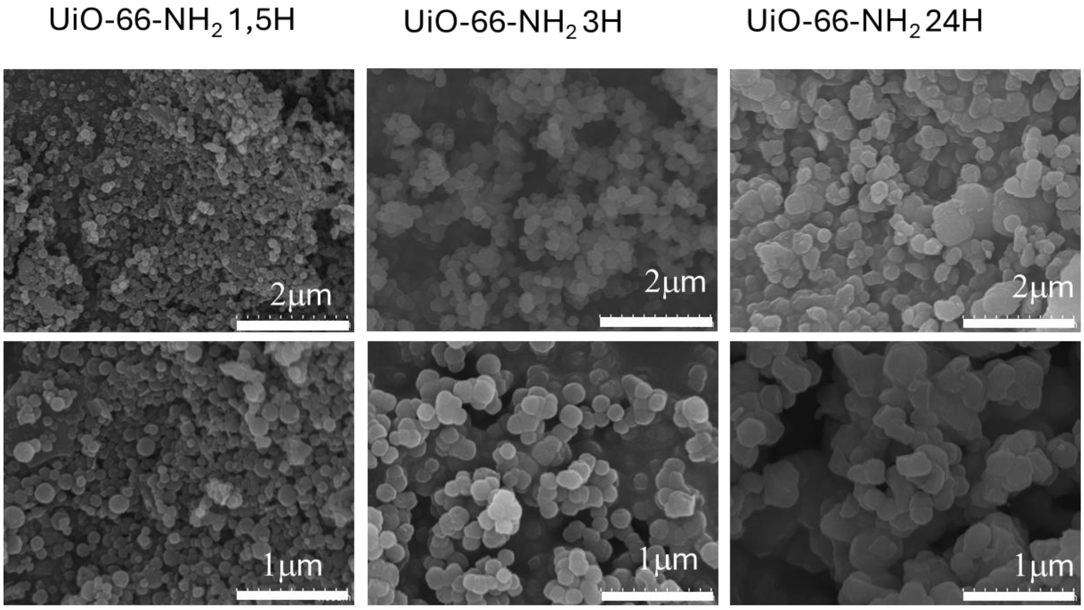

Figure S73: SEM images of UiO-66- NH$_2$ synthesised with different reaction times, 1.5h, 3h and 24h.

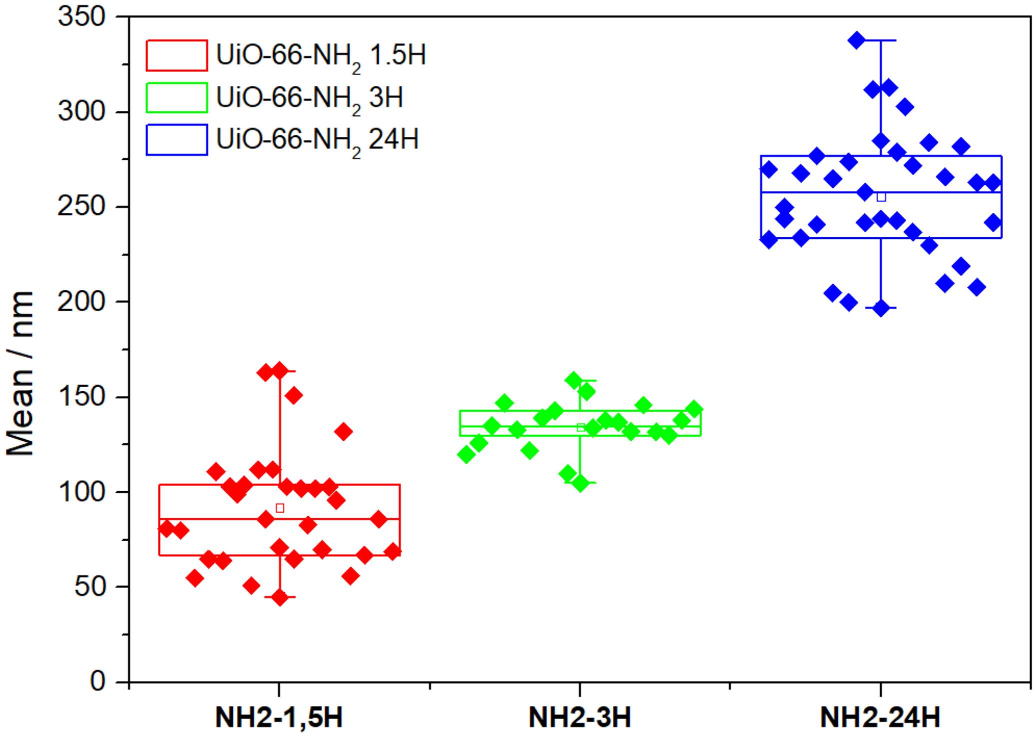

Figure S74: Particle size histogram of UiO-66-NH$_2$ after different reaction times. Bin size 10 nm.

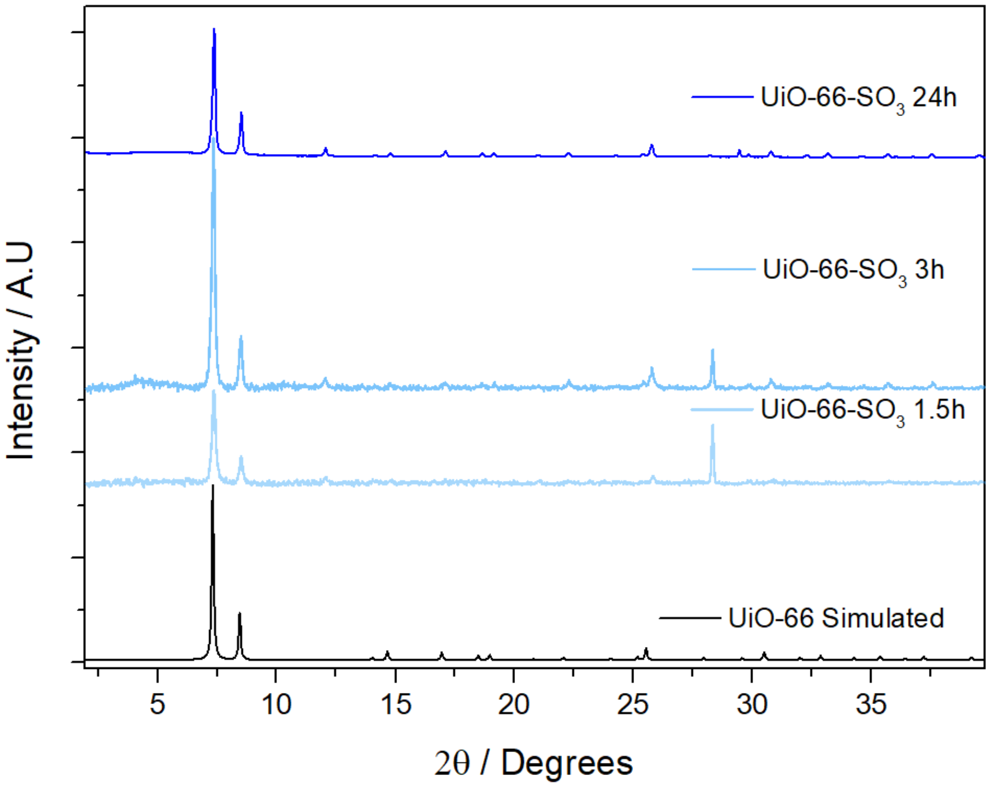

Figure S75: PXRD patterns of UiO-66-SO3 synthesised with p-SO3-benzoic acid at different reaction times, 1.5h, 3h and 24h. The samples initially show a new Bragg reflection band at ca. 28.3 2tetha degrees, which could correspond to cluster condensed phases[9] but might also align with the <622> hkl reflection.[10]

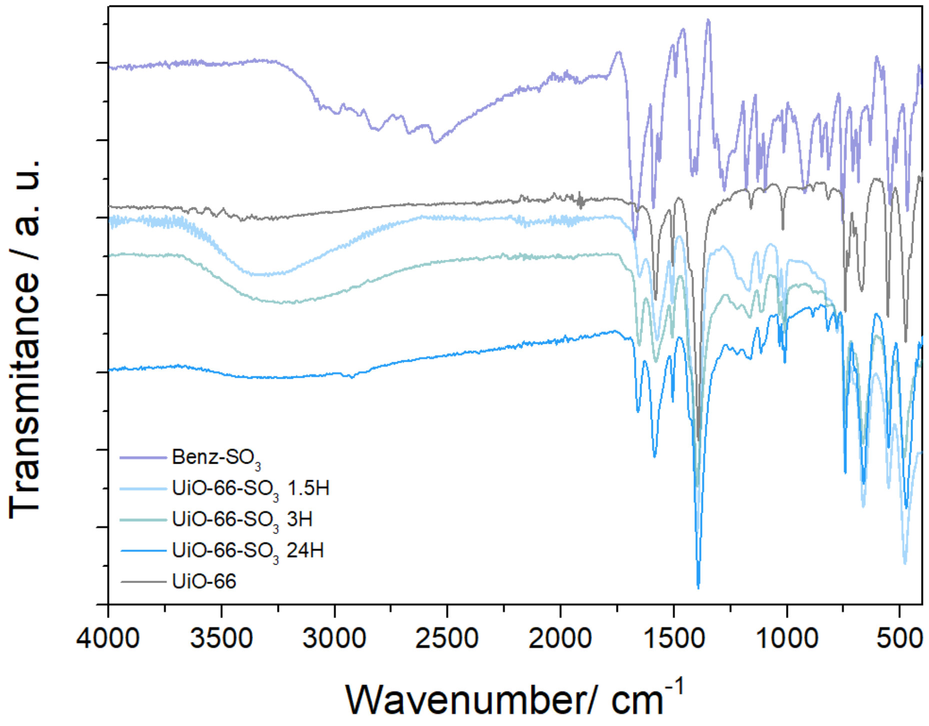

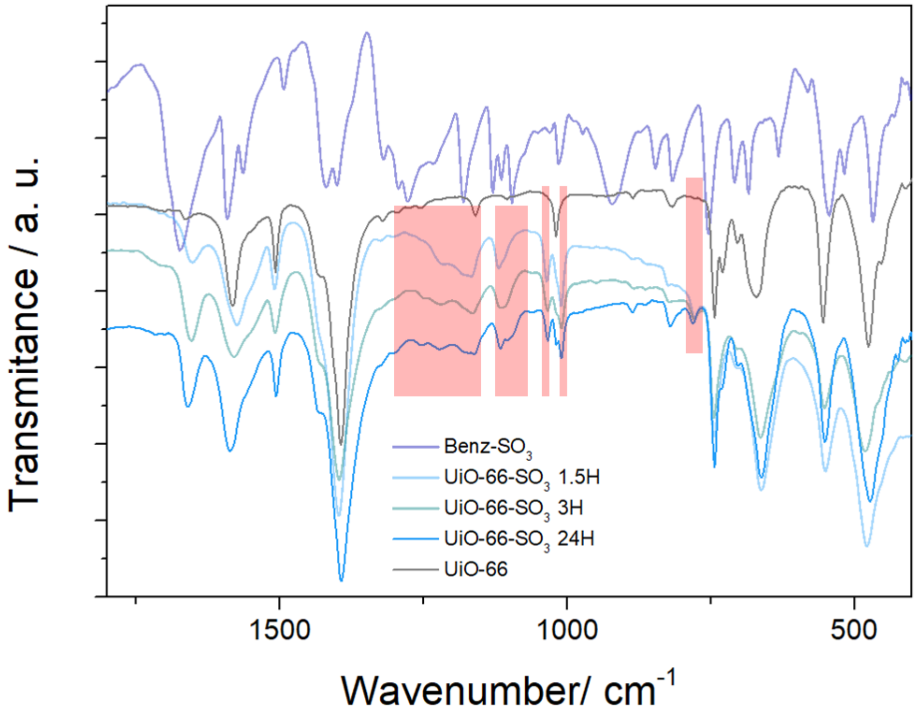

Figure S76: FT-IR profiles of UiO-66-SO_3 synthesised with different reaction times, compared to the free modulator and UiO-66. The incorporation of Benz-SO_3 can be observed for all the reaction stages, with new bands attributed to asymmetric and symmetric stretching frequencies of sulfonate,[2] at 1115 ($\nu_{as}SO_3$), 1032 ($\nu_{as}SO_3$) and 1010 (ν_sSO_3) cm^{-1}. These bands are shifted in comparison with the free modulator due to the partial attachment of sulfonate groups to Zr clusters. A new band at 780 cm^{-1} (C-S stretching) is observed in the FT-IR spectra of SO_3-containing-MOFs.

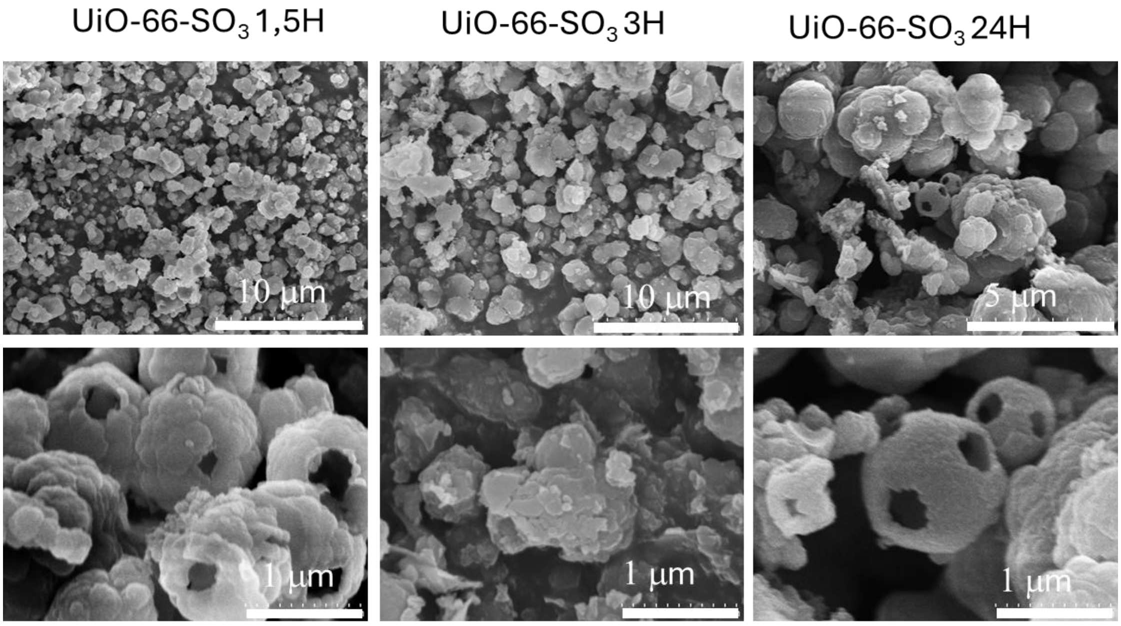

Figure S77: SEM images of UiO-66-SO_3 synthesised with different reaction times, 1.5h, 3h and 24h.

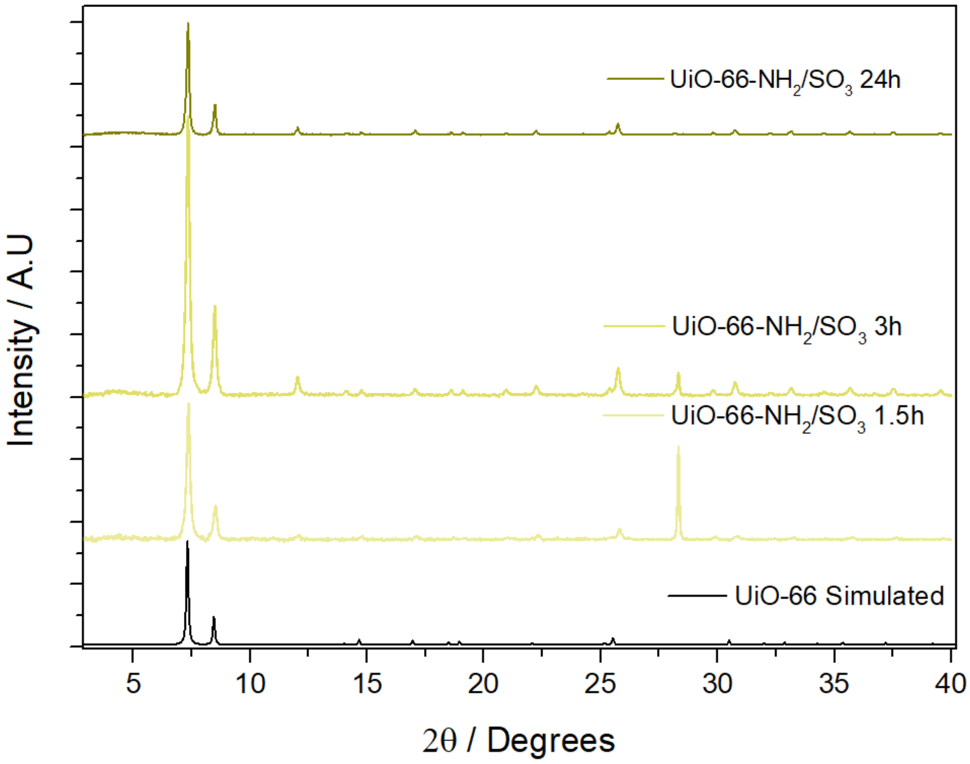

Figure S78: PXRD patterns of UiO-66-NH_2/SO_3 synthesised with p-NH_2-benzoic acid and p-SO_3-benzoic acid with different reaction times, 1.5h, 3h and 24h. The samples initially show a new Bragg reflection band at ca. 28.3 2tetha degrees, which could correspond to cluster condensed phases[9] but might also align with the <622> hkl reflection. [10]

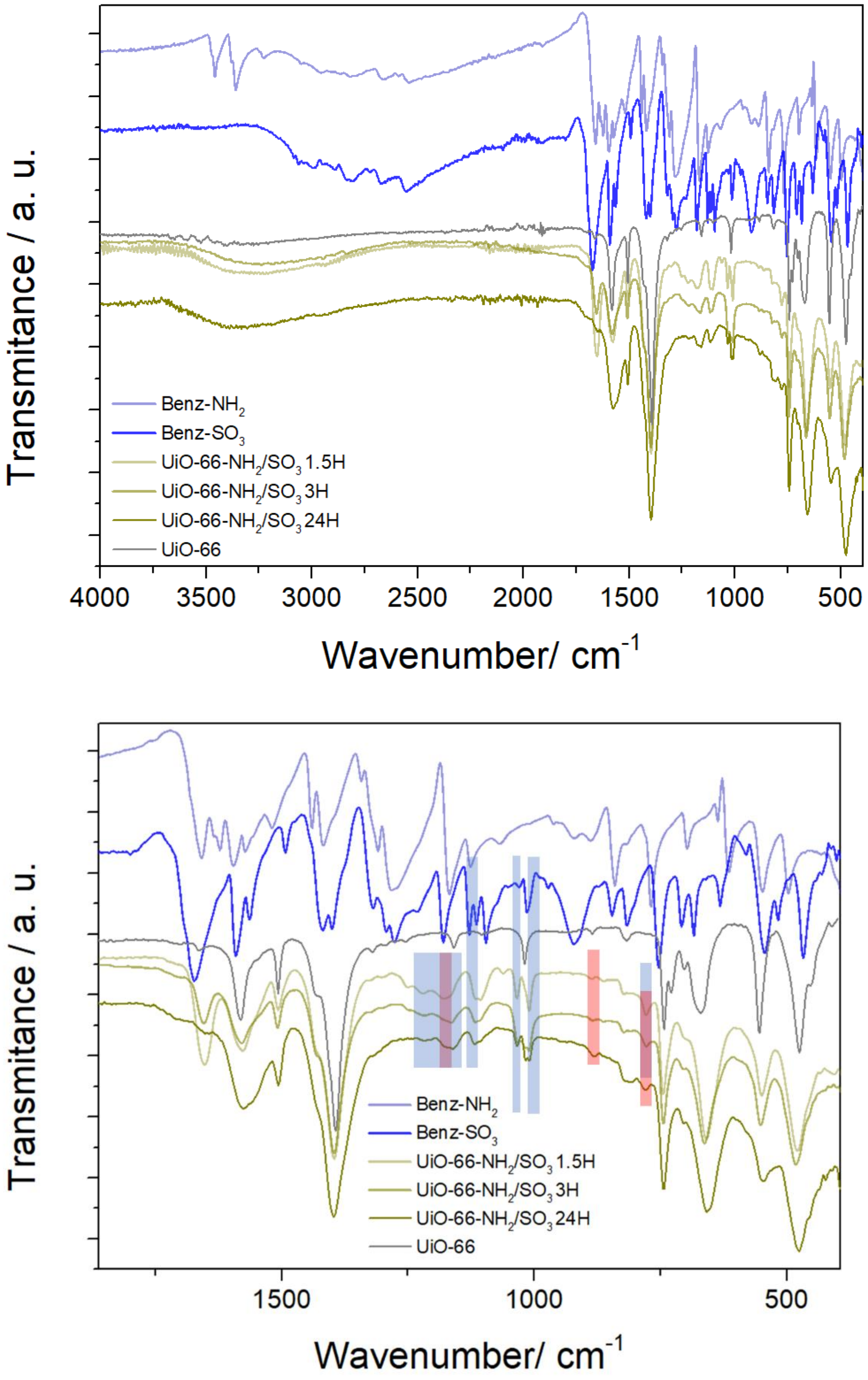

Figure S79: FT-IR profiles of UiO-66-NH$_2$/SO$_3$ synthesised with different reaction times, compared to the free modulators and UiO-66.Bands from both Benz-NH$_2$ and Benz-SO$_3$ modulators can be observed, highlighted in blue for Benz-SO$_3$ ($\nu_{as}SO_3$ at ca. 1115 cm^{-1} and 1032 cm^{-1} and $\nu_{s}SO_3$ at ca. 1010 cm^{-1}) and red for Benz-NH$_2$ (C-N $_{st}$ at ca. 1179 cm^{-1} and the NH$_2$ δ at 861 cm^{-1} and ca. 798 cm^{-1}).

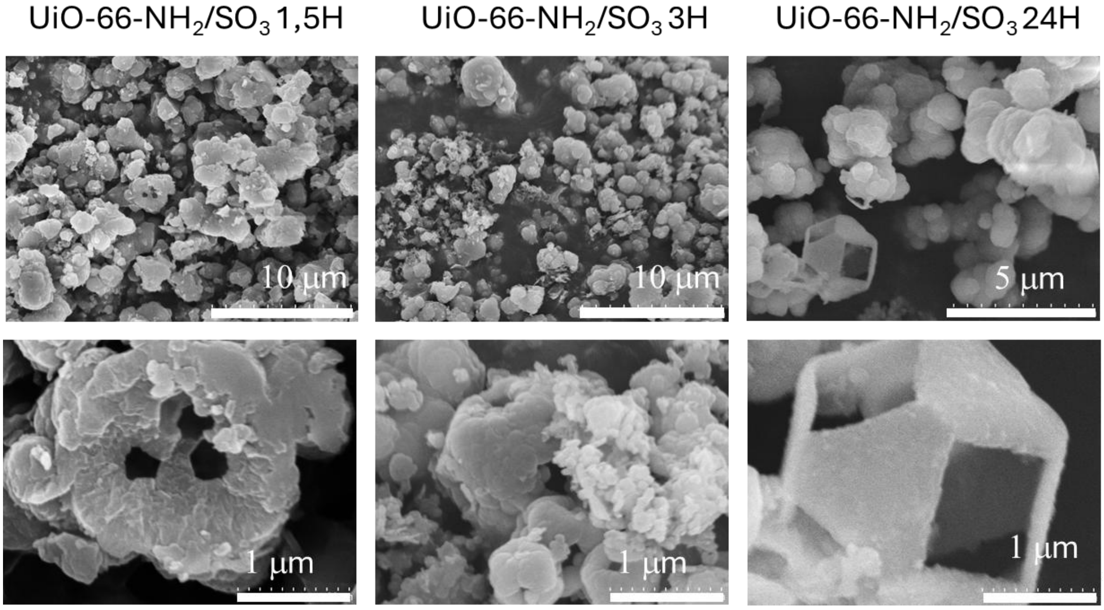

Figure S80: SEM images of UiO-66-NH_2/SO_3 synthesised with different reaction times, 1.5h, 3h and 24h.

S.6. CO_2 Adsorption and Desorption Measurements

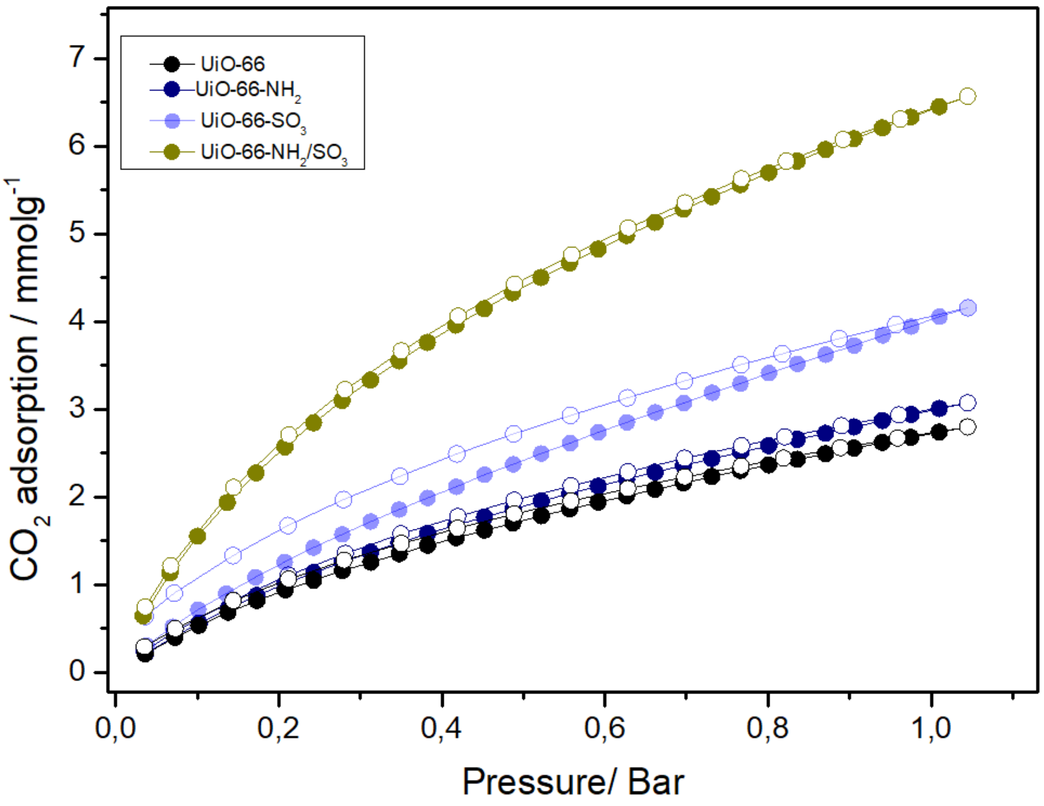

Figure S81: CO_2 adsorption and desorption isotherms at 273K of UiO-66 MOFs.

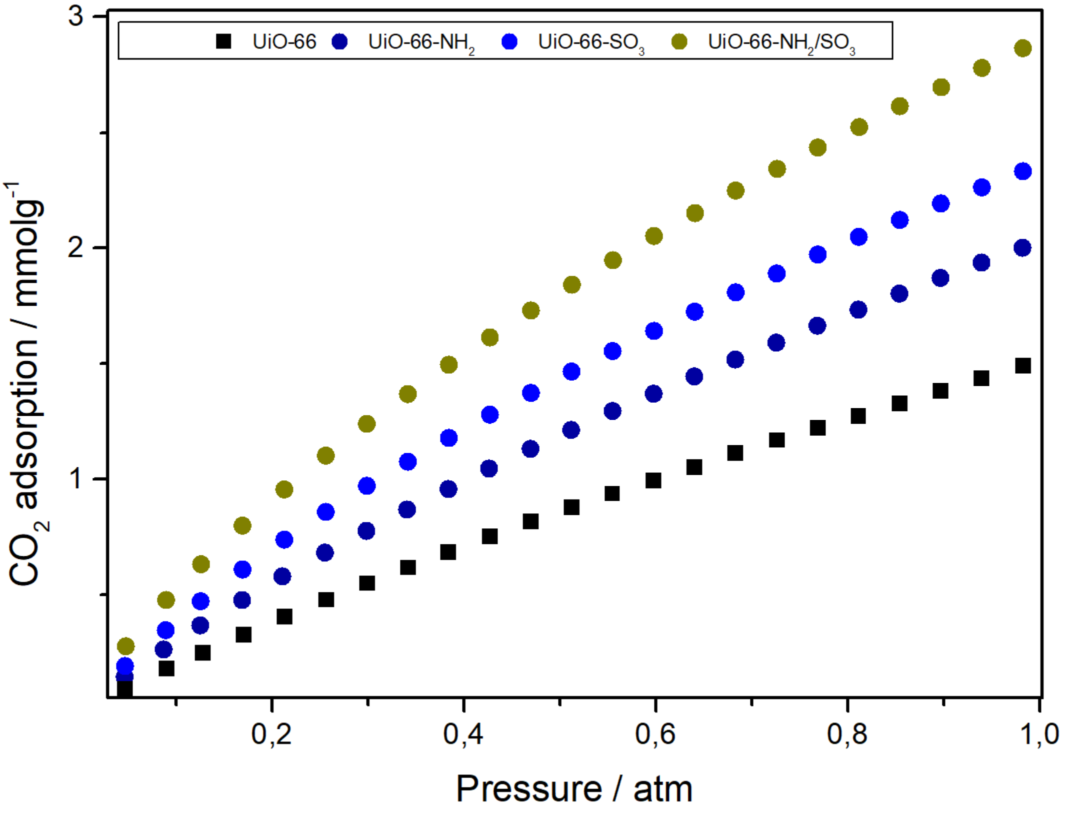

Figure S82: CO_2 adsorption isotherms at 293K of UiO-66 MOFs.

S.7. CO_2 Adsorption of MOFs containing different quantities of modulators

Following the synthetic conditions of S.2, different equivalents of the modulators were introduced to fine-tune the modulator content of the samples. In 8 mL vials, $ZrCl_4$ (0.45 mmol, 1 equivalent, 104.9mg), terephthalic acid (0.45 mmol, 1 equivalent, 74.8 mg), and the modulators (0.9 mmol for 2 equivalents or 2.25 mmol for 5 equivalents) were dissolved in 5 mL of DMF with 0.35 mL of glacial acetic acid. The reaction mixtures were sonicated for 5 minutes and placed in an oven at 120ºC. After 24 hours, the reaction mixtures were cooled down to room temperature.

S.7.1 CO_2 Adsorption of MOFs variable modulator UiO-66-NH_2

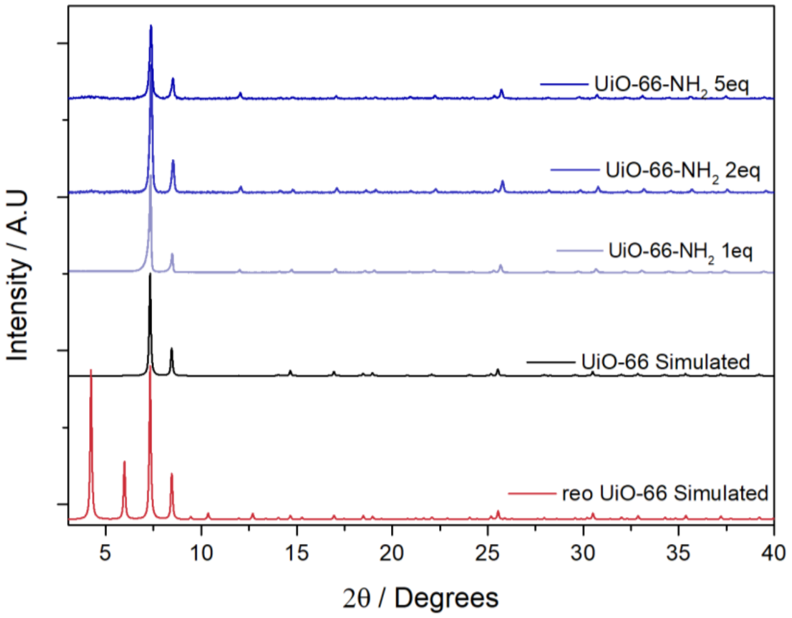

.

Figure S83: PXRD patterns of UiO-66-NH_2 synthesised with different equivalents of Benz-NH_2.

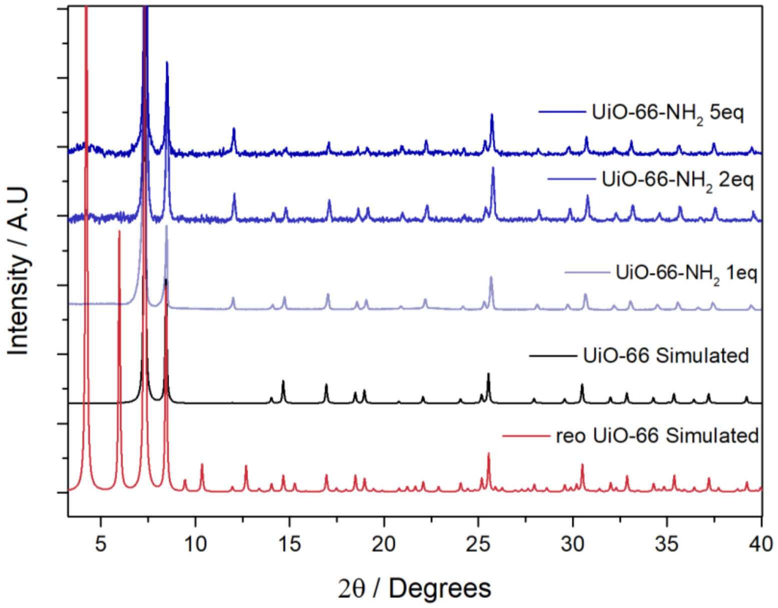

.

Figure S84: PXRD patterns of UiO-66-NH_2 synthesised with different equivalents of Benz-NH_2.

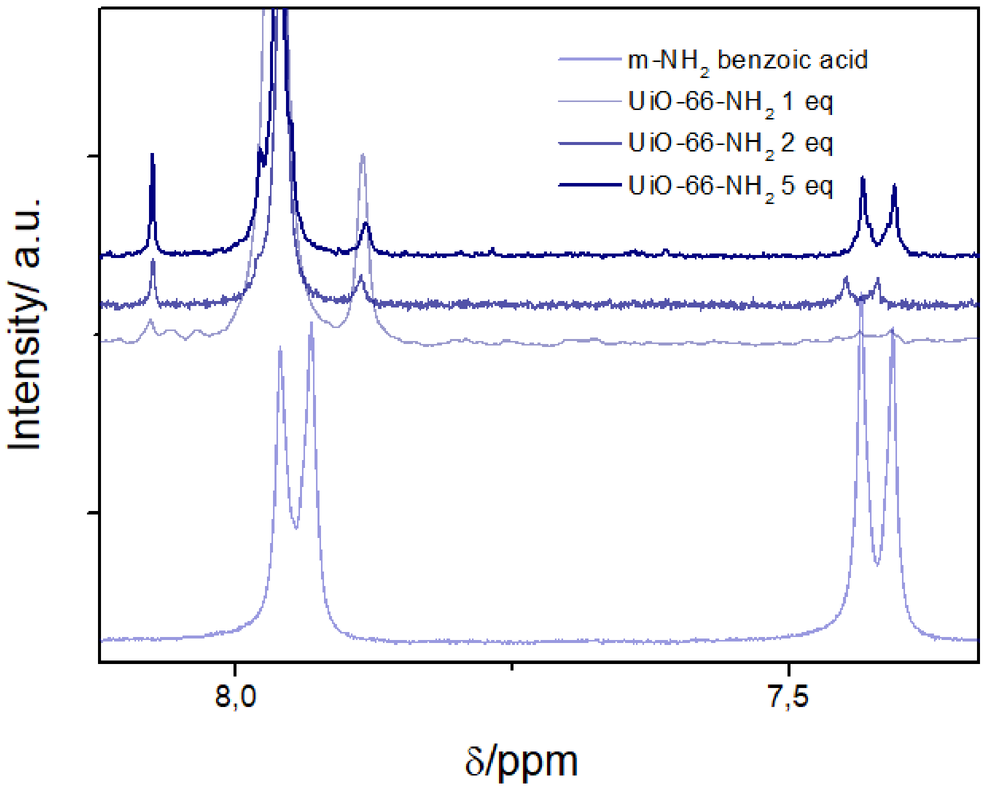

Figure S85: ^{1}H NMR profiles of acid-digested UiO-66-NH$_2$ synthesised with different equivalents of Benz-NH$_2$, compared to the free modulator.

Table S10: Tabulated data extracted from acid-digested ^{1}HNMR of activated UiO-66-NH$_2$ MOFs, expressed in molar and molar percentage ratio compared to the linker.

Samples	**NH$_2$/BDC**	**%NH$_2$**
UiO-66-NH$_2$ 1 eq	0.061	4.667
UiO-66-NH$_2$ 2 eq	0.093	8.475
UiO-66-NH$_2$ 5 eq	0.234	18.993

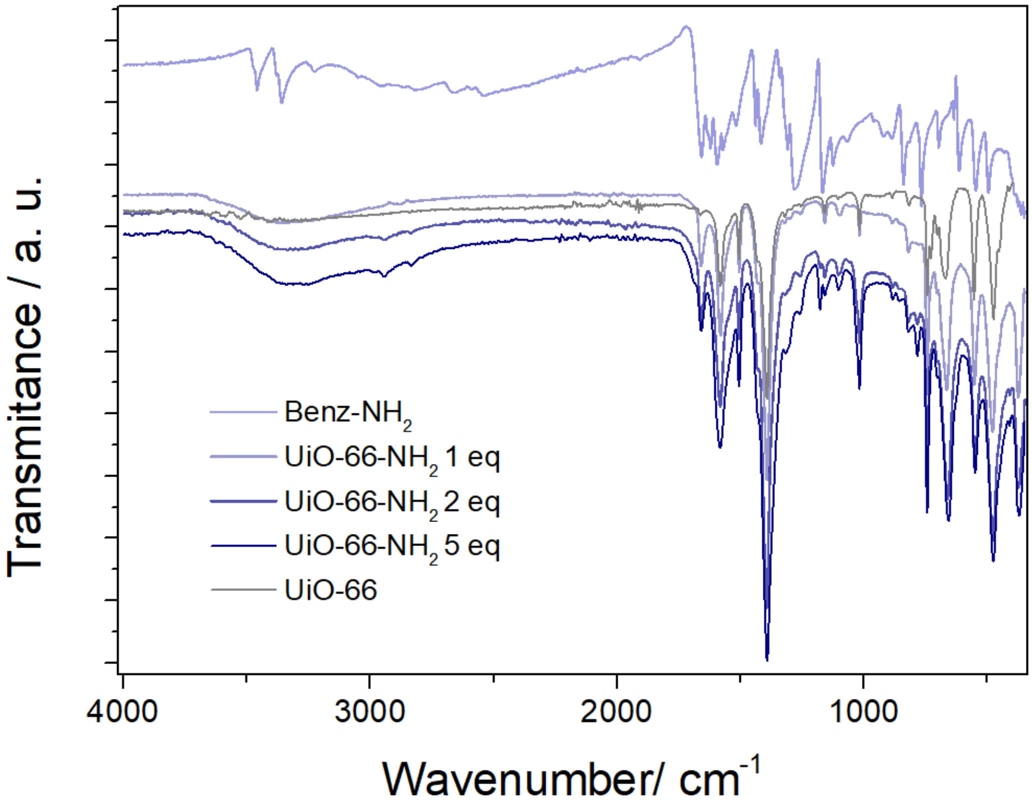

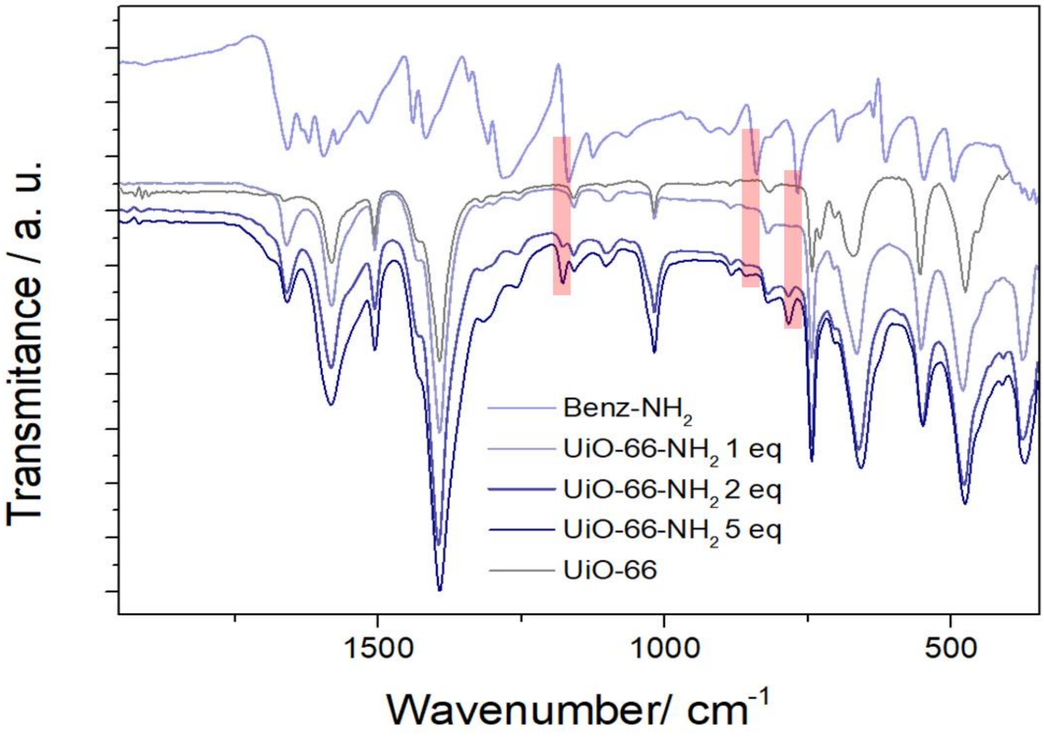

Figure S86: FT-IR profiles of UiO-66-NH$_2$ synthesised with different equivalents of Benz-NH$_2$, compared to the free modulator and UiO-66. Benz-NH$_2$ signals, such as the C-N $_{st}$ (ca. 1179 cm^{-1}) and the NH$_2$ δ (861 cm^{-1} and ca. 798 cm^{-1}) can be observed as more Benz-NH$_2$ is incorporated.

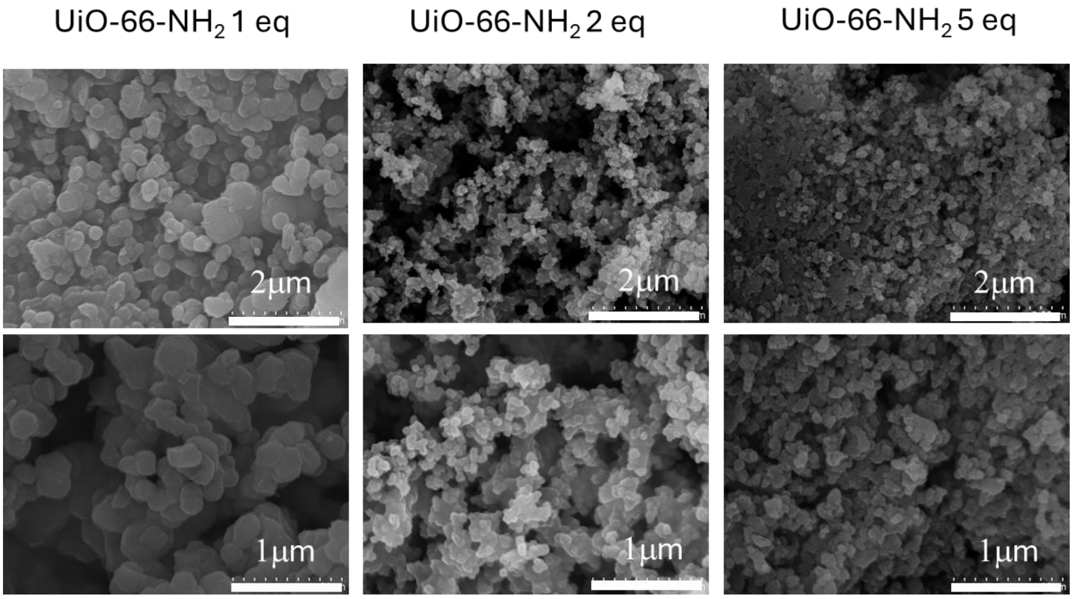

Figure S87: SEM images of UiO-66-NH_2 synthesised with different equivalents of Benz-NH_2.

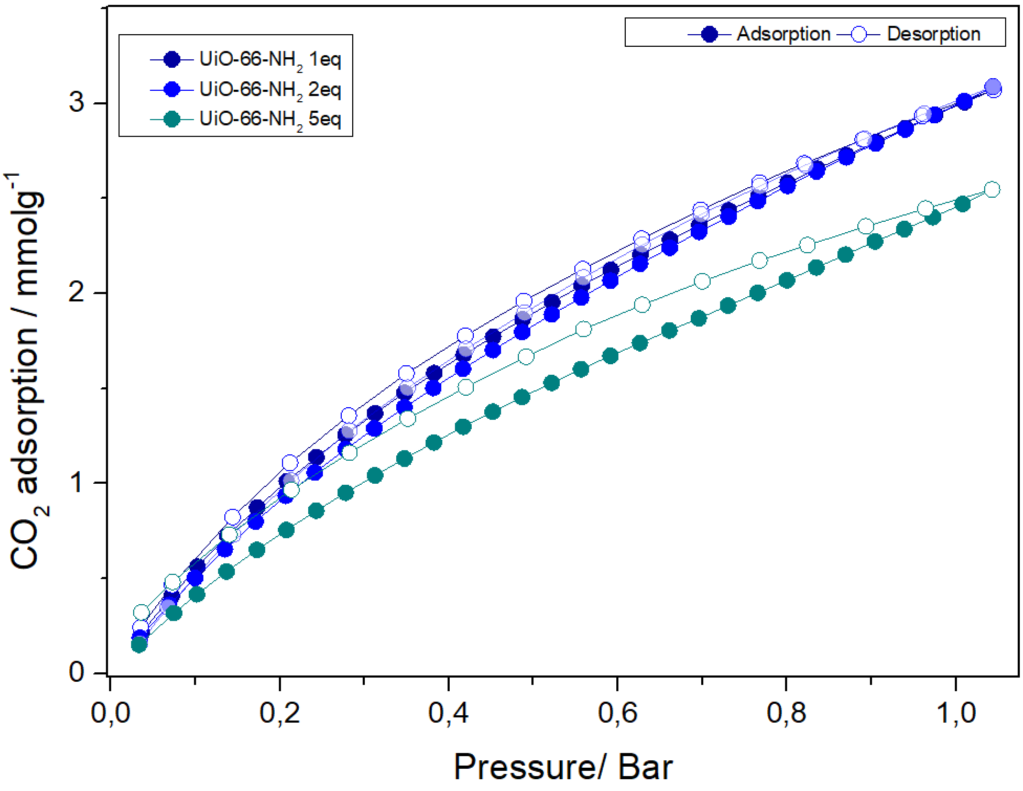

Figure S88: CO_2 adsorption and desorption isotherms at 273 K of UiO-66-NH_2 synthesised with different equivalents of Benz-NH_2, showing that the inclusion of higher amounts of Benz-NH_2 into the framework does not increase the adsorption capacity.

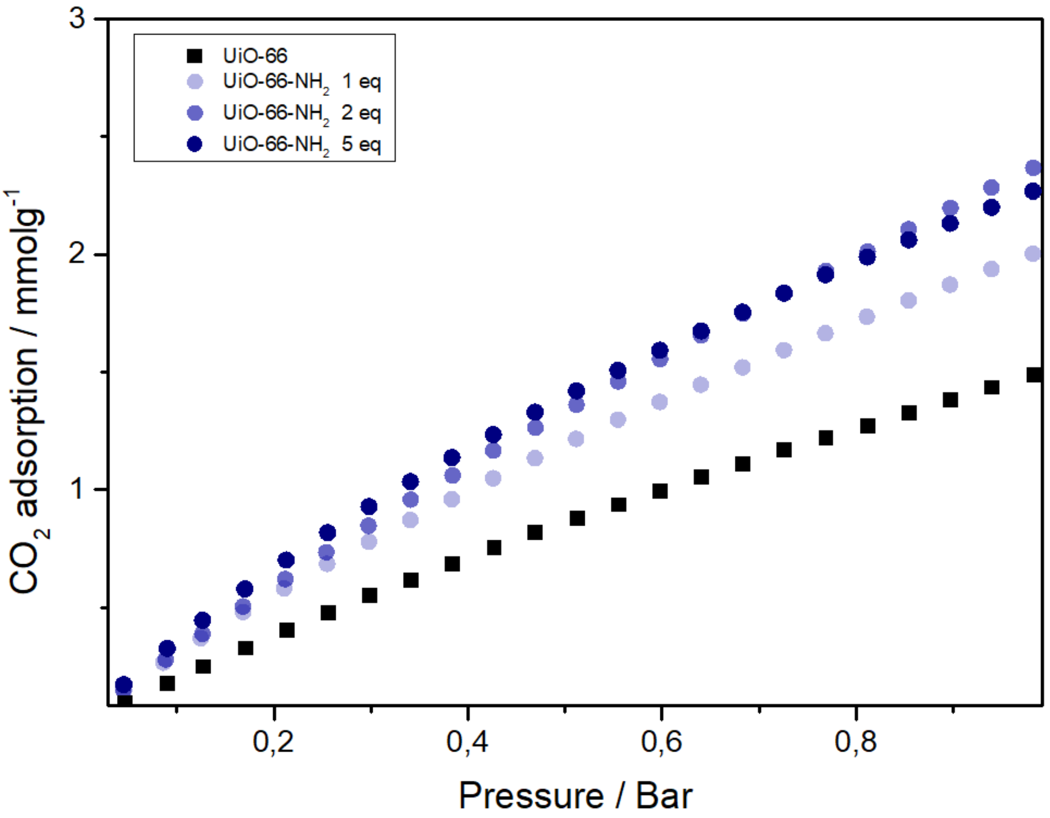

Figure S89: CO_2 adsorption and desorption isotherms at 293 K of UiO-66-NH_2 synthesised with different equivalents of Benz-NH_2, showing that the inclusion of higher amounts of Benz-NH_2 into the framework does not increase the adsorption capacity.

S.7.2 CO_2 Adsorption of MOFs variable modulator UiO-66-SO_3

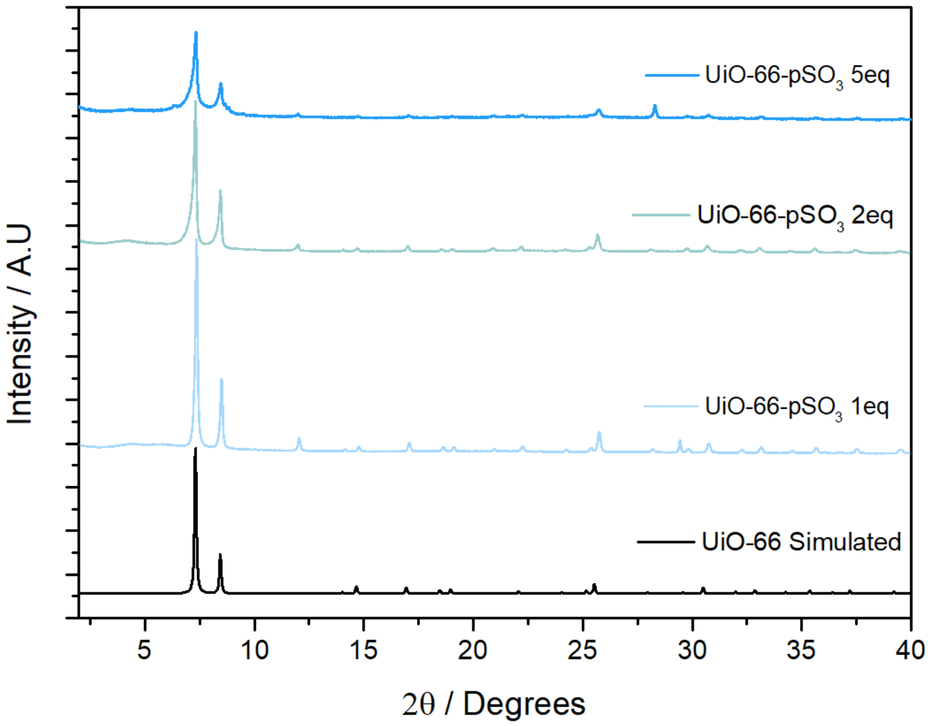

Figure S90: PXRD patterns of UiO-66-SO_3 synthesised with different equivalents of Benz-SO_3.

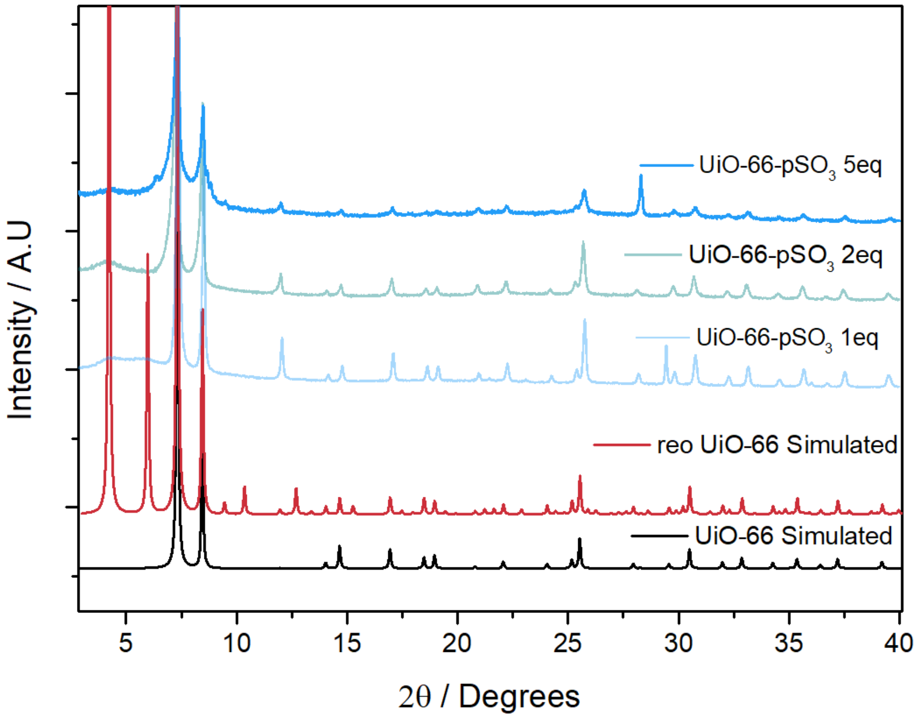

Figure S91: PXRD patterns of UiO-66-SO_3 synthesised with different equivalents of Benz-SO_3. Note that the sample synthesised with 5 equivalents is not phase pure.

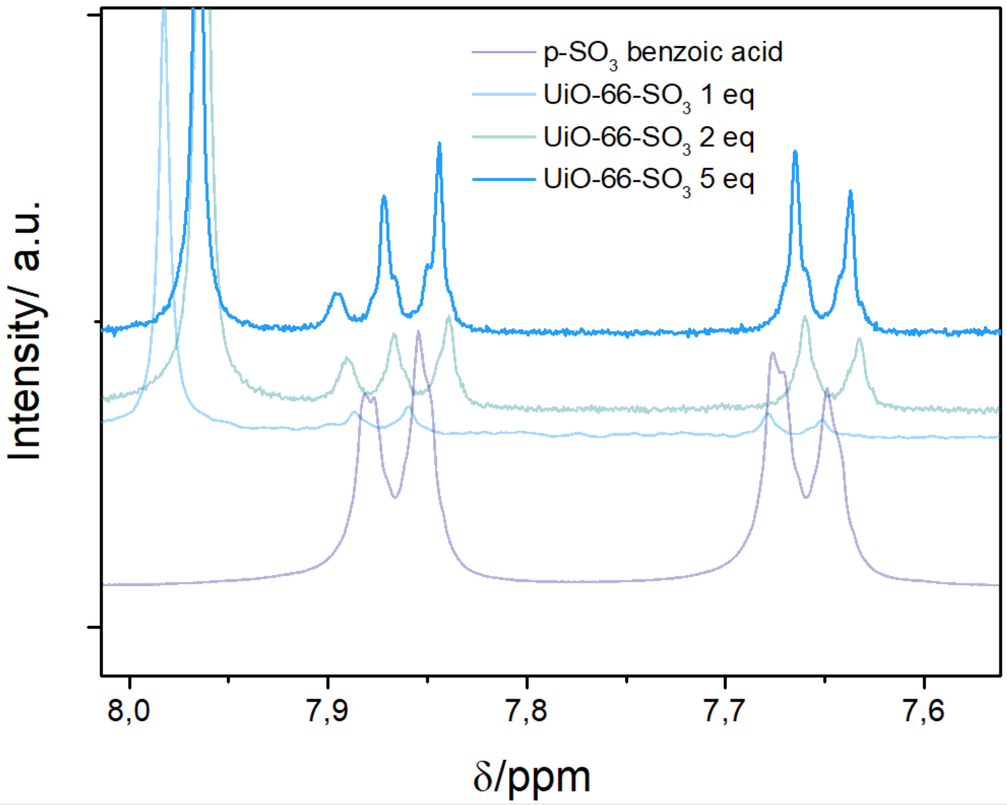

Figure S92: ^{1}HNMR profiles of acid-digested UiO-66-SO$_3$ synthesised with different equivalents of Benz-SO$_3$, compared to the free modulator.

Table S11: Tabulated data extracted from acid-digested ^{1}HNMR of activated UiO-66-SO$_3$ MOFs, expressed in molar and molar percentage ratio compared to the linker.

Samples	**SO$_3$/BDC**	**% SO$_3$**
UiO-66-SO$_3$ 1 eq	0.200	21.875
UiO-66-SO$_3$ 2 eq	0.750	27.285
UiO-66-SO$_3$ 5 eq	1.980	49.751

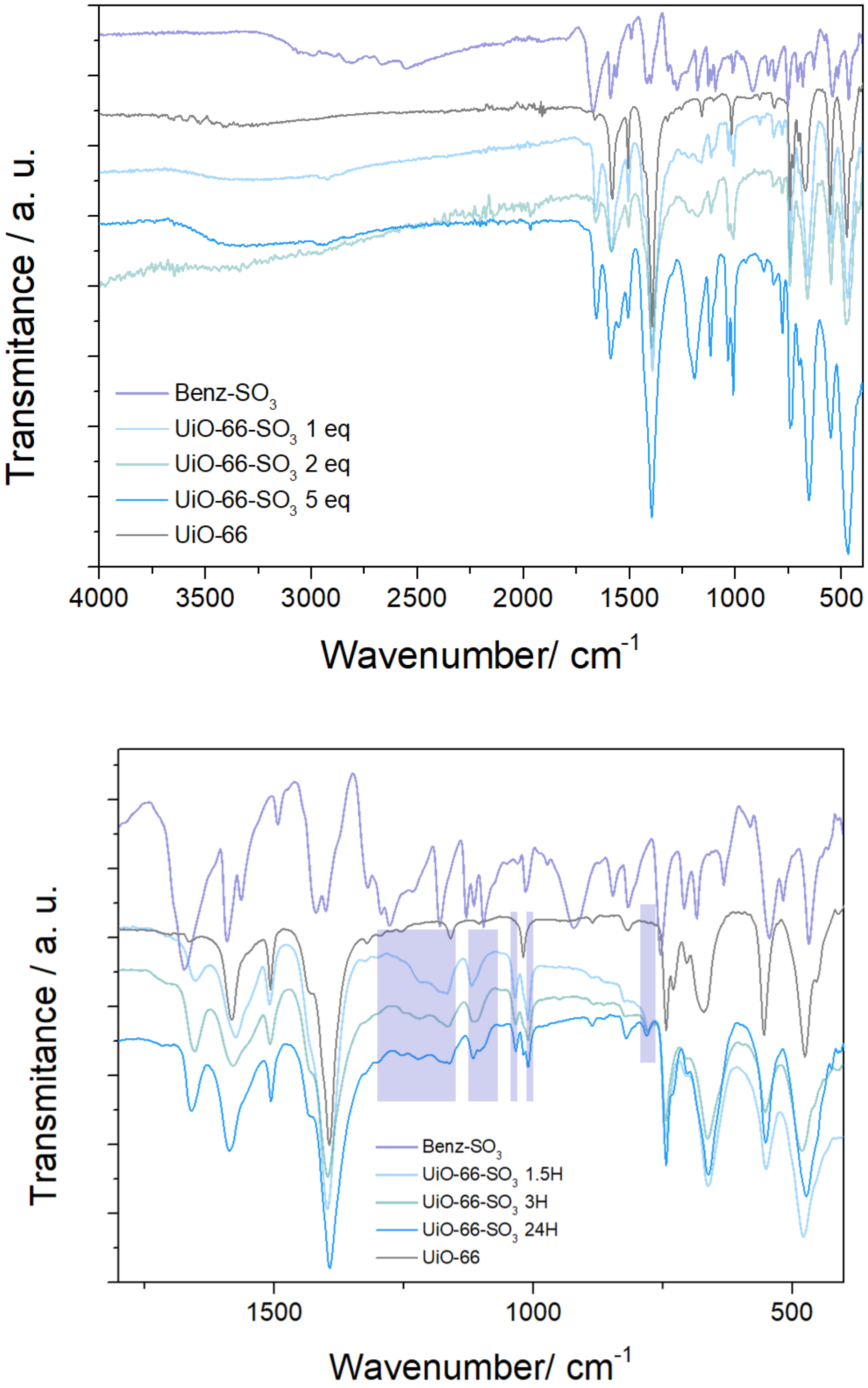

Figure S93: IR profiles of UiO-66-SO$_3$ synthesised with different equivalents of Benz-SO$_3$, compared to the free modulator and UiO-66. UiO-66-SO$_3$ samples displayed new bands attributed to asymmetric and symmetric stretching frequencies of sulfonate,[2] at 1115 ($\nu_{as}SO_3$), 1032 ($\nu_{as}SO_3$) and 1010 ($\nu_{s}SO_3$) cm^{-1}. These bands are shifted in comparison with the free modulator due to the partial attachment of sulfonate groups to Zr clusters. A new band at 780 cm^{-1} (C-S stretching) is observed in the FT-IR spectra of SO$_3$-containing-MOFs.

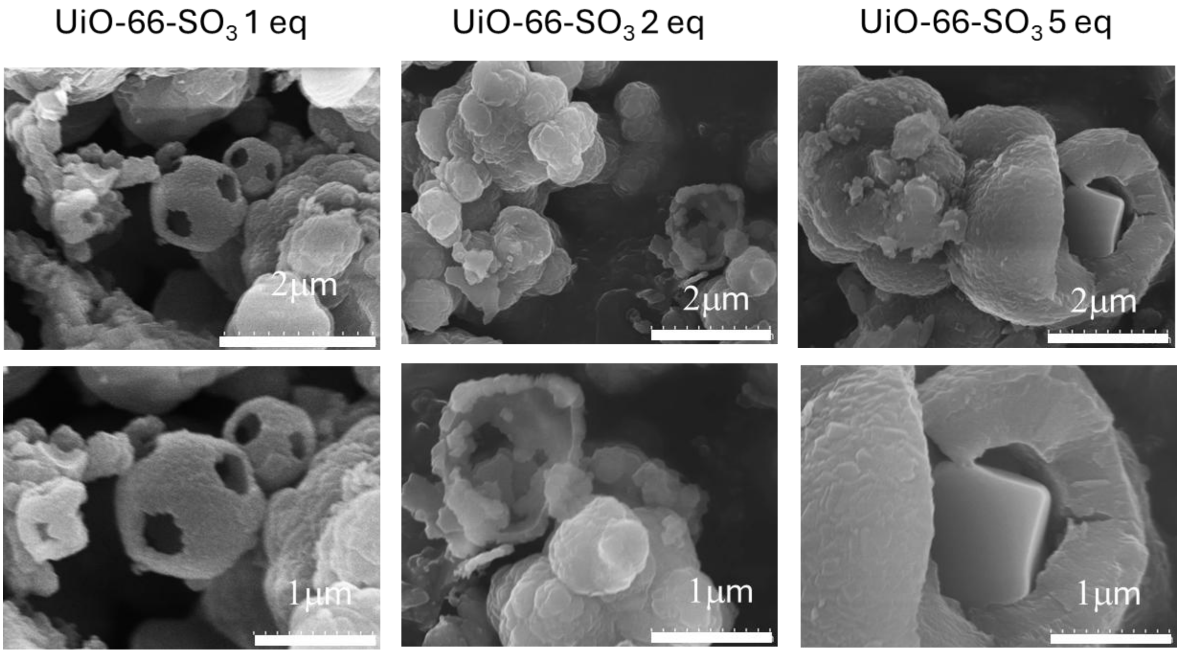

Figure S94: SEM images of UiO-66-SO$_3$ synthesised with different equivalents of Benz-SO$_3$.

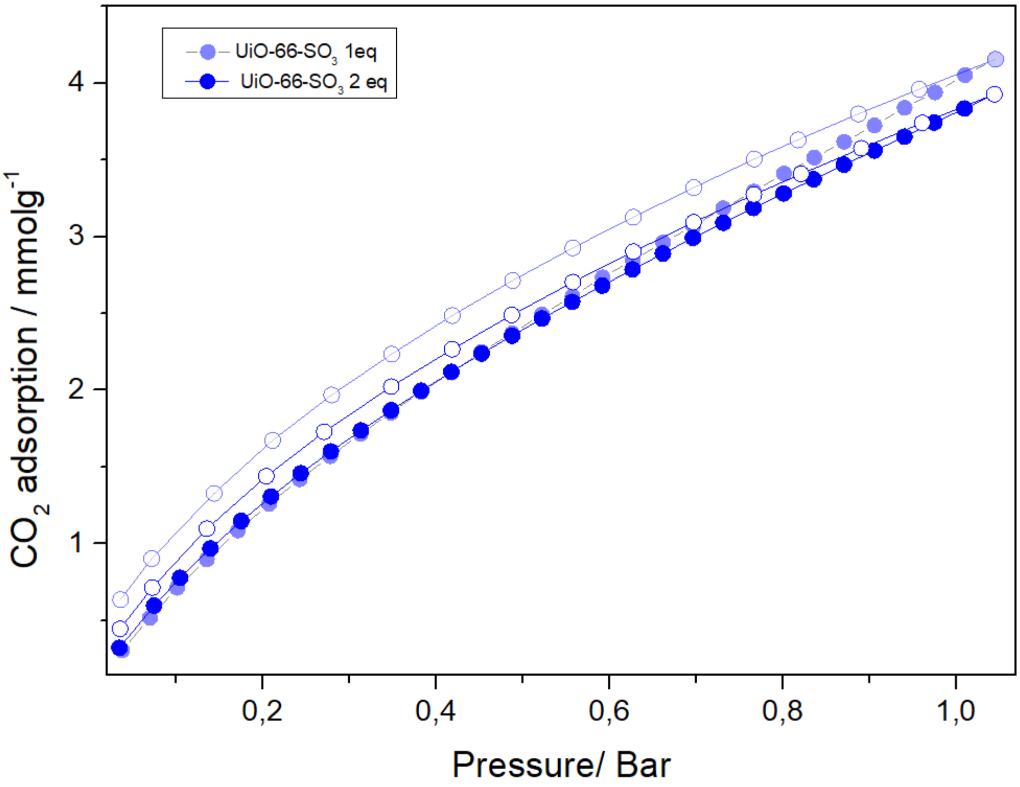

Figure S95: CO$_2$ adsorption and desorption isotherms at 273 K of UiO-66-SO$_3$ synthesised with different equivalents of (para)Benz-SO$_3$. Given that PXRD revealed a phase impurity for the material synthesised with 5 equivalents, its isotherm was not recorded.

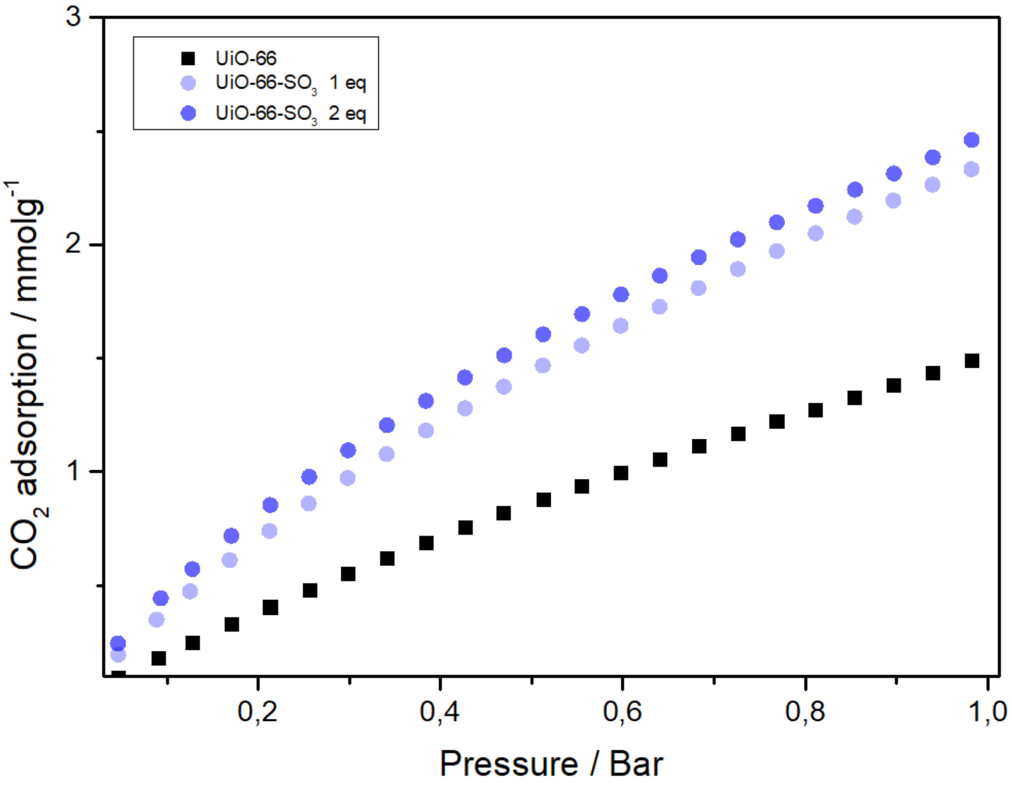

Figure S96: CO_2 adsorption and desorption isotherms at 293 K of UiO-66-SO_3 synthesised with different equivalents of (para)Benz-SO_3. Given that PXRD revealed a phase impurity for the material synthesised with 5 equivalents, its isotherm was not recorded.

S.7.3 CO_2 Adsorption of MOFs variable modulator UiO-66-NH_2/SO_3

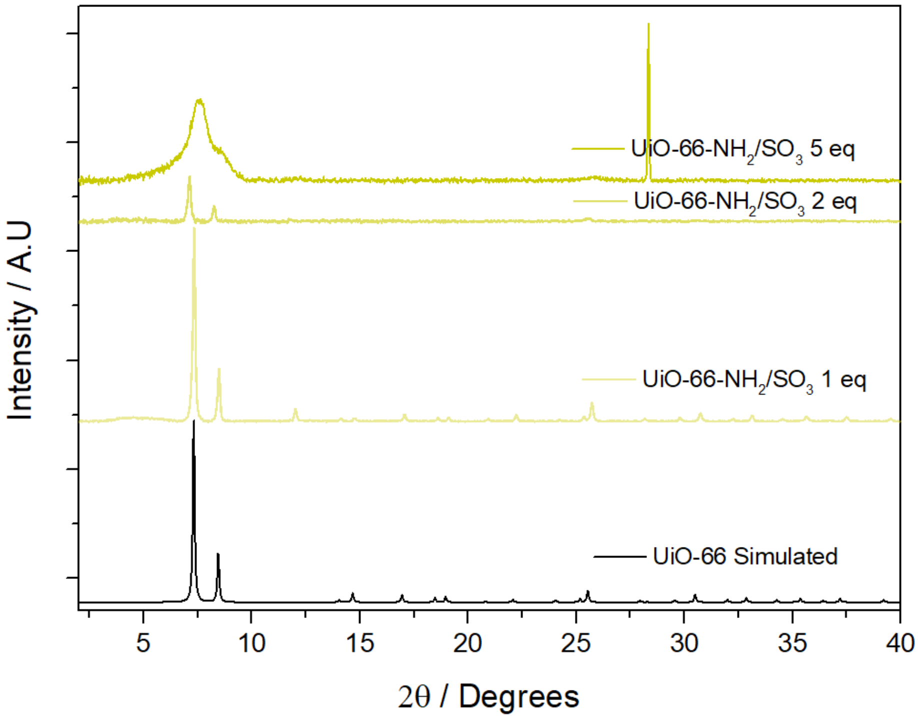

Figure S97: PXRD patterns of UiO-66-NH_2/SO_3 synthesised with different equivalents of p-SO_3 benzoic acid and p-NH_2-benzoic acid. Note that the sample synthesised with 5 equivalents of each modulator presents a new Bragg reflection band at ca. 28.3 2 tetha degrees, which could correspond to cluster condensed phases[9] but might also align with the <622> hkl reflection. [10]

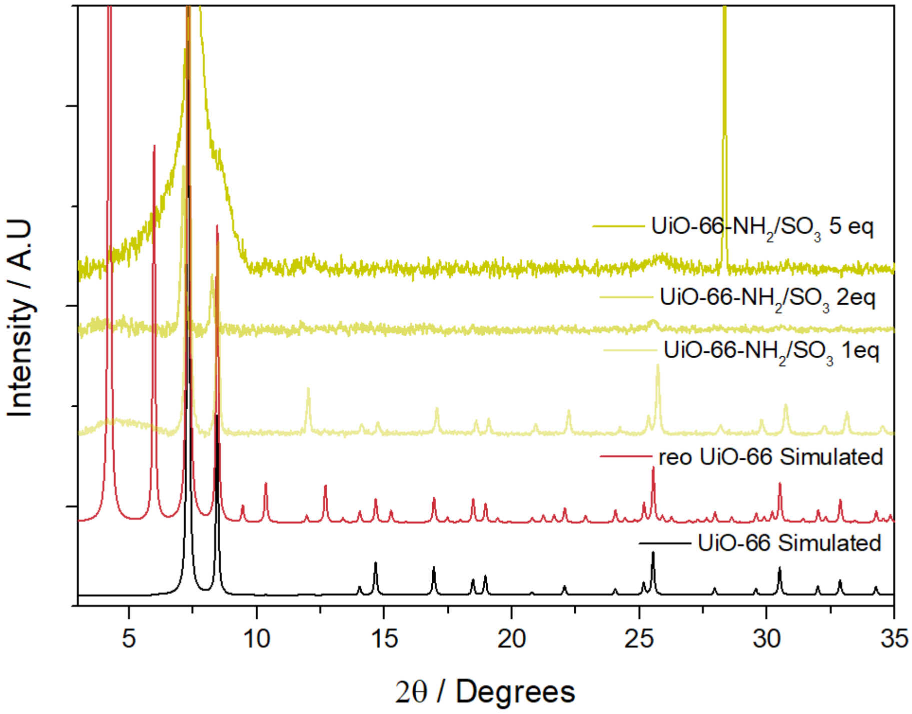

Figure S98: PXRD patterns of UiO-66-NH_2/SO_3 synthesised with different equivalents of p-SO_3 benzoic acid and p-NH_2-benzoic acid.

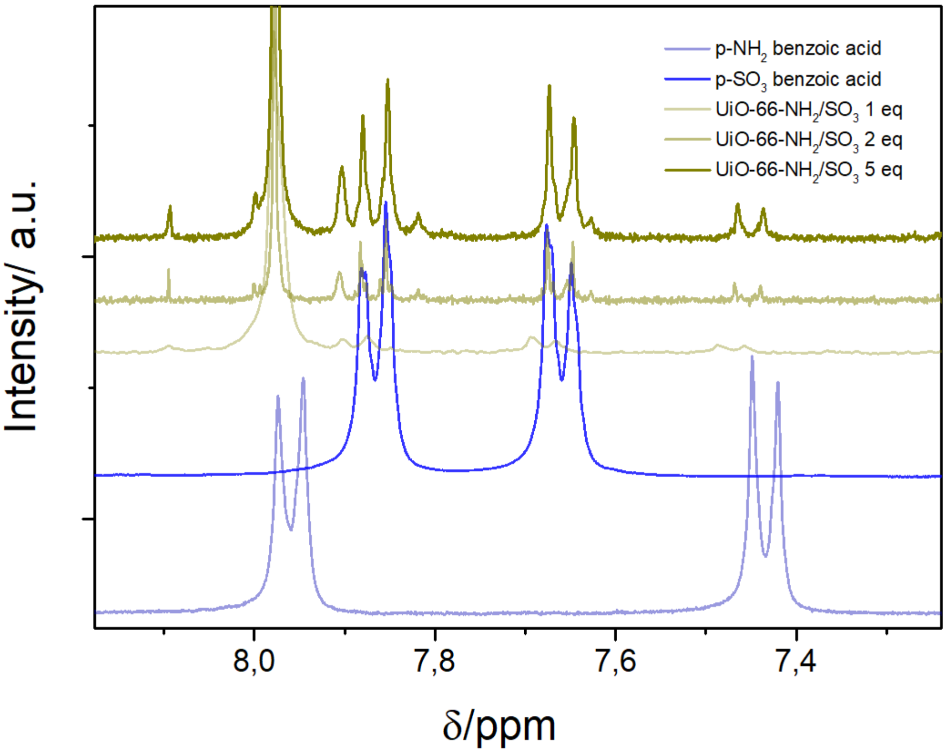

Figure S99: ^{1}HNMR profiles of acid-digested UiO-66-NH_2/SO_3 synthesised with different equivalents of p-NH_2 and p-SO_3 benzoic acid.

Table S12: Tabulated data extracted from acid-digested ^{1}HNMR of activated MTVM UiO-66 MOFs, expressed in molar ratio compared to the linker.

Sample	**NH_2/BDC**	**SO_3/BDC**	**%NH_2**	**%SO_3**
UiO-66-NH_2/SO_3 1 eq	0.133	0.317	11.765	24.089
UiO-66-NH_2/SO_3 2 eq	0.062	0.848	5.821	29.774
UiO-66-NH_2/SO_3 5 eq	0.132	1.357	11.662	40.425

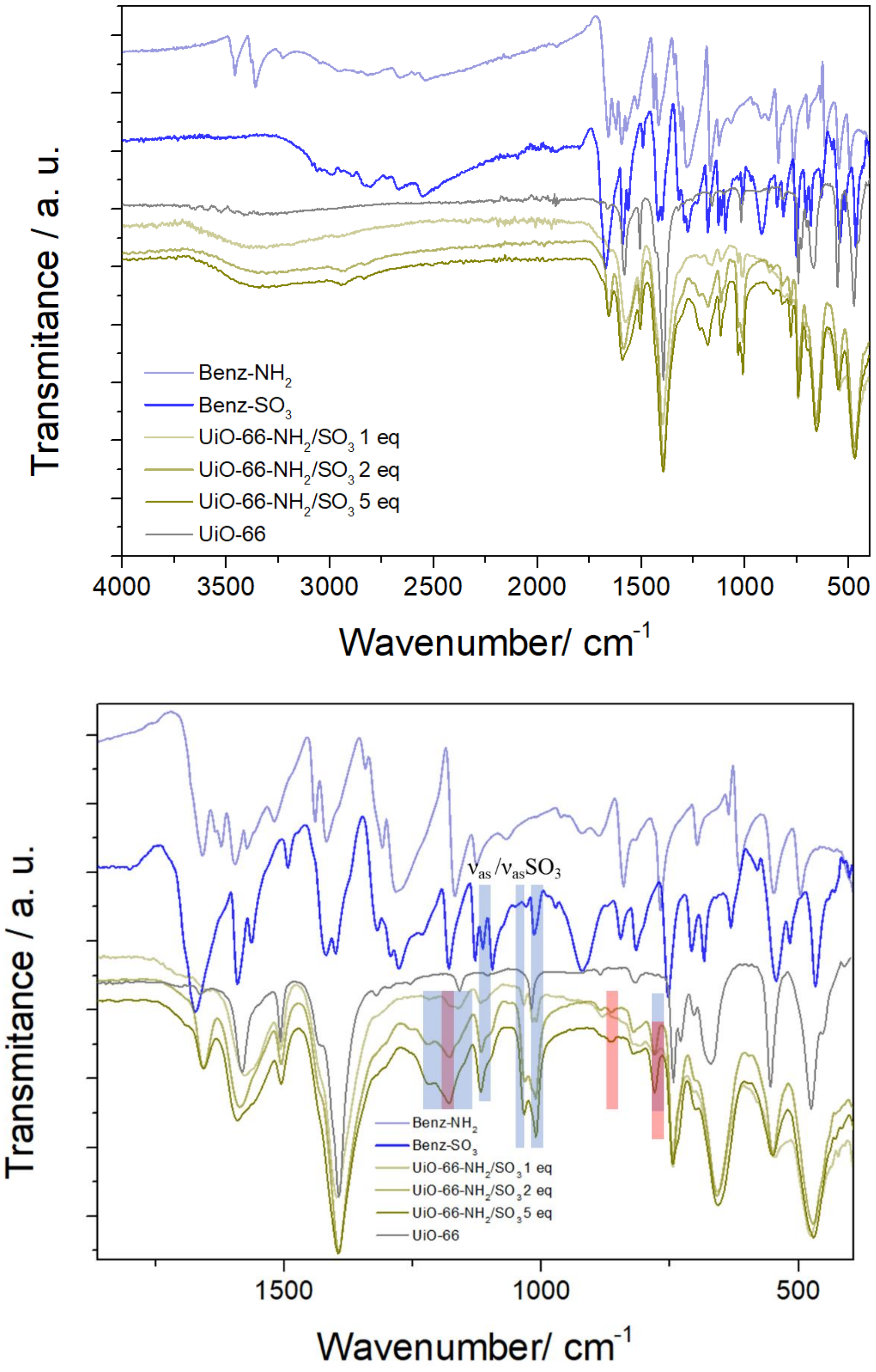

Figure S100: IR profiles of UiO-66-NH_2/SO_3 synthesised with different equivalents of Benz-NH_2 and Benz-SO_3, compared to the free modulators and UiO-66. Bands from both Benz-NH_2 and Benz-SO_3 modulators can be observed, highlighted in blue for Benz-SO_3 ($\nu_{as}SO_3$ at ca. 1115 cm^{-1} and 1032 cm^{-1} and ν_sSO_3 at ca. 1010 cm^{-1}) and red for Benz-NH_2 (C-N $_{st}$ at ca. 1179 cm^{-1} and the NH_2 δ at 861 cm^{-1} and ca. 798 cm^{-1}).

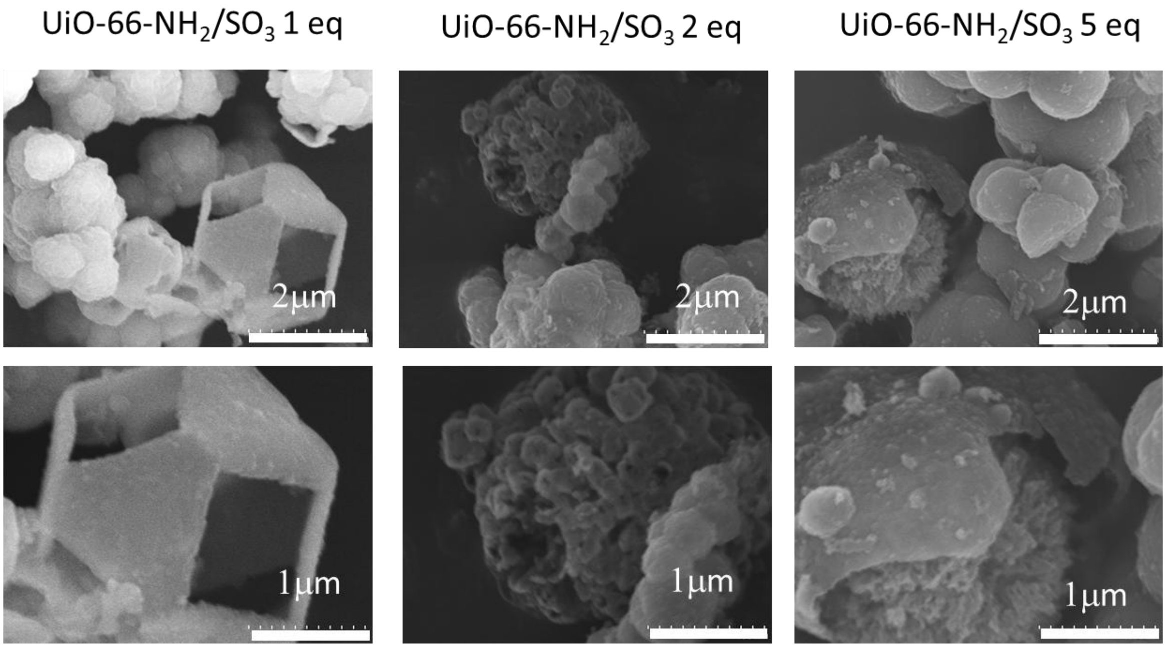

Figure S101: SEM images of UiO-66- NH_2/SO_3 synthesised with different equivalents of Benz-NH_2 and Benz-SO_3.

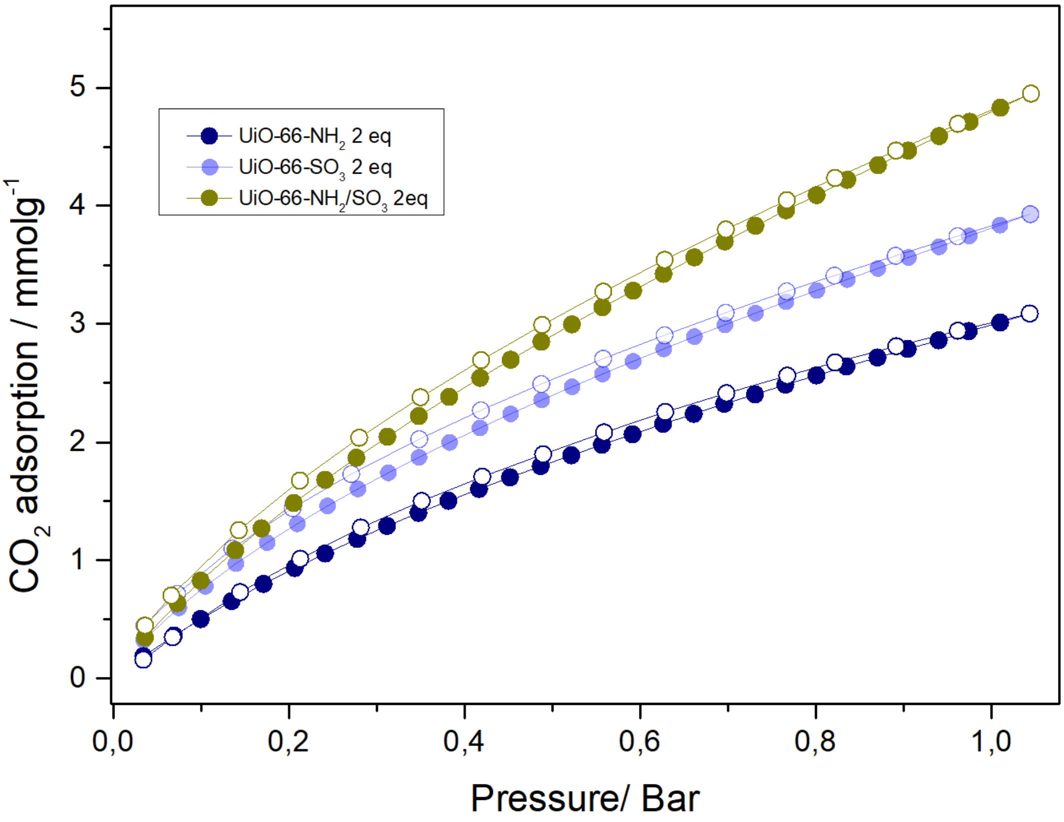

Figure S102: CO_2 adsorption and desorption isotherms at 273K of UiO-66 MOFs synthesised with 2 equivalents of modulators.

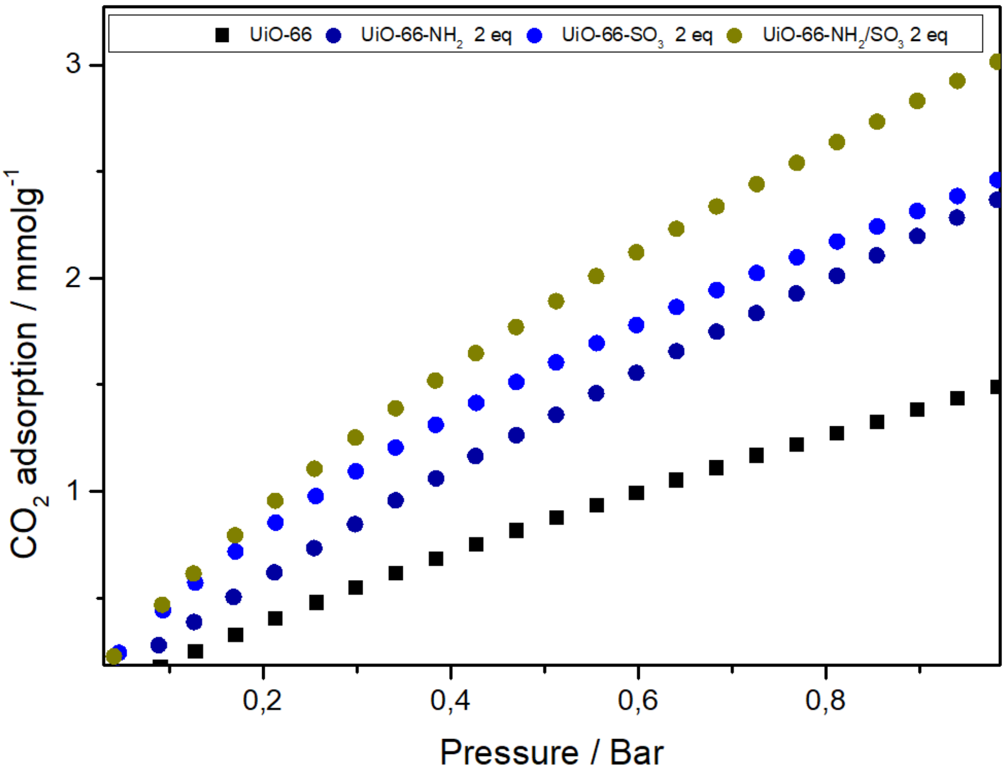

Figure S103: CO$_2$ adsorption and desorption isotherms at 293K of UiO-66 MOFs synthesised with 2 equivalents of modulators.

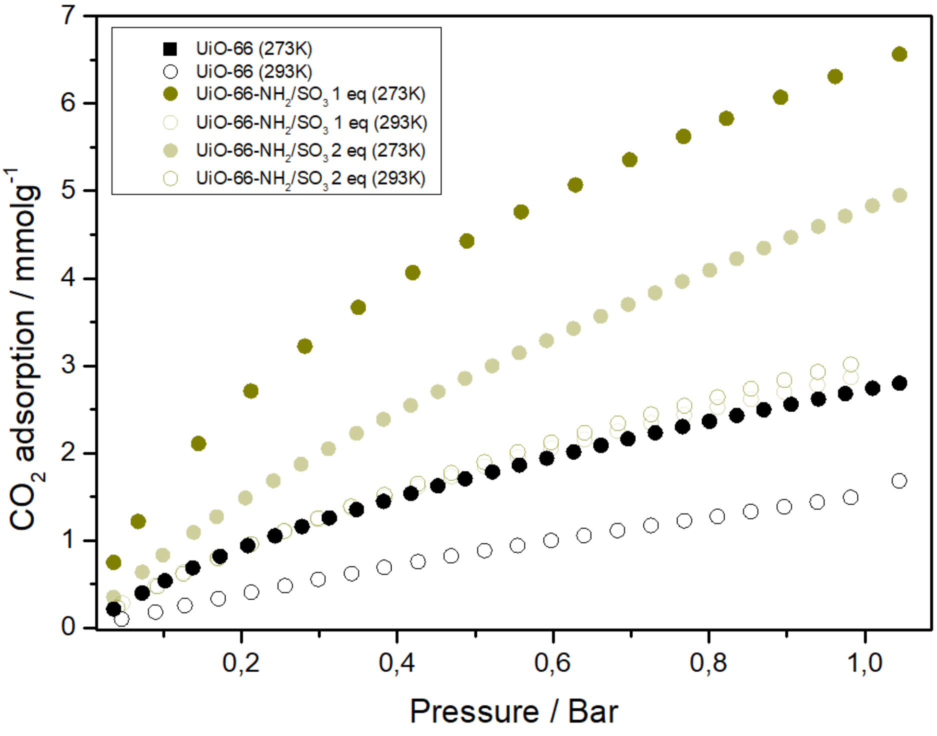

Figure S104: CO$_2$ adsorption and desorption isotherms at 273K and 293K of UiO-66 and UiO-66-NH$_2$/SO$_3$ synthesised with 1 and 2 equivalents of p-functionalised modulators.

S.8. CO_2 Adsorption Simulations

Periodic Density Functional Theory (DFT) calculations were performed using the BEEF-vdW[11] exchange-correlation functional to optimize 2x2x1 supercell model systems from a pristine UiO-66 model system with two inorganic $[Zr_6O_4(OH)_4]^{12+}$ bricks and ten terephthalate linkers to accommodate the defectivity determined by TGA. The stoichiometry of different materials was compared to the model systems (**Tables S13** and **S14**).

Table S13: Stoichiometry model used for the simulations (CIF-files are available from DOI:10.5281/zenodo.15472541).

Name **(CIF-filename)**	**Stoichiometry model**
UiO66 **(UiO-66.cif)**	$\{[Zr_6O_4(OH)_4]^{12+}\}_8\{(OOC(C_6H_4)COO)\}_{42}\{OH,H_2O\}_{12}$
UiO-66-NH_2 **(UiO-66-NH2.cif)**	$\{[Zr_6O_4(OH)_4]^{12+}\}_8\{(OOC(C_6H_4)COO)\}_{39}\{(OOC(C_6H_4)NH_2)\}_3\{OH,H_2O\}_{12}$
UiO-66-SO_3 **(UiO-66-SO3.cif)**	$\{[Zr_6O_4(OH)_4]^{12+}\}_7\{(OOC(C_6H_4)COO)\}_{31}\{(OOC(C_6H_4)COOH)\}_3\{(OOC(C_6H_4)SO_3Na)\}_8\{OH,H_2O\}_{11}$
UiO-66-NH_2/SO_3 **(UiO-66-NH2SO3.cif)**	$\{[Zr_6O_4(OH)_4]^{12+}\}_7\{(OOC(C_6H_4)COO)\}_{30}\{(OOC(C_6H_4)NH_2)\}_3\{(OOC(C_6H_4)SO_3Na)\}_9\{OH,H_2O\}_{11}$
UiO-66-NH_2/SO_3-2 **(UiO-66-NH2SO3-2.cif)**	$\{[Zr_6O_4(OH)_4]^{12+}\}_7\{(OOC(C_6H_4)COO)\}_{31}\{(OOC(C_6H_4)NH_2)\}_3\{(OOC(C_6H_4)SO_3Na)\}_8\{OH,H_2O\}_{11}$

Since TGA cannot differentiate between missing linker and missing clusters, whereas PXRD and N_2 adsorption and desorption isotherms suggested the presence of missing clusters in UiO-66-SO_3 and UiO-66-NH_2/SO_3, we have included 1 missing cluster into the simulated structures of these MOFs. We have included the experimental estimated molecular formulas for both structures in **Table S14**.

Table S14: Stoichiometry extracted from TGA and ^{1}HNMR by multiplying our extracted formula per Zr (Table S4) by the number of Zr on the 2x2x2 cell.

Name	**Experimental stoichiometry**
UiO66	$\{[Zr_6O_4(OH)_4\}_8\{(OOC(C_6H_4)COO)\}_{41.12}\{AcOH\}_{0.12}\{FA\}_{0.24}\{OH/H_2O\}_{13.4}$
UiO-66-NH_2	$\{[Zr_6O_4(OH)_4\}_8\{(OOC(C_6H_4)COO)\}_{39.56}\{(OOC(C_6H_4)NH_2)\}_{2.4}\{AcOH\}_{0.33}\{FA\}_{0.1}\{OH\}_{14}\{DMF\}_8\{H_2O\}_{5.9}$
UiO-66-SO_3	$\{[Zr_6O_4(OH)_4\}_8\{(OOC(C_6H_4)COO)\}_{36.04}\{(OOC(C_6H_4)SO_3Na)\}_{7.2}\{AcOH\}_{0.48}\{FA\}_{0.05}\{OH/H_2O\}_{16.18}$ $\{[Zr_6O_4(OH)_4\}_7\{(OOC(C_6H_4)COO)\}_{31.55}\{(OOC(C_6H_4)SO_3Na)\}_{6.3}\{AcOH\}_{0.41}\{FA\}_{0.04}\{OH/H_2O\}_{14.14}$
UiO-66-NH_2/SO_3	$\{[Zr_6O_4(OH)_4\}_8\{(OOC(C_6H_4)COO)\}_{28.6}\{(OOC(C_6H_4)NH_2)\}_{3.79}\{(OOC(C_6H_4)SO_3Na)\}_{9.07}\{AcOH\}_{0.43}\{FA\}_{0.05}\{OH/H_2O\}_{25.39}$ $\{[Zr_6O_4(OH)_4\}_7\{(OOC(C_6H_4)COO)\}_{25.05}\{(OOC(C_6H_4)NH_2)\}_{3.33}\{(OOC(C_6H_4)SO_3Na)\}_{7.94}\{AcOH\}_{0.38}\{F$

	A}$_{0.04}${OH/H$_2$O}$_{22.21}$

The framework atoms were optimised within their experimental unit cells (see **Table S13-14** before the Monte Carlo simulations (see further). The DFT-optimised structures are present in **Figure S105**. In particular, the projected augmented wave (PAW)[12] method was used as implemented in the Vienna Ab Initio Simulation Package[13,14] (VASP 6.4.2) to describe interactions between core and valence electrons with corresponding standard PBE-PAW-potentials. The atomic positions were optimised using the conjugate gradient algorithm with force and electronic convergence criteria of 0.01 eV/Å and 10^{-6} eV, a Gaussian smearing of 0.05 eV, a plane wave energy cut-off of 600 eV, a 2x2x2 Monkhorst-Pack[15] k-point grid, and with the assumption of ferromagnetic coupling between the two unpaired electrons for each Ni atom. The atomic point charges used for the framework models can be found in the supplementary CIF files (UiO-66.cif, UiO-66-NH2.cif, UiO-66-SO3.cif, UiO-66-NH2SO3.cif, UiO-66-NH2SO3-2.cif)**.**

Canonical Monte Carlo (CMC) simulations[16] were performed to confirm the main binding site locations for CO_2 in **UiO-66-SO_3, UiO-66-NH_2/SO_3, UiO-66-NH_2/SO_3-2, UiO-66-NH_2,** and **UiO-66** frameworks. CMC simulations were performed in Materials Studio [17] at 273 K on a 2x2x2 supercell of the frameworks (Table **S13**). To describe the electrostatic interaction between the framework models and CO_2, their atomic point charges were determined via the charge equilibration (Qeq) method. Electrostatic interactions calculated using the Ewald[18] summation method for enhanced accuracy. The Qeq point charges used for CO_2 are given in **Figure S106**, while the atomic point charges used for the framework models can be found in the supplementary CIF files (UiO-66.cif, UiO-66-NH2.cif, UiO-66-SO3.cif, UiO-66-NH2SO3.cif, UiO-66-NH2SO3-2.cif)**.** Furthermore, the Lennard-Jones parameters were obtained from the Universal Force Field (UFF)[18]as implemented in the Material Studio forcefield library, employing the Lorentz-Berthelot mixing rules for the interaction parameters (ε_{ij}, σ_{ij}) between unlike atoms i and j. A cut-off distance of 12 Å was applied for non-bonded interactions, with the potentials smoothly truncated using a cubic spline function over a spline width of 1 Å.

For the CMC simulations, the frameworks were considered rigid, with atoms fixed at their DFT-optimised positions and a fixed loading of one CO_2 molecule (per supercell). In the canonical ensemble, the Metropolis sampling method considered different moves, such as translation (corresponds with a translation of the selected adsorbate molecule), rotation around the center of mass of the selected adsorbate molecule, regrowth (removes a selected adsorbate molecule from the system and reintroduces it at a random position with random orientation), and conformer (collects multiple adsorbate conformations), with relative probabilities of 1, 1, 0.1 and 1, respectively. CMC simulations included 3×10^6 loading steps, followed by 3×10^6 equilibration steps, and finally, 3×10^6 production steps to ensure reasonable ensemble averages. The output of the CMC simulations was visualised as adsorbate density fields, encompassing the mass-middle points of all successful adsorbate MC moves (see **Table S15**). From the table, the adsorption binding sites of CO_2 are primarily observed around defects. In frameworks with moderate defects, such as **UiO-66-NH_2** and **UiO-66**, the number density of adsorbed CO_2 is barely detectable within the applied density range (0–3.5 molecules/$Å^3$) in the density map for all frameworks. To better identify potential CO_2 binding sites, we also visualize the density field for these frameworks using a narrower density range (0–0.2 molecules/$Å^3$) (see **Table S16**). We also created an isosurface of constant density and coloured it by the potential energy (see **Figure S107**). From the colour-mapped isosurfaces, we can observe that among all the studied adsorbates, CO_2 in the framework including all SO_3, NH_2 and carboxyl groups (**UiO-66-NH_2/SO_3, UiO-66-NH_2/SO_3-2)** have the lowest potential energy, indicating the most favourable binding sites. Since $-SO_3Na$, $-NH_2$, and $-COOH$ groups are positioned around the defect region, they create a synergistic effect, enhancing CO_2 adsorption: $-SO_3Na$ groups introduce strong electrostatic interactions, attracting CO_2 molecules, while $-NH_2$ groups can engage in dipole–quadrupole interactions with CO_2. Carboxyl groups ($-COOH$) can result in binding via hydrogen bonding and polar interactions.

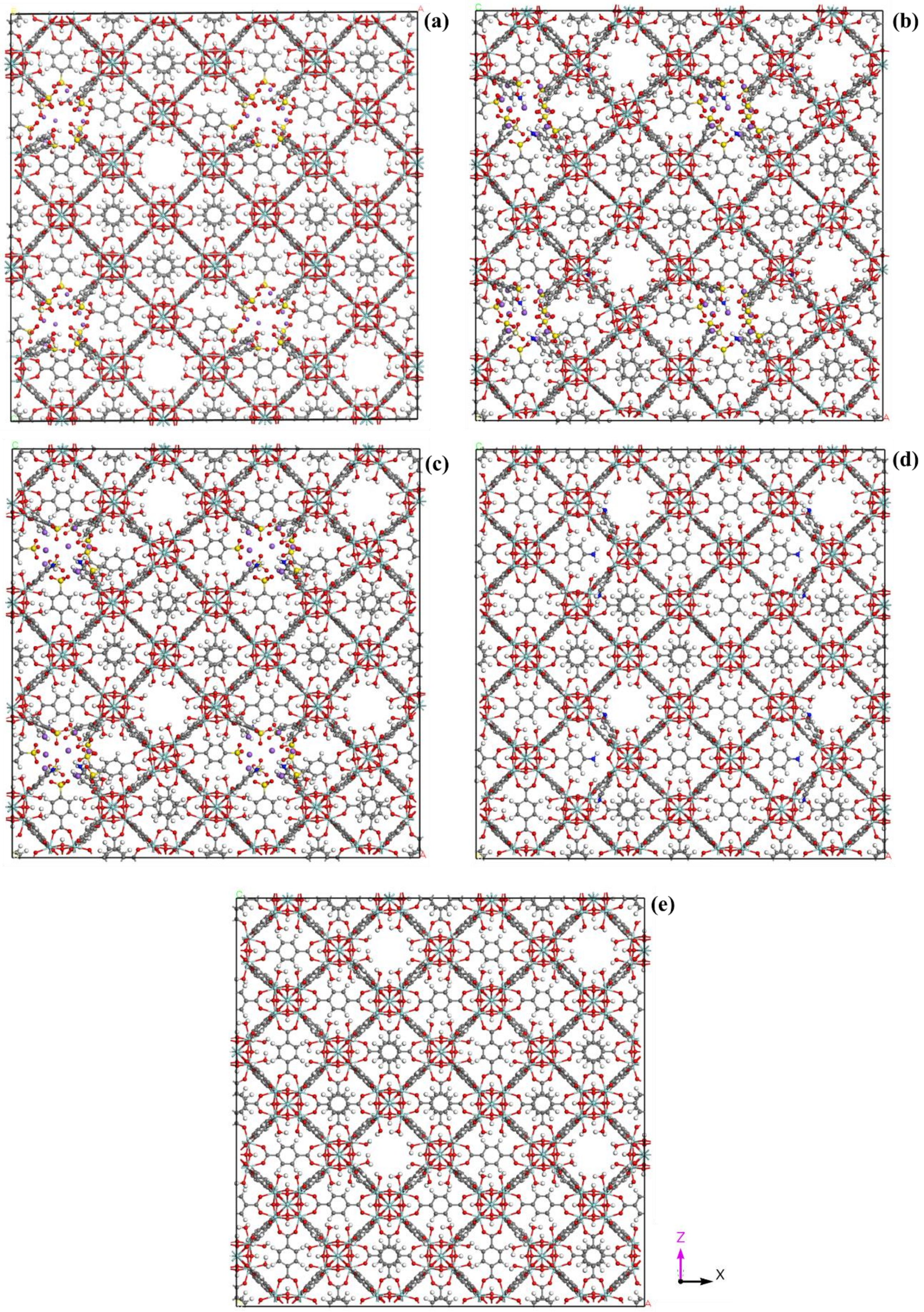

Figure S105: DFT-Optimised (a) UiO-66-SO_3, (b) UiO-66-NH_2/SO_3, (c), UiO-66-NH_2/SO_3-2 (d) UiO-66-NH_2, (e) UiO-66 structures.

To gain a deeper understanding of the binding sites, we also performed CMC simulations at a fixed loading of one CO_2 molecule per unit cell. **Table S19** presents the three most stable CO_2 binding sites in each framework.

Grand Canonical Monte Carlo (GCMC) simulations were performed to gain deeper insight into the CO_2 adsorption isotherms of the model systems. The Metropolis sampling technique and force field parameters used in these simulations follow those detailed in the CMC section. The adsorption isotherms were calculated over a pressure range of 0 to 1 bar at 273 K. Each GCMC simulation consisted of 3×10^6 equilibration steps, followed by 3×10^6 production steps, ensuring reliable ensemble averages. The simulated adsorption isotherms for the studied frameworks are presented in **Figure S108**. The results indicate that the highest **CO_2** uptake occurs in **UiO-66-NH_2/SO_3** and **UiO-66-NH_2/SO_3-2,** which aligns with the binding site analysis **(Tables S15-S17)** and the experimentally obtained adsorption isotherms **(**see **Figure S106).**

Overall, the CMC and GCMC simulations demonstrate that CO_2 adsorption is strongly influenced by **the presence of defects and functional groups** ($-SO_3$, $-NH_2$, and −COOH), with the highest uptake observed in **UiO-66-NH_2/SO_3** and **UiO-66-NH_2/SO_3-2**, confirming that these frameworks provide the most favorable binding sites and adsorption capacities.

Figure S106: Atomic structures and point charges of CO_2.

Table S15: The adsorbate density fields obtained from CMC simulations for CO_2, at 273 K in **UiO-66-SO_3, UiO-66-NH_2/SO_3, UiO-66-NH_2/SO_3-2, UiO-66-NH_2,** and **UiO-66**. They allow the identification of optimal binding sites. The colour map values indicate the density of the adsorbate in molecules/Å^3.

Structure	View 1	View 2
UiO-66-SO_3	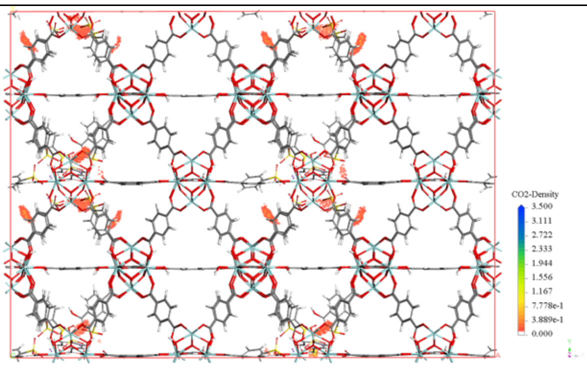	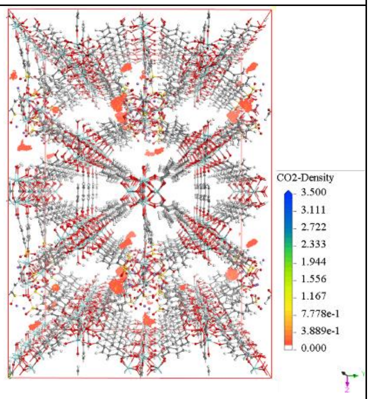
UiO-66-NH_2/SO_3	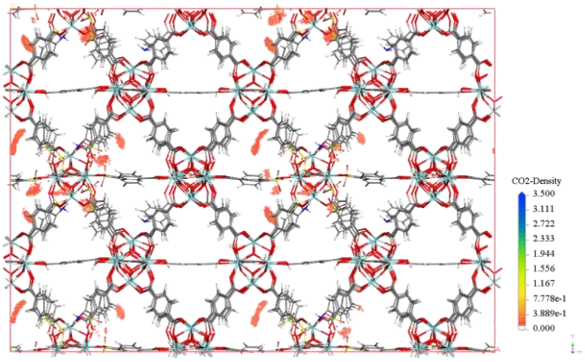	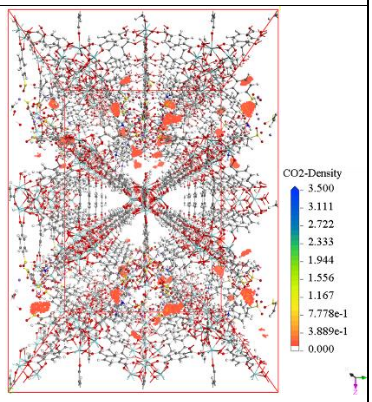
UiO-66-NH_2/SO_3 -2	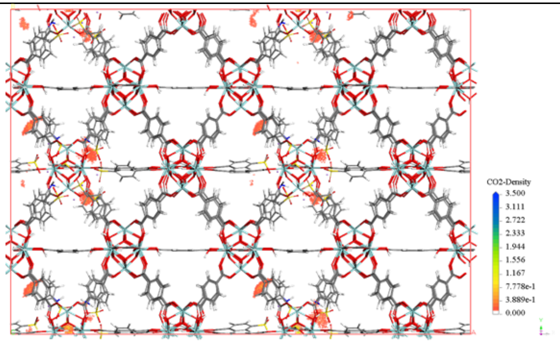	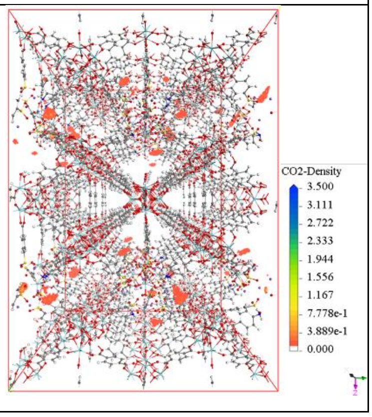

UiO-66-NH$_2$	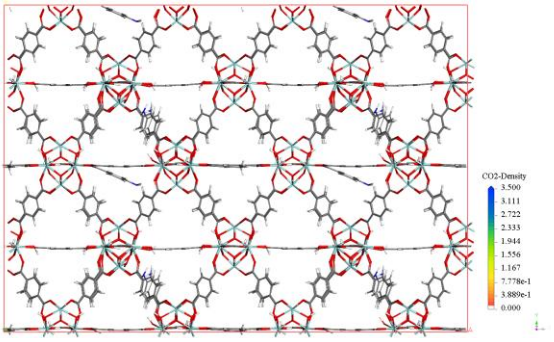	
UiO-66	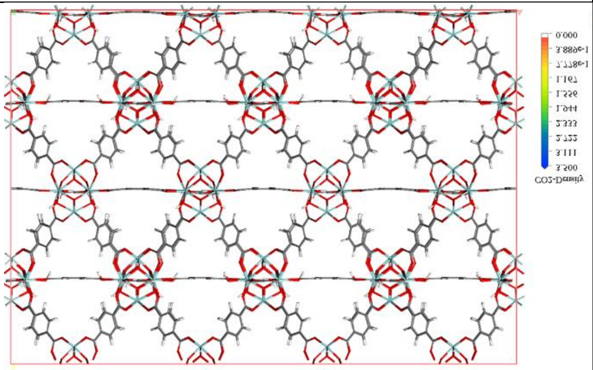	

Table S16: The adsorbate density fields obtained from CMC simulations for CO_2, at 273 K in **UiO-66-NH$_2$,** and **UiO-66**. They allow the identification of optimal binding sites. The colour map values indicate the density of the adsorbate in molecules/Å^3.

Structure	**View 1**	**View 2**
UiO-66-NH$_2$	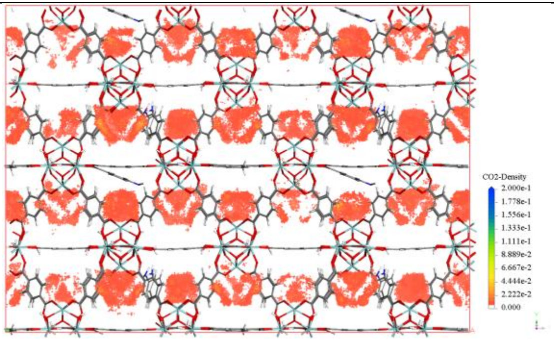	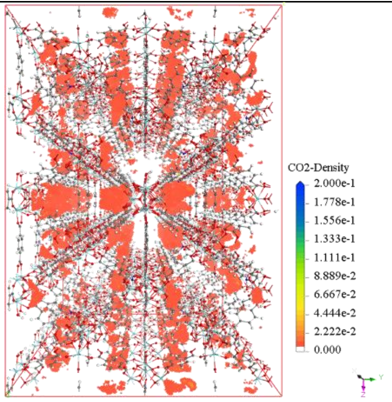

UiO-66	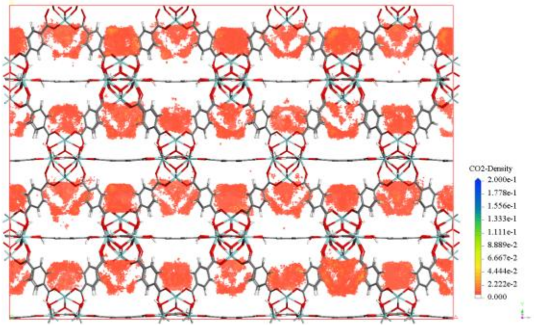CO2-Density 2.000e-1 1.778e-1 1.556e-1 1.333e-1 1.111e-1 8.889e-2 6.667e-2 4.444e-2 2.222e-2 0.000	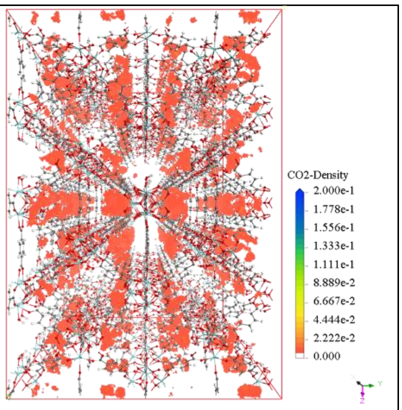CO2-Density 2.000e-1 1.778e-1 1.556e-1 1.333e-1 1.111e-1 8.889e-2 6.667e-2 4.444e-2 2.222e-2 0.000 Y Z

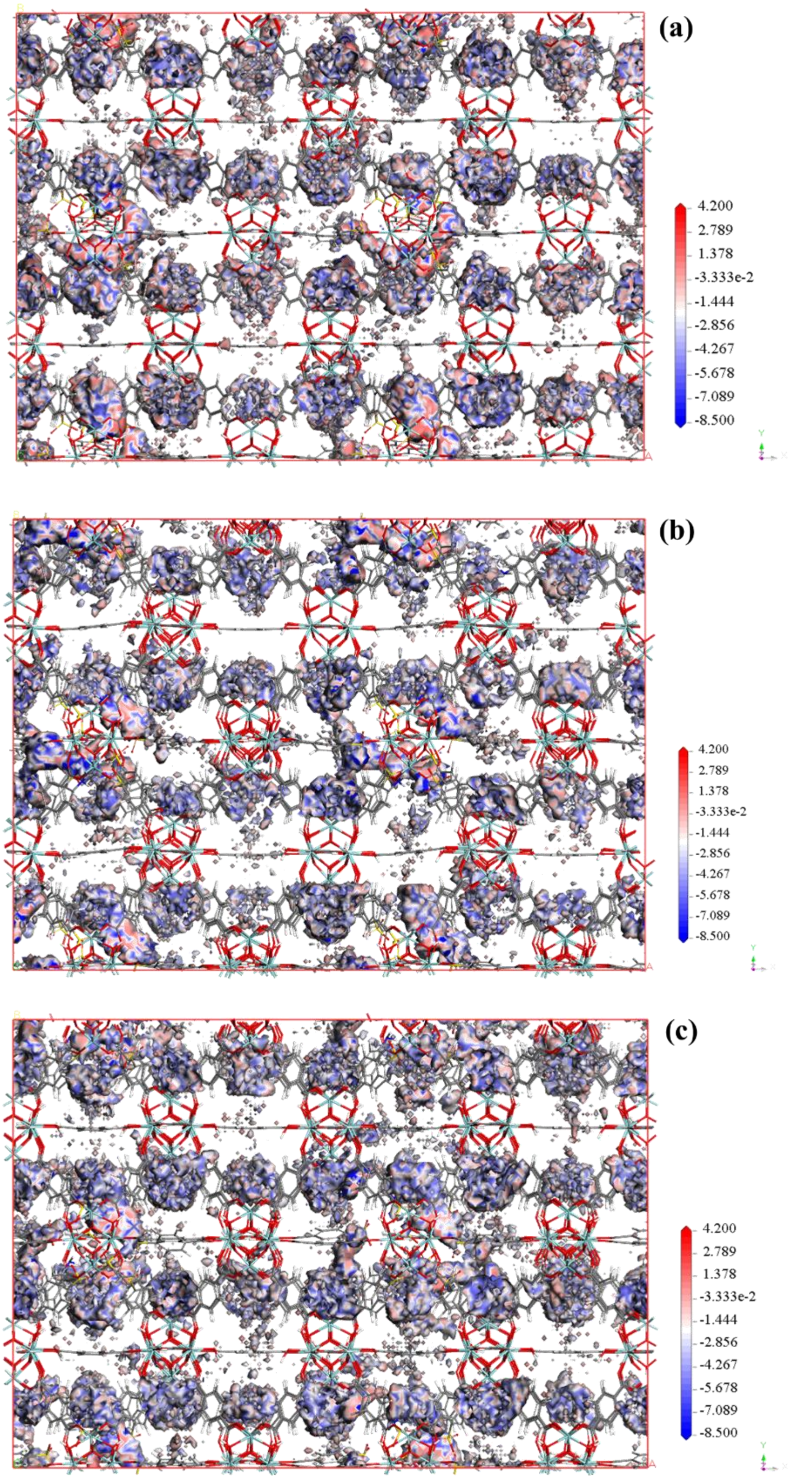

Figure 107 Energy and density distribution information at 273 K. It has created an isosurface of constant CO_2 density (isovalue= 0.001) in (a) **UiO-66-SO$_3$,** (b) **UiO-66-NH$_2$/SO$_3$,** and (c) **UiO-66-NH$_2$/SO$_3$-2**, and coloured it by the potential energy. In this representation, regions shaded in dark blue signify the lowest energy, while those shaded in dark red denote the highest energy. This analysis can be used to identify favourable binding sites within the framework. The colour map values indicate the potential energy of the adsorbate in kcal/mol.

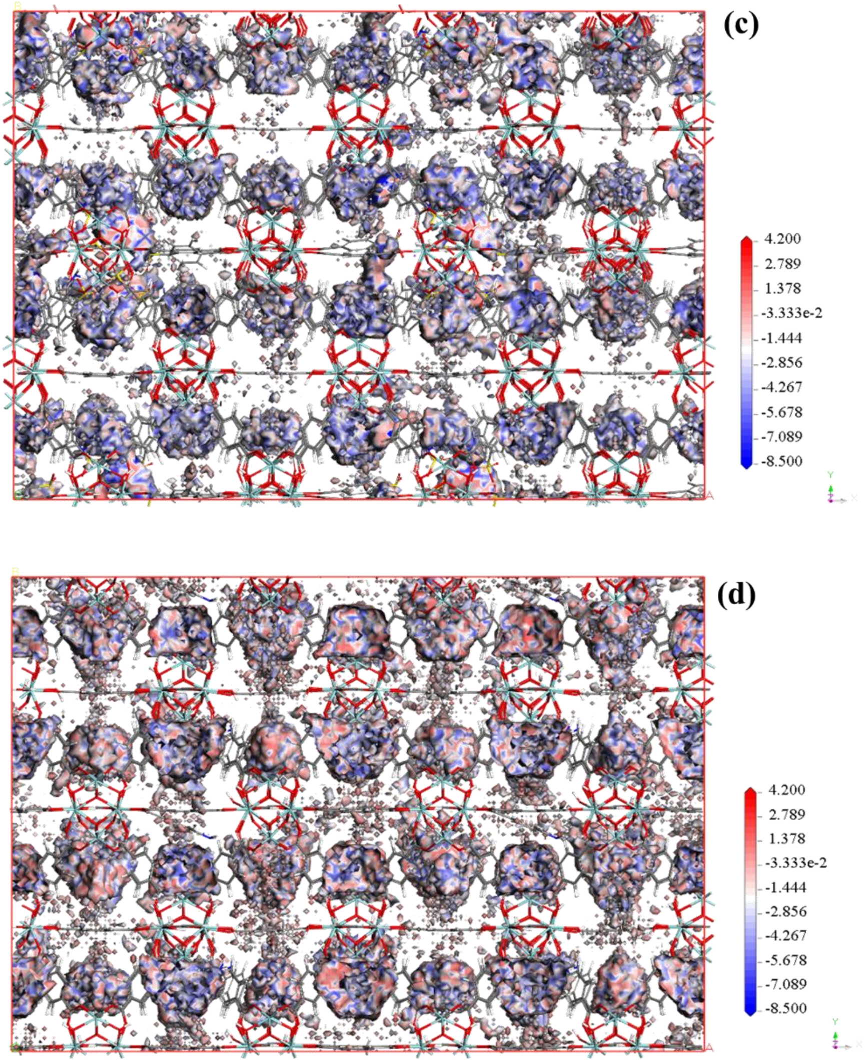

Figure S107 (continued): Energy and density distribution information at 273 K. It has created an isosurface of constant CO_2 density (isovalue= 0.001) in (d) **UiO-66-NH_2,** and **(e) UiO-66**, and coloured it by the potential energy. In this representation, regions shaded in dark blue signify the lowest energy, while those shaded in dark red denote the highest energy. This analysis can be used to identify favourable binding sites within the framework. The colour map values indicate the potential energy of the adsorbate in kcal/mol.

Table S19: Visualisation of most stable CO$_2$ binding sites in the frameworks.

Structure	Binding site 1	Binding site 2	Binding site 3
UiO-66-SO$_3$	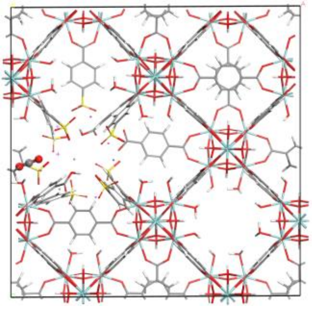	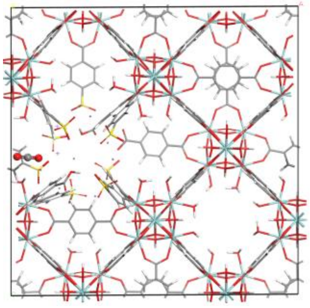	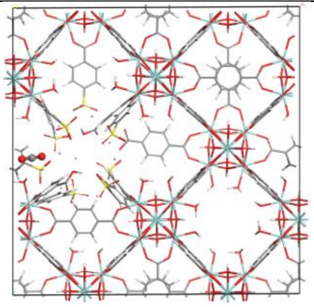
UiO-66-NH$_2$SO$_3$	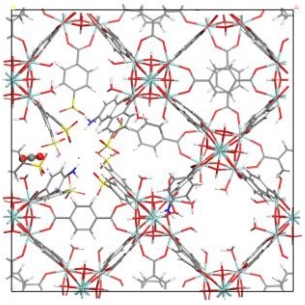	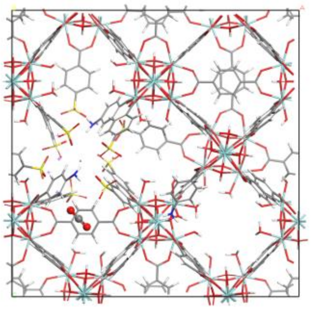	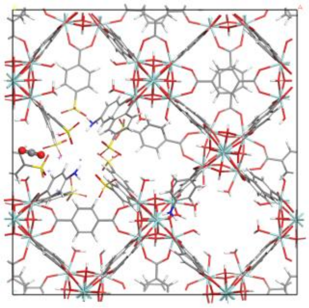
UiO-66-NH$_2$SO$_3$-2	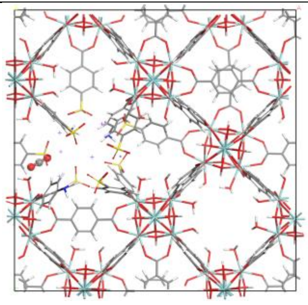	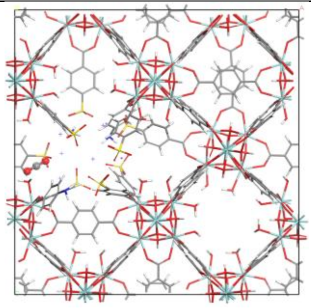	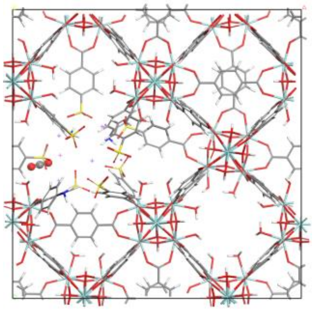
UiO-66-NH$_2$	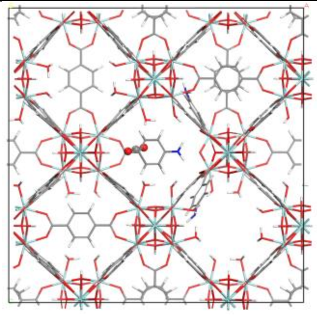	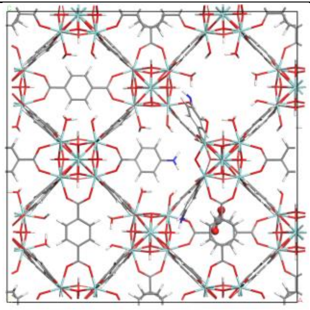	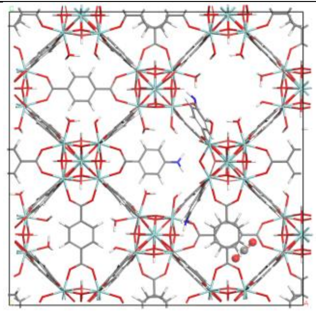
UiO-66	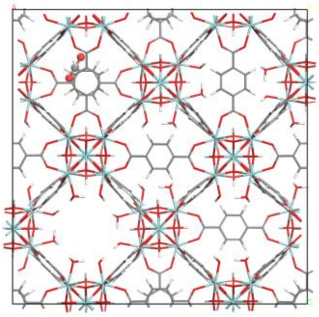	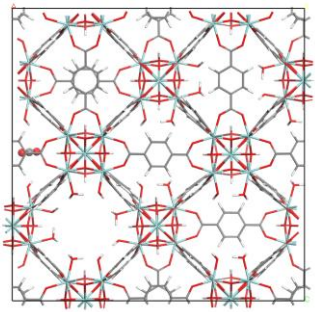	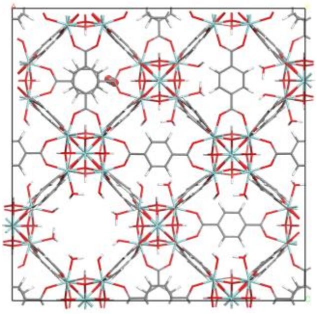

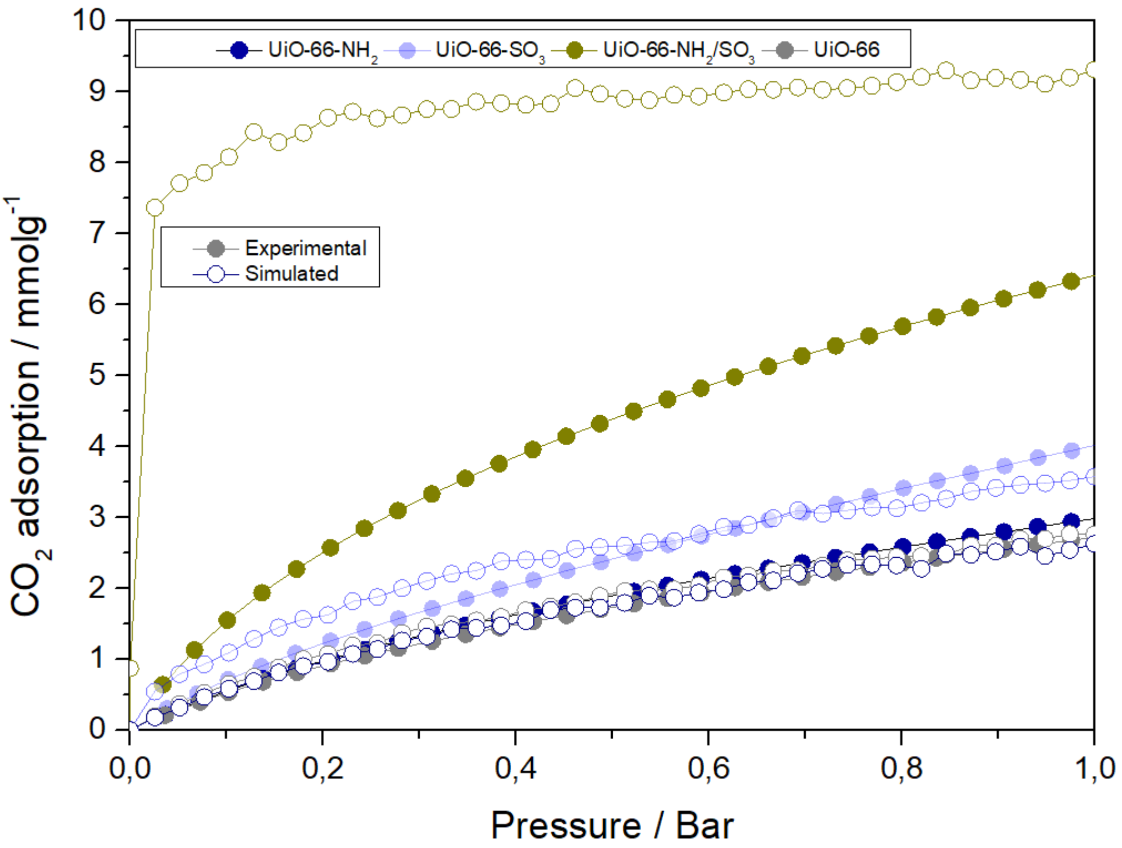

Figure S108: Comparison of the experimental and simulated adsorption isotherms obtained from the GCMC calculations for CO_2 (273K)

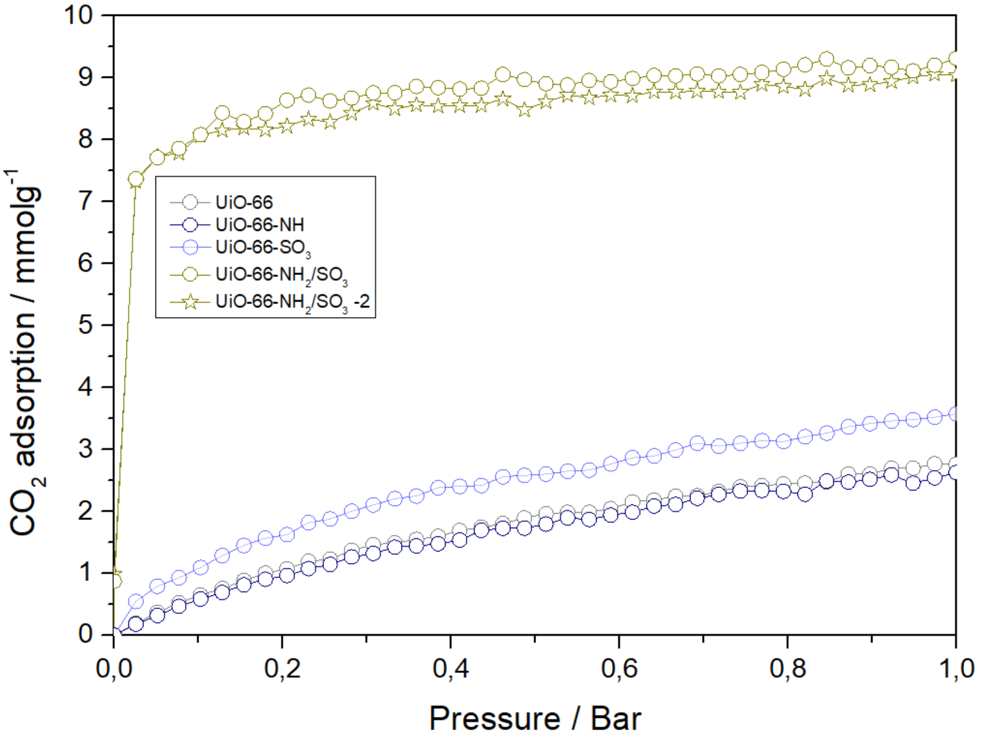

Figure S109: Adsorption isotherms obtained from the GCMC calculations for CO_2 (273K)

S.9. References

1 G. C. Shearer, S. Chavan, S. Bordiga, S. Svelle, U. Olsbye and K. P. Lillerud, *Chem. Mater.*, 2016, **28**, 3749–3761.

2 X. Feng, J. Hajek, H. S. Jena, G. Wang, S. K. P. Veerapandian, R. Morent, N. D. Geyter, K. Leyssens, A. E. J. Hoffman, V. Meynen, C. Marquez, D. E. D. Vos, V. V. Speybroeck, K. Leus and P. V. D. Voort, *J. Am. Chem. Soc.*, 2020, **142**, 3174–3183.

3 L. Valenzano, B. Civalleri, S. Chavan, S. Bordiga, M. H. Nilsen, S. Jakobsen, K. P. Lillerud and C. Lamberti, *Chem. Mater.*, 2011, **23**, 1700–1718.

4 I. A. Lázaro, *Eur. J. Inorg. Chem.*, 2020, **2020**, 4284-4294.

5 J. Ilavsky and P. R. Jemian, *J. Appl. Crystallogr.*, 2009, **42**, 347–353.

6 T. Li, A. J. Senesi and B. Lee, *Chem. Rev.*, 2016, **116**, 11128–11180.

7 H. Hayashi, T. Morita and K. Nishikawa, *Chem. Phys. Lett.*, 2009, **471**, 249–252.

8 O. Glatter, O. KratkyChapter 2 General Theory by Porod, G.; *Academic Press INC (London) LTD.* 1982, 18-51.

9 F. C. N. Firth, M. J. Cliffe, D. Vulpe, M. Aragones-Anglada, P. Z. Moghadam, D. Fairen-Jimenez, B. Slater and C. P. Grey, *J. Mater. Chem. A*, 2019, 7, 7459–7469.

10 J. H. Cavka, S. Jakobsen, U. Olsbye, N. Guillou, C. Lamberti, S. Bordiga and K. P. Lillerud, *J. Am. Chem. Soc.*, 2008, **130**, 13850–13851.

11 J. Wellendorff, K. T. Lundgaard, A. Møgelhøj, V. Petzold, D. D. Landis, J. K. Nørskov, T. Bligaard and K. W. Jacobsen, *Phys. Rev. B*, 2012, **85**, 235149.

12 P. E. Blöchl, *Phys. Rev. B*, 1994, **50**, 17953–17979.

13 G. Kresse and D. Joubert, *Phys. Rev. B*, 1998, **59**, 1758–1775.

14 G. Kresse and J. Furthmüller, *Comp. Mater. Sci.*, 1996, **6**, 15–50.

15 H. J. Monkhorst and J. D. Pack, *Phys. Rev. B*, 1976, **13**, 5188–5192.

16 D. Frenkel, B. Smit, *Academic Press: New York* **2002**, 112-114.

17 BIOVIA, Dassault Systèmes, Material Studio, San Diego: Dassault Systèmes, 2023.

18 A. Y. Toukmaji and J. A. Board, *Comput. Phys. Commun.*, 1996, **95**, 73–92.